NOVEL MATERIALS AND TECHNIQUES FOR ENERGY CONVERSION AND SENSING

A DISSERTATION SUBMITTED TO
THE GRADUATE SCHOOL OF ENGINEERING AND SCIENCE
OF BILKENT UNIVERSITY
IN PARTIAL FULFILLMENT OF THE REQUIREMENTS FOR
THE DEGREE OF
DOCTOR OF PHILOSOPHY
IN
MATERIALS SCIENCE AND NANOTECHNOLOGY

By
Okan Öner Ekiz
December 2015

Novel Materials and Techniques for Energy Conversion and Sensing
By Okan Öner Ekiz
December 2015

We certify that we have read this dissertation and that in our opinion it is fully adequate, in scope and in quality, as a dissertation for the degree of Doctor of Philosophy.

Aykutlu Dana(Advisor)

Ceyhun Bulutay

Ali Kemal Okyay

Adil Denizli

Hatice Duran

Approved for the Graduate School of Engineering and Science:

Levent Onural
Director of the Graduate School

ABSTRACT

NOVEL MATERIALS AND TECHNIQUES FOR ENERGY CONVERSION AND SENSING

Okan Öner Ekiz
Ph.D. in Materials Science and Nanotechnology
Advisor: Aykutlu Dana
December 2015

In the recent years, characterization of nanomaterials and using them in sensing applications gain considerable attention. Increased research on nanotechnology brings new materials and techniques that come with many unsought properties. Additionally, novel materials and concepts have created new demands for new characterization techniques. In this thesis, our main aim is to characterize novel materials and develop new techniques to use nanotechnology in sensing applications.

Graphene is one of the most important material in nanotechnology found in the recent years. In this thesis, we have characterized and explain the electrochemical behavior of graphene oxide. During the experiments, novel properties of graphene oxide have been revealed. Foundings paved the way for new applications of graphene.

Recent studies in plasmonic materials made SERS (Surface-Enhanced-Raman-Spectroscopy) an important characterization tool used in nanotechnology. SERS is a powerful technique for chemical specific and label free analysis of low concentration materials. In this thesis, we have used SERS to build an artificial nose for detection of VOCs. SERS substrates have been fabricated and used for the experiments. Experiments showed that our technique could detect many VOCs and could be used for several applications such as explosive and drug detection.

There is a strong need for easy and cost effective biosensors especially for home-care applications. Recent advances in nanotechnology help us to develop cost effective techniques. Reducing costs could make biosensors more accessible for end user applications such. In this thesis, we have developed a biosensor platform by using SPR (Surface Plasmon Resonance) for pathogen detection. Experiments showed that our device could detect 10^2 pathogens without labeling. Our aim is to improve this platform for rapid food analysis and home-care applications.

Keywords: Graphene, Graphene oxide, Raman microscopy, SERS, Surface plasmon resonance, bacterial sensing, pathogen detection, Single molecule sensing.

ÖZET

ENERJİ ÇEVRİMİ VE ALGILAMA AMAÇLI YENİLİKÇİ MALZEMELER VE TEKNİKLER

Okan Öner Ekiz
Malzeme Bilimi ve Nanoteknoloji, Doktora
Tez Danışmanı: Aykutlu Dana
Aralık 2015

Nanomalzemelerin karakterizasyonu ve sensör teknolojilerde kullanımı son yıllarda ciddi miktarda önem kazanmıştır. Nanomalzemeler üzerine yapılan araştırmaların artması farklı malzemelerin ve tekniklerin bulunmasını sağlamıştır. Yeni malzemeler, araştırılmayı bekleyen bir çok özellik ihtiva etmektedir. Ek olarak, farklı karakterizasyon tekniklerinin geliştirilmesi için talep oluşturmaktadır. Bu tez çalşmalarında amacımız yeni malzemeleri karakterize edip, nanoteknolojiyi kullanarak uygulamalar geliştirmektir.

Grafen son yıllarda bulunmuş nanoteknoloji alanındaki en önemli malzemelerdendir. Bu tez çalışmaları sırasında, Grafen karakterize edilip, elektrokimyasal davranışları aıklanmıştır. Yapılan deneylerde, grafen oksitin bazı yeni özellikleri ortaya ıkarılmıştır. Elde edilen bulgular Grafenin yeni uygulamalarının yolunu açmıştır.

Son yıllarda plazmonik alanında yapılan çalışmalar SERS (Yüzey Yükseltilmiş Raman Spektroskopisi)′i nanoteknoloji alanında kullanılan önemli bir karakterizasyon aracı haline getirmiştir. SERS, düşük konsantrasyonlu malzemeler için kimyasal belirli işaretlemesiz bir analiz yapabilen gülü bir tekniktir. Bu tez çalışmalarında, SERS′ i kullanarak uçucu organik kimyasalları tesbit edebilen yapay burun yapılmıştır. Deneylerde kullanılan SERS substratları üretilmiştir. Yapılan deneyler göstermektedirki, kullandımız teknik bir çok uçucu organik kimyasalı tesbit edebilmektedir ve patlayıcı ve uyuşturucu tesbiti gibi bir ok alanda kullanılabilmektedir.

Kişisel ve ev uygulamaları için düşük maliyetli ve kolay kullanımlı biyosensör sistemleri için ihtiyaç vardır. Nanoteknoloji alanındaki gelişmeler, uygun maliyetli tekniklerin geliştirilmesinde bize yardımcı olmaktadır. Maliyetlerin düşürülmesi, biyosensörlerin son kullanıcılar için daha ulaşılabilir yapabilmektedir. Bu tez alışmalarında, yüzey plazmon rezonans tekniini kullanılarak gıda sulularının tesbitini yapan bir biyosensör platformu üretilmiştir. Yapılan deneyler

göstermektedir ki, geliştirilen cihaz yaklaşk 100 suçluyu işaretlemesiz olarak tesbit edebilmektedir. Amacımız geliştirilen bu platformu , hızlı gıda analizi ve son kullanıcı uygulamaları için geliştirmektir.

Anahtar sözcükler: Grafen, Grafen oksit, Raman mikroskopisi, SERS, Yüzey plazmon rezonans, Bakteri tesbiti, Patojen tesbiti, Tek molekül tesbiti.

Acknowledgement

First, I would like to thank my advisor Dr.Aykutlu Dana for his continuous guidance throughout my PhD. He always encouraged and supported me with novel ideas. Seven years with Dr.Dana was a great experience and will always be remembered.

I owe my sincere thanks to Prof. Dr. H. İbrahim Ekiz. He generously allowed me to use his cell culture facilities in Mersin University. I would like to thank Esma Eser, Hikmet Çelik and Selim Sülek for their support and friendship during the experiments.

I would like to thank all the people contributed to this thesis, Dr. Ali Kemal Okyay, Dr. Ceyhun Bulutay, Dr. Adem Yildirim, Göksu Çınar, Prof.Dr. Engin Umut Akkaya, Dr. Mustafa Güler, Bihter Dağlar, Dr. Turgay Tenikay, Dr. Burak Türker, Sıla Toksöz, Dr. Handan Acar, Merve Türkşanli Kaplan, Hasan Guner, Mustafa Ürel, Dr. Sencer Ayaş, Koray Mizrak, and all the past and present members of UNAM. I would like to thank my best friend Sinan Baysal.

Last but most important, I would like thank my family who always believed in and supported me. I wish to give special thanks to Melis Şardan Ekiz, who stood by me for all those times.

...

Contents

List of Figures

List of Tables

Chapter 1

Introduction

In the recent years, the design and fabrication of nanomaterials for chemical and biological sensing have received considerable attention due to the increased demand for low-cost practical applications. Although, great amount of research progress has been done in nanomaterials, there are still uncharacterized properties of new materials such as electrochemical behaviour of graphene. Complete characterization of common nanomaterials is critical for practical applications. Graphene is one of the most important materials in nanotechnology. In this thesis, we have revealed novel properties of graphene and found new applications. Additionally, we have developed sensors by using SERS (Surface Enhanced Raman Spectroscopy) and SPR (Surface Plasmon Resonance) techniques.

In Chapter 2, we demonstrate that graphene oxide can be reversibly reduced and oxidized using electrical stimulus. Controlled reduction and oxidation in two-terminal devices containing multilayer graphene oxide films are shown to result in switching between partially reduced graphene oxide and graphene, a process which modifies the electronic and optical properties. High resolution tunneling current and electrostatic force imaging reveal that graphene oxide islands are formed on multilayer graphene, turning graphene into a self-assembled heterostructure random nanomesh. Charge storage and resistive switching behavior is observed in two-terminal devices made of multilayer graphene oxide films, correlated with electrochromic effects. Tip-induced reduction and oxidation are also

demonstrated. Results are discussed in terms of thermodynamics of oxidation and reduction reactions

In Chapter 3, we demonstrate reversible and irreversible changes in the ultrafast optical response of multilayer graphene oxide thin films upon electrical and optical stimulus. The reversible effects are due to electrochemical modification of graphene oxide, which allows tuning of the optical response by externally applied bias. Increasing the degree of reduction in graphene oxide causes excited state absorption to gradually switch to saturable absorption for shorter probe wavelengths. Spectral and temporal properties as well as the sign of the ultrafast response can be tuned either by changing the applied bias or exposing to high intensity femtosecond pulses.

In Chapter 4, we demonstrate single molecule sensing of airborne molecules with Raman spectroscopy. Sensing mechanism is based on Raman scattering of hoping volatile organic compounds (VOCs) on surface-enhanced Raman spectroscopy (SERS) substrates. The demonstrated sensor can discriminate even residual fragrance molecules of cleaning products used around experimental set-up. Additionally, we showed that excess amount of target molecules could not saturate the sensor contrary to mammalian olfactory system. Experiments revealed that sensor surface repels excess molecules with a light driven force. This phenomenon could be observed on sensor surface dip-coated with target molecules. Videos of light driven motion will be shown in the presentation. Spectra coming from SERS substrates are complicated and contain extensive amount of information to process manually. We have developed several algorithms to process and identify Raman spectra of hoping molecules.

In Chapter 5, we report rapid and sensitive detection of *Salmonella Enteritidis* and *Listeria* with high specificity by using SPR (Surface Plasmon resonance) technique. Antibodies against *S. Enteritidis* and *Listeria* were immobilized on to a gold sensor surface and different concentrations of serially diluted bacterial solutions were pumped in to the system. The changes in the response unit (RU) due to the binding of different concentrations of bacteria were measured. Regeneration of the sensor surface was carried out by using PBS + Tween 80 solution. The selectivity of the developed sensor was examined with different bacterial

species which did not produce any significant response. Additionally, the ability of the developed sensor to detect *S. Enteritidis* in milk samples was tested. Based on these results, the developed SPR based biosensor may be used for rapid, label-free, sensitive and selective detection of bacteria in food materials.

Chapter 2

Reversible Electrical Reduction and Oxidation of Graphene Oxide

2.1 Introduction

Graphene [1, 2, 3] has received tremendous attention in recent years due to its potential applications in electronics[4, 5, 6], sensors[7, 8, 9], energy storage[10, 11, 12], and optics[13, 14, 15]. Despite the extreme intrinsic mobility of graphene,[16] semimetallic electronic band structure limited its use in high-performance transistors. Quantum confinement effects were theoretically [17, 18] and experimentally [19, 20] shown to modify the band structure, making graphene a more versatile material. Chemical modification is still being actively sought to form semiconductors in the graphene family and implement conventional optoelectronic device structures. Novel devices have been reported that combine the superior electronic properties of graphene with other chemical and mechanical phenomena, such as resistive switching and electromechanical memories.[21, 22, 23] The mechanism of observed resistive switching in some graphene-based devices remained unclear. Graphene oxide (GO) is an insulator with a large effective band gap and band structure that depends on the stoichiometry.[24, 25] It has been previously observed that graphene oxide can

be reduced controllably at low temperature (low-T) in ambient atmosphere.[26] In such a low-temperature reduction process, the resistivity of the films can be continuously monitored and can be used to control the degree of reduction. Interruption of thermal reduction results in partially reduced graphene oxide (PRGO). Conduction mechanisms of such PRGO films are known to be different than multilayer graphene (MLG) films, as evidenced by temperature dependence of resistivity.[26, 27, 28] A hopping transport mechanism was thought to be dominant in such films, and limited evidence for the presence of oxygen-rich domains was provided through scanning tunneling microscopy (STM) imaging of PRGO layers.[29] Recently, thermal site selective reduction of graphene oxide is demonstrated using a heated atomic force microscope tip.[30] STM has also been used to image hydrogen atoms on graphene and to create nanoscale heterostructure patterns by tip induced hydrogen desorption.[31] Recently, a conductive atomic force microscopy tip was used to characterize nanoscale surface conductivity of graphene oxide, and tip-induced reduction was shown to be possible.[32] In this work, we demonstrate electrically induced reversible reduction of graphene oxide, resulting in changes in the electronic and optical properties of graphene-based thin films. It is observed that optical and electronic property changes are correlated with the formation of a graphene/graphene oxide nanomesh.

2.2 Synthesis of graphene oxide

Graphene oxide was synthesized from natural graphite (SP-1, Bay Carbon) by the Hummers method.[33] 25 ml of 66° sulfuric acid was cooled to 0 °C with an ice bath in a 100 ml glass beeker. 1g of powdered graphite and 0.5 g of $NaNO_3$ were added to the sulfuric acid. While maintaining vigorous magnetic stirring, 3 g. of $KMnO_4$ was added to the solution. The temperature was kept below 20 °C during the addition of $KMnO_4$. The ice-bath was removed and temperature icreased to 35 °C for 30 minutes. Then, 50 ml of DI water was added slowly caused violent effervescence and increase in temperature to approximately 100 °C. The temperatuere was kept over 90 °C for over 10 minutes. The resulted solution was

diluted with 150 ml of DI water. Hydrogen peroxide was added to reduce the residual permanganate and manganese dioxide to colorless soluble manganese sulfate. After centrifugation of the solution at 8000 rpm for 30 minutes, the graphite oxide was precipitated and washed with DI water for three times with the same procedure. The graphite oxide DI water mixture was than ultrasonicated for 30 minutes. Ultrasonication exfoliated graphite oxide and dissolved it in DI water. To eliminate graphite and unexfoliated graphite oxide, the solution was centrifugated for 15 minutes at 14000 rmp. The bright yellow supernatant solution is the final product that is graphene oxide dissolved in DI water.

2.3 Experimental

Stable graphene suspensions were prepared by a fast and simple method. Hydrazine hydrate (0.1 mL, Merck) was added to the 10 mL of graphene oxide/water, and the mixture was heated to 85 °C for 1 h. A few minutes after the addition of hydrazine hydrate, the color of the mixture became black. At the end of 1 h, the graphene particles precipitated because of aggregation. Acetone (Sigma-Aldrich) was added to the solution with the same volume. After hydrazine treatment, the graphene surface contained hydrazone groups[34]. Acetone could modify the surface graphene by reacting with hydrazone groups; therefore, addition of acetone dissolves graphene in the water and hydrazine hydrate mixture. To completely suspend aggregated graphene, 5 min of sonication was applied to the mixture. Two-terminal devices were fabricated by sputtering Au-Pd films on precleaned glass substrates by using a 300 μm wide shadow mask. Graphene or GO suspensions were drop-casted on the devices fabricated. The films were dried under vacuum. Devices were characterized using a digital source meter (Keithley 2700) with a probe station. Graphene devices were annealed at 125-150 °C for 30 sec before measurements. Partially reduced graphene oxide samples were prepared by thermal annealing of graphene oxide films at 125 °C for 30 sec. Thermal annealing processes were applied on a preheated hot plate. Electrochemical experiments were performed under ambient conditions in clean room conditions, at room temperature (T = 25 (0.5 °C) and 40 (5 % humidity as monitored

by a humidity sensor, under 1 atm pressure. Electrical and XPS (X-ray photoelectron spectroscopy) measurements were done on a Thermo K-Alpha system. Multifrequency electrostatic force microscopy was implemented using modified commercial silicon cantilevers with spring constants of 2-4 N/m, and resonance frequencies of 65-75 kHz. The tips are double-stage electron-beam induced deposited Pt tips with a tip radius of 2-5 nm as inspected by scanning electron microscopy. Low-frequency electrostatic excitation was applied at 5 kHz, and first and second time harmonics of the electrostatic forces were monitored using lock-in amplifiers (Stanford Research Systems, SR 830). The details of the high resolution multi frequency electrostatic force microscopy and spectroscopy can be found in references [35, 36, 37].

2.4 Reversible oxidation and characterization of graphene

Electrical reduction of GO in air has been studied, using multilayer GO (MLGO) films deposited on metalized glass substrates. The two-terminal devices consist of thin (10-50 nm) Pd/Au planar contacts, separated by 0.3-0.6 mm, with a thin multilayer GO film covering both contacts and in between (Figure 2.1). Upon application of a bias to the contacts, the positive contact is seen to be oxidized and the negative contact is seen to be reduced. There is a potential drop between the contacts due to the finite conductivity of the films. Experiments showed that stoichiometry depends on the distance from the contacts, as confirmed by X-ray photoelectron spectroscopy (XPS) (Figure 2.2). The reduction/oxidation can be reversed by reversal of the bias.

The optical transparencies of the films are also dependent on the oxidation

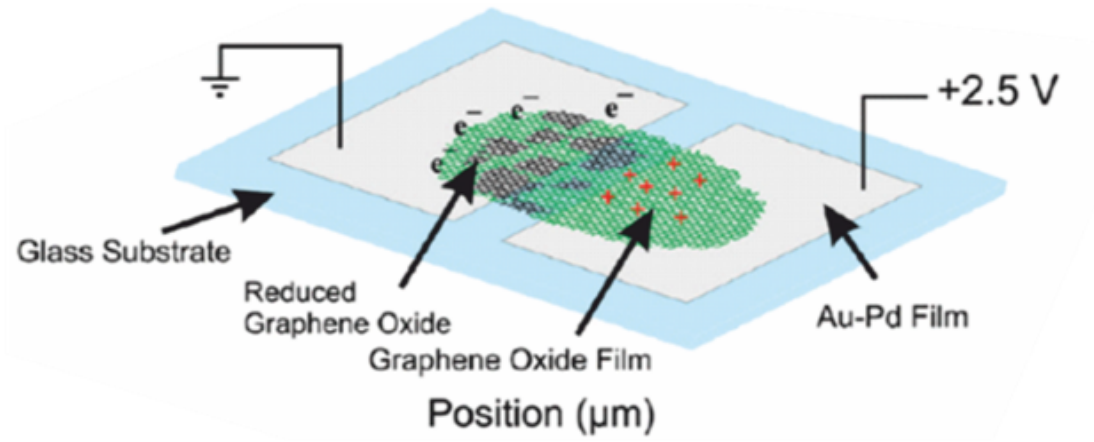

Figure 2.1: Thin multilayer graphene oxide films (30-60 nm thickness) can be electrically reduced and oxidized. The two terminal device is schematically shown. Two therminal device was fabricated by sputtering Au-Pd on a glass substrate with a shadow mask.

state. Wavelength-dependent linear transmission is measured using a fiber-coupled spectrometer near one of the contacts, while the bias is swept quasi-statically between -2.5 and 2.5 V. A gradual increase of the absorption edge as a function of applied bias is observed (Figure 2.3a). The optical transparency is correlated with the oxidation state (Figure 2.3b and c), films being semitransparent in the oxidized state. During cyclic voltage sweeps, it is observed that electrically induced oxidation/reduction takes place with time scales on the order of seconds for applied bias voltages of 2.5 V. We infer the thickness of the films to be 30-60 nm using optical measurements, assuming the films have absorption coefficients similar to graphene during the absorbing (reduced) state. [38] We inspect the surface electronic properties of the two-terminal devices with an atomic force microscope (AFM), imaging the surface topography and conductivity before and after voltage pulses applied between its terminals. Two-terminal devices are subjected to voltage pulses (typically 2 to 3 V) while the tip is retracted. After the electrical reduction (or oxidation) process, the device contacts are grounded and the surface conductivity is imaged using a conductive AFM tip, using few millivolt tip bias. It is observed that the surface resistance of MLGO films decreases in the oxidized state, correlated with an increase in the optical transparency of the film (Figure 2.4a).

As the optical microscope of the AFM system did not produce clear images, the

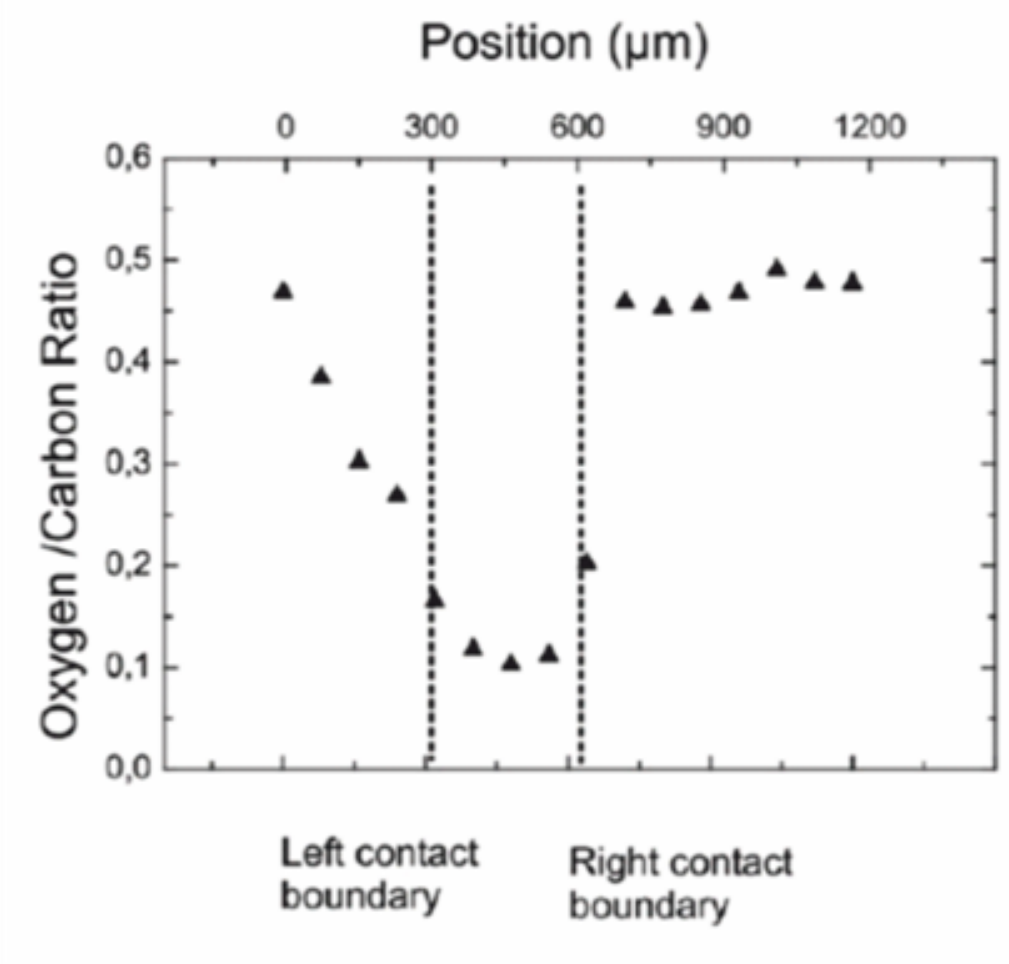

Figure 2.2: Oxidation and reduction are confirmed by XPS measurements. The oxygen-to carbon ratio is measured using a 100 μm diameter photoelectron collection spot and is plotted as a function of distance across the device. The data show gradual changes in the stoichiometry between the contacts.

changes in the optical transparency of the films are observed with the aid of the optical microscope in transmitted light mode in a separate experiment (Figure 2.4b).

It is observed that the transparent state corresponds to a mostly insulating surface with intermittent conductive domains. Upon application of a reducing pulse, the surface conductivity of the film greatly increases. It is seen that both the number of conductive domains and current per domain increase. When small currents (10 μA per mm wide films) are used, the reactions are slow and no significant topographical change is observed as verified by contact mode AFM images. This suggests that electrical changes are related to the chemistry of the films and not due to a mechanical reconfiguration. Rapid reduction and oxidation, however, result in delamination of the flakes as evident by increased instability in noncontact AFM images (data not shown). A sequence of optical micrographs shows that oxidation or reduction is not instant and not simultaneously taking place over the film area, but progresses as a front (Figure 2.5a). This is possibly due to the coupling of the potential distribution inside the film depending on the conductivity, which in turn is related to the degree of reduction. It is also observed that, when low (¡2 V) maximum bias values are used, reversible optical and resistive switching continue for multiple cycles (about 20 in our devices) before the film shows an irreversible reduction in electrical resistance. Our observations suggest that previously observed resistive switching in graphene oxide and graphene devices is a result of chemical modification of graphene due to reversible binding of oxygen[23, 24]. The drop-cast films consist of a large number of flakes. The thickness and conductivity of the films are not very uniform, and we attribute the device failure to formation of highly conductive dendrite-like shorting paths, which are observable in optical images (Figure 2.5b).

As the shorting paths are formed, current paths and voltage distributions inside the film change in a way that the bias needed for the reduction/oxidation process cannot be sustained uniformly and controllably at all parts of the film. We also investigate film surfaces in various oxidation states using high-resolution multifrequency electrostatic force microscopy. Since electrostatic force microscopy is

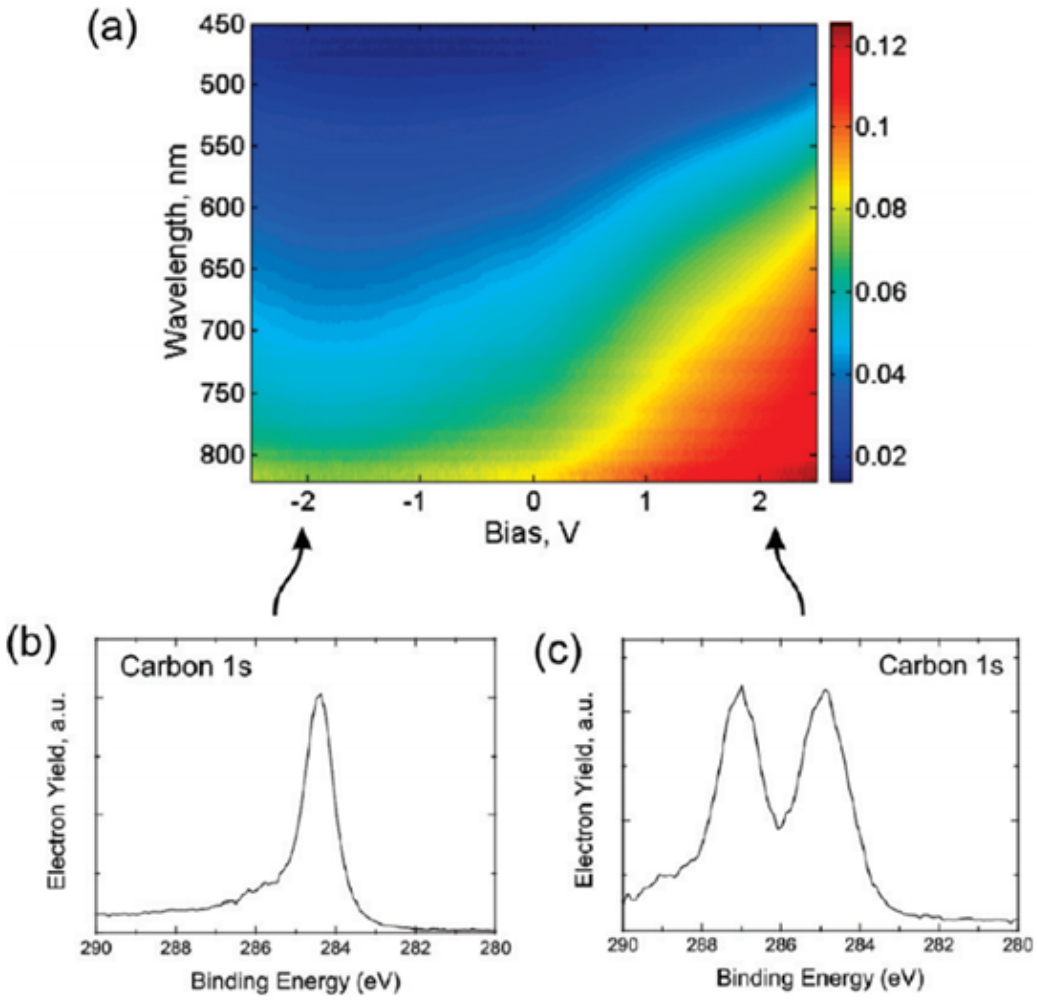

Figure 2.3: (a) Linear optical transmission of the films is measured using a 25 μm core fiber optic light collector near one of the contacts while the bias is swept between -2.5 and 2.5 V. It is observed that wavelength dependent transmission is adjustable by applying an external bias. Representative XPS spectra that correspond to the (b) reduced and (c) oxidized states show the correlation of optical transparency with stoichiometry.

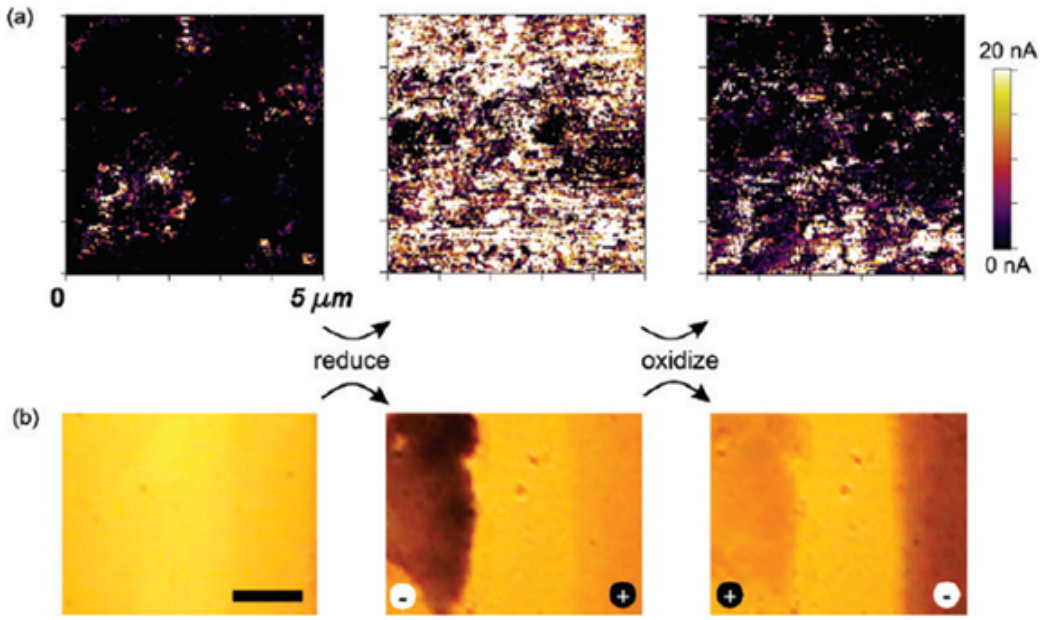

Figure 2.4: Figure 2.4: (a) Tunneling current images showing the effect of reversible electrical oxidation and reduction in three consecutive voltage cycles (+2 V, -2 V, +2 V for tens of seconds). The images are collected at the same location, by grounding the two contacts and applying a 10 mV tip bias. The surface conductivity is observed to switch in reduced and oxidized states. (b) Representative optical micrographs (observed by bright-field transmitted light, scale bar 30 μm) of multilayer graphene oxide films show spatially uniform transmission at the beginning of the bias cycles (left), where reduced transmission is observed upon application of bias that reduces the left side of the film (middle, minus sign, dark region). The optical transmission can be manipulated by reversing the polarity of applied bias and causing the left side to oxidize and the right side to reduce (right).

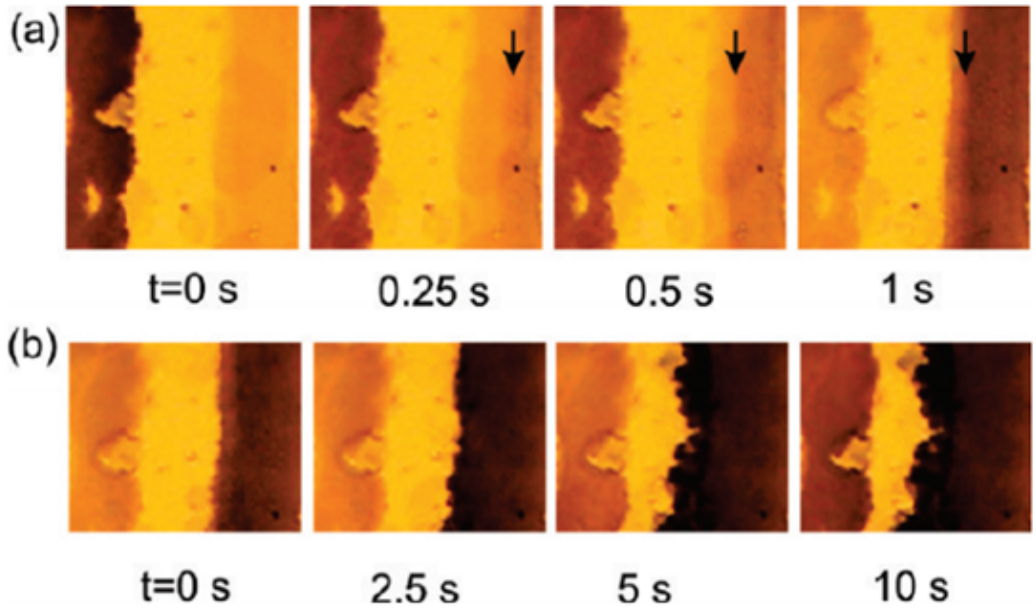

Figure 2.5: (a) Optical micrographs recorded as a function of time show the progress of reduction and oxidation upon sudden reversal of bias polarity. The arrows denote the presence of an advancing reduction front. (b) Failure of the device is observed upon application of a large bias (3 to 10 V for a given device geometry). Failure is due to advancement of dentrite-like conductive (reduced) regions, eventually causing a short in the device.

a noncontact and relatively nondestructive measurement technique, we use it as a reliable complementary way of confirming the surface electronic structure. In the electrostatic force microscopy images, we see that there are interconnected domains of different work functions on the PRGO films (Figure 2.6a, b).

Brighter pixels correspond to regions with more negative surface potentials, which we attribute to the presence of bound oxygen and hydroxide. Darker regions correspond to graphene-like channels and quantum dots. Sizes of the graphene dots show a distribution and vary from nanometer to micrometer scale in various states. These observations confirm that partial electrical reduction results in a graphene/graphene oxide heterostructure nanomesh, whose mesh size depends on the degree of reduction.

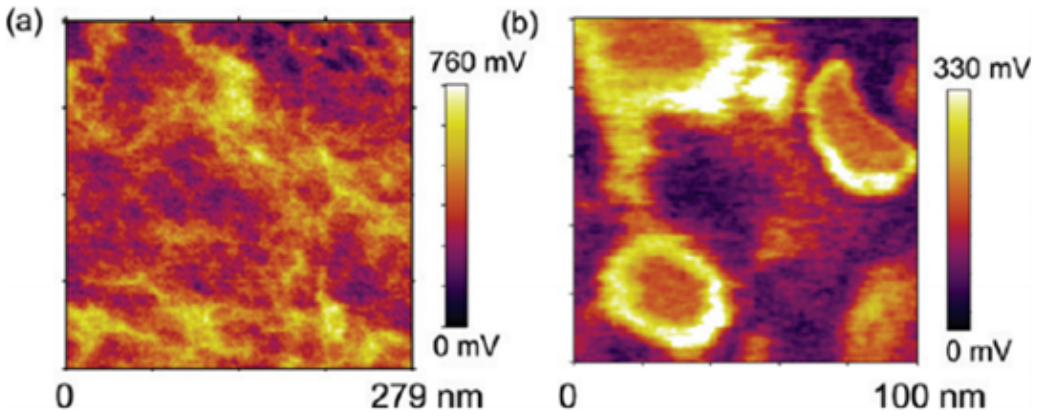

Figure 2.6: (a) Partially reduced graphene oxide films are investigated by multifrequency electrostatic force microscopy. Regions with different surface potentials are observed, suggesting the presence of a 2D graphene heterostructure where graphene and graphene oxide domains are simultaneously present. Electrostatic force amplitude is imaged, where bright regions correspond to lower surface potential, or greater oxygen content. (b) Higher resolution electrostatic force map shows that segregated regions with distinct surface potentials are present, with sizes ranging from few nanometers to tens of nanometers.

This observation is in accord with previous theoretical predictions. Uniform coverage of graphene oxide is not energetically favorable.[24, 25] Tip-induced electrical oxidation of graphene oxide is demonstrated by using a conductive AFM tip operated in the contact mode. Application of a positive sample bias (1-2 V) results in oxidation of graphene films, and resulting GO structures can be observed in the tunneling current image collected with a few millivolt tip bias (Figure 2.7).

No oxidation is observed for biases under 0.5 V. Reduction of MLGO is observed to occur when the sample is negatively biased. In order to monitor the changes in the electronic properties of the MLGO film surface as a function of bias, the tunneling current is measured between the Pt-coated AFM tip and the MLGO film while the sample potential is swept in a cyclic fashion (Figure 2.8).

The measurements demonstrate that the flake begins to reduce at relatively

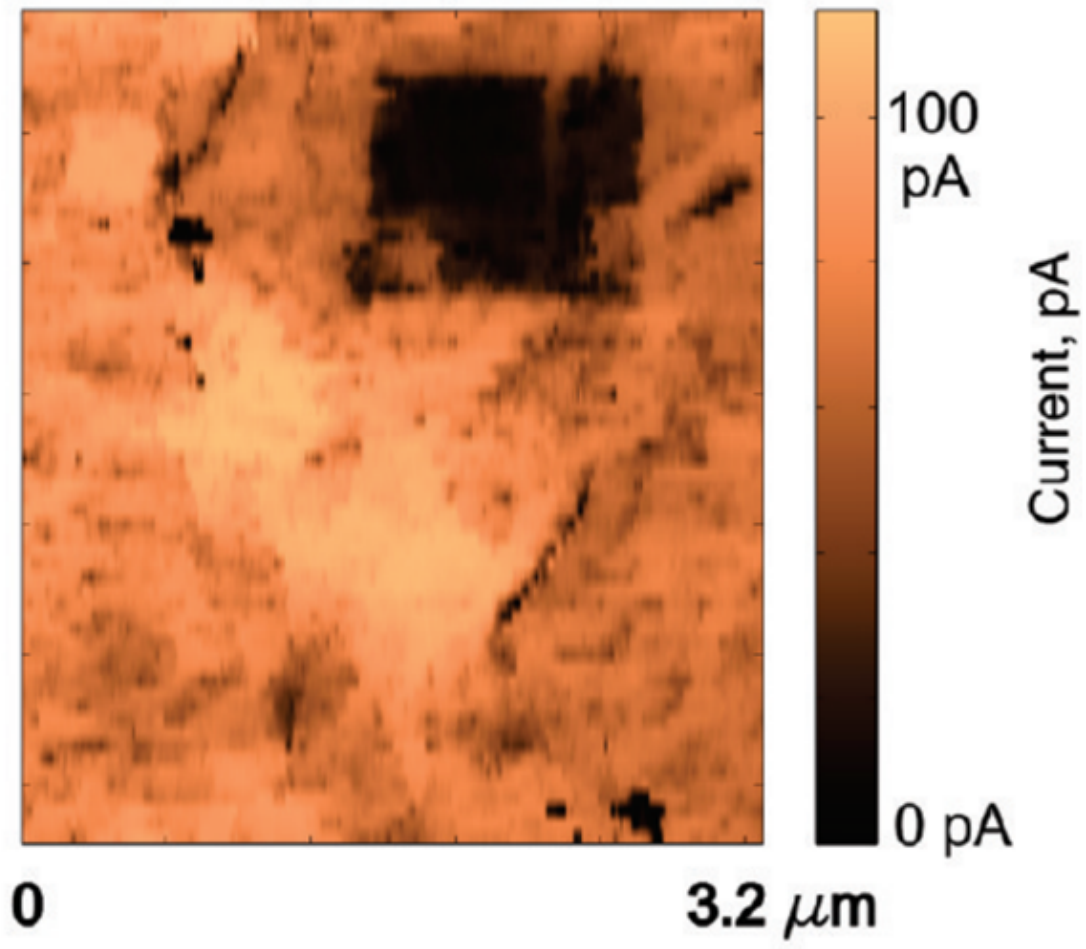

Figure 2.7: Due to the local electric field induced by a conductive atomic force microscopy tip, graphene can be locally oxidized.

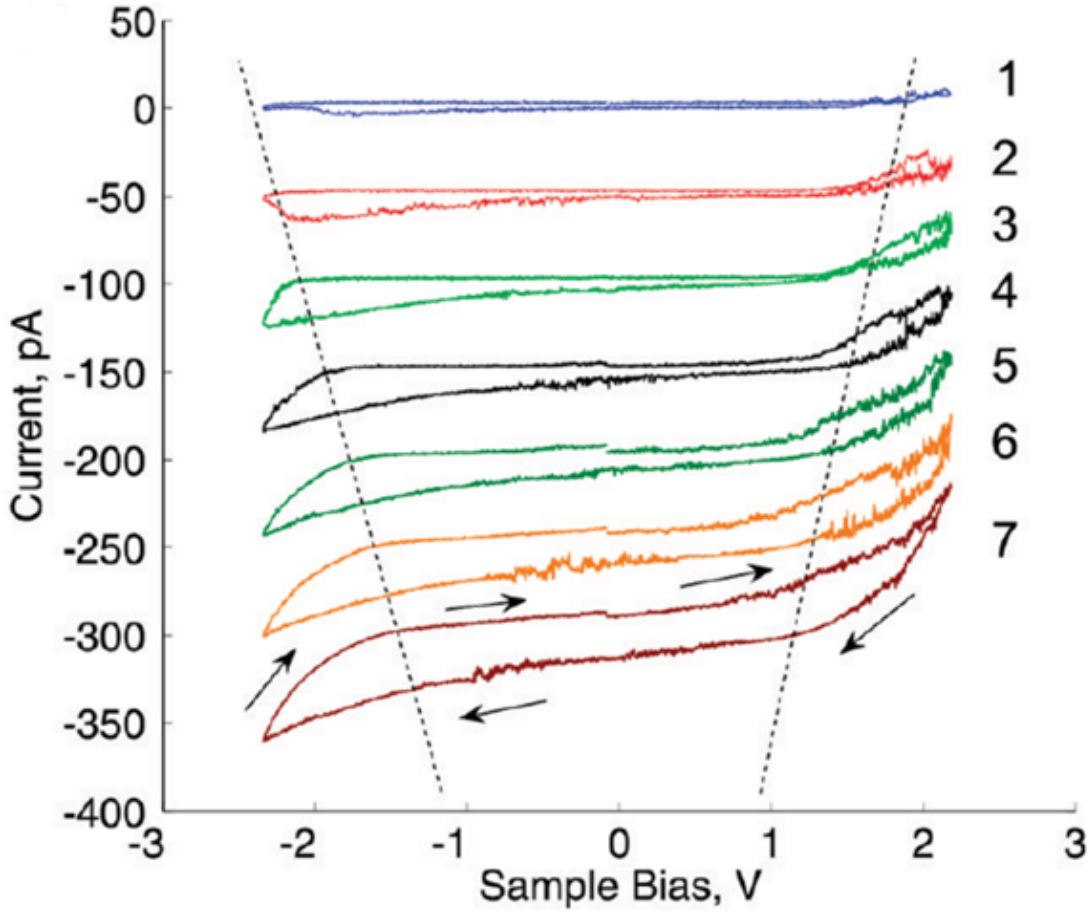

Figure 2.8: Cyclic current versus voltage (I-V) measurements are performed on multilayer graphene oxide films on Au/Pd film using a Pt-coated atomic force microscope cantilever. An increase of the current at smaller bias voltage after successive (1 to 7) I-V measurements suggests a decrease in the local effective band gap. Despite a symmetric voltage sweep, a net reduction effect is observed, suggesting that oxidation rate is smaller than reduction rate at similar magnitude bias.

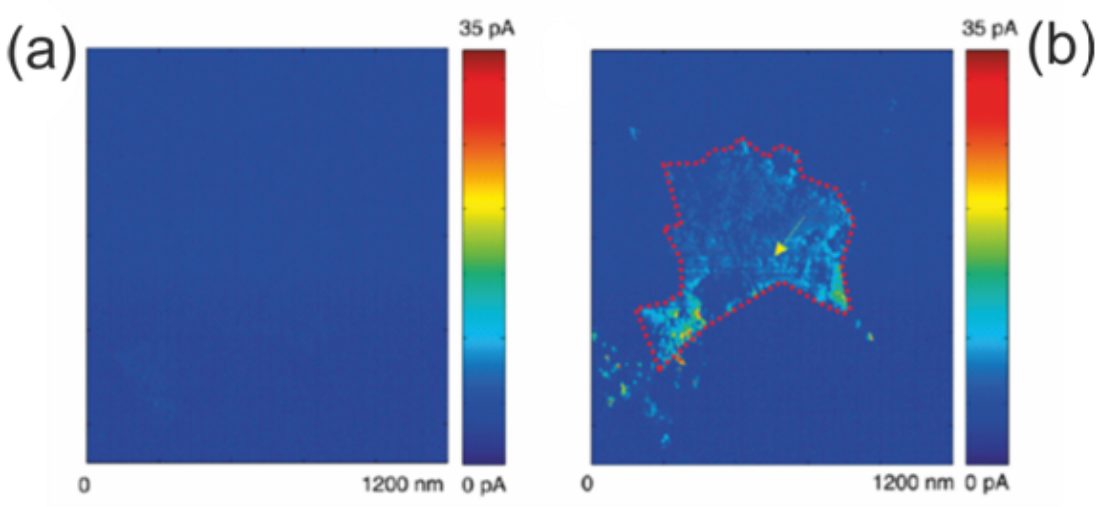

Figure 2.9: Tunneling current map after the first I-V measurement shows no or little surface conductivity. (d) Tunneling current map obtained after the 7^{th} I-V measurement shows increased current on one flake (or few flakes), suggesting whole individual flakes are reduced. Dashed red contour shows the reduced region and arrow denotes the location of the cantilever tip.

small current levels of few tens of picoamperes. Gradual decrease of the band gap during reduction is evidenced by changes in the positive and negative onsets of currents. Before and after the voltage sweeps, surface conductivity is imaged using a small bias (1100 mV), and a similar emergent heterostructured mesh of graphene/GO is seen on an individual flake (Figure 2.9 a and b). Reduction of the whole flake (or flakes, as highlighted by the red dashed line in Figure 2.9b) instead of a small spot right below the tip is possibly due to poor grounding of the topmost flake on the insulating MLGO film.

The reason for this is that the multilayer graphene oxide films are quite insulating and the effective resistance between the tip and the topmost flake is smaller than the effective resistance between the flake and the ground contact. Therefore, during application of the bias with the tip, whole flake is charged to a potential different than zero. The effective resistance within the flake is also smaller than the resistance between the topmost flake and underlying flakes. Therefore, the carriers injected into the flake diffuse within the flake and facilitate

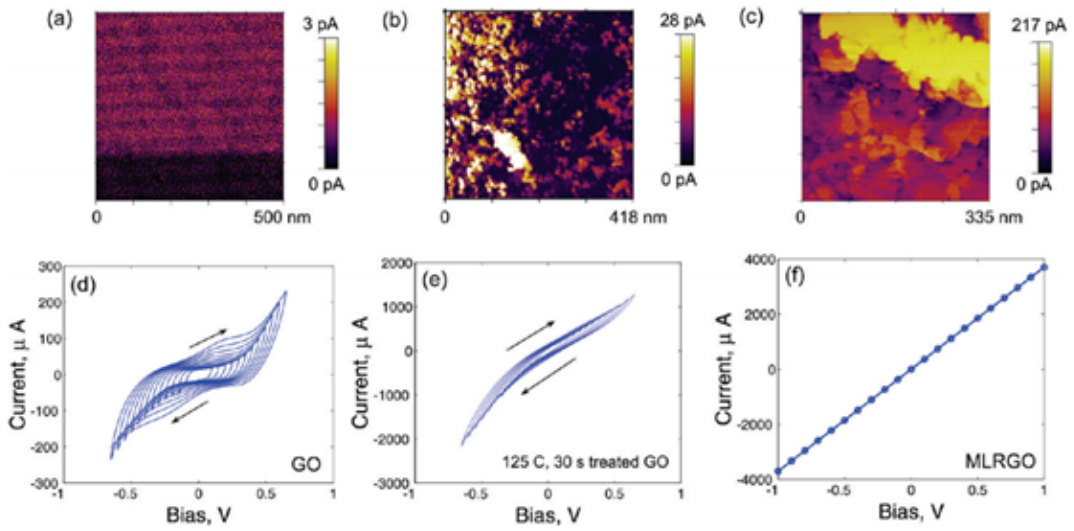

Figure 2.10: (a) Multilayer graphene oxide films, which have not been subject to thermal or electrical reduction shows low surface conductivity as observed by tunneling current maps obtained with a Pt tip (10 mV bias). (b) Upon partial reduction, conductive domains are observed in the tunneling current maps. (c) Tunneling current maps of chemically or thermally reduced multilayer graphene films show plateaus of current instead of conductive spots. (d) Cyclic current-voltage measurements are performed on two-terminal devices with unreduced graphene oxide. Hysteresis and changes in the I-V curves show that graphene oxide films feature both resistive switching and capacitive charge storage. (e) Hysteresis is decreased for two-terminal devices fabricated using partially reduced graphene oxide films, and (f) no observable hysteresis is present in multilayer graphene films obtained by complete thermal reduction (150 °C, few minutes thermal exposure) of graphene oxide films.

the electrochemical reaction, resulting in reduction of the whole flake. In contrast, tip-induced oxidation is performed on a relatively high conductivity film, and potentials are defined with higher spatial resolution. This is why the rectangle shown in Figure 2.7 is much better defined in shape than the reduced region of Figure 2.9b.

The time scales and voltages required for reduction and oxidation are also quite different; oxidation requires longer times and higher voltages. This suggests that the activation energies of reduction and oxidation are different. We assume that oxidation takes place by an electrochemical process within the water meniscus

formed between the tip and the sample, similar to tip-induced oxidation of various metals and semiconductors[39, 40, 41]. The observation that reduction takes place at very small current levels suggests that reduction is also an electrochemical process and not a thermal process. Oxygen coverage can be manipulated by applying electric fields in the noncontact mode as well (data not shown), suggesting that the electric field of the tip can also be used to manipulate the surface. Electron injection into graphene oxide is thought to facilitate the reduction, due to weakening of the bonds of negatively charge oxygen atoms with the graphene layer. The presence of states that trap electrons inside graphene oxide layers is evidenced by the charge storage effect observed in cyclic current-voltage measurements on two-terminal devices. A graphene oxide device with an apparently insulating surface (Figure 2.10a) shows nonzero current during a cyclic voltage sweep (Figure 2.10d).

Hysteresis observed in the I-V curves demonstrates charge storage (nonzero current at zero bias) and resistive switching (current asymmetry and change of the shape of the forward and backward sweep curves, around -0.2 V and 0.2 V in Figure 2.10d). Upon cycling the voltage with increasing maximum voltage levels, reduction takes place, accompanied with resistive switching. Upon further reduction, conductive islands begin to form on the surface similar to those observed for thermal PRGO films (Figure 2.10b). For the PRGO films, the hysteresis in the current-voltage curves is reduced (Figure 2.10e). Chemically or thermally reduced multilayer graphene film surfaces do not have conductive dots on the surface (Figure 2.10c), and they do not display charge storage or resistive switching effects (Figure 2.10f). It must be noted that we were not able to observe reversible oxidation when we start with films of chemically reduced graphene. This may be due to the high conductivity of such films and resulting inability to establish significantly differing potentials within the film. The results show that electrical charge has a strong effect on the thermodynamic equilibrium of graphene/ oxygen system. In ambient atmosphere, positive charge causes oxidation of graphene, and negative charge enhances the reduction of graphene oxide to graphene. Graphene oxide flakes are unstable and slowly decompose to partially reduced graphene oxide. The decomposition process is slow at room temperature. For instance, it is observed that graphene oxide suspensions start to darken in

a few months at 25 °C, which indicates the partial reduction of graphene oxide. However, negative charging effectively increases the free energy change (G of the decomposition reaction). Increased driving force (G) greatly enhances the rate of the reaction, and it is possible to completely reduce graphene oxide in a few seconds. Also, for the oxidation case of partially reduced graphene oxide, the reaction is not spontaneous under ambient conditions and temperature. When graphene is positively charged, the oxidation is spontaneous. The reaction rate is observed to depend on initial oxygen coverage of graphene and is slower for graphene-like films. Both graphene quantum dots are formed and oxygen coverage change during the electrical reduction. The equilibrium size distribution of the quantum dots can be controlled with the applied voltage. In order to determine the equilibrium stoichiometry and structure, the partition function must be written for the graphene/graphene oxide system, also including the electrostatic energy due to the presence of excess charge. Oxygen is known to bind to graphene in a number of different configurations, resulting in different band gaps and binding energies[24]. The binding energy of individual oxygen atoms on graphene is also a function of coverage, as well as being dependent on the actual binding configuration (bond type) and presence of neighboring oxygen atoms[25]. A thorough thermodynamic analysis of the phenomenon, as observed under ambient conditions, must take into account the myriad configurations of binding of oxygen, hydrogen, and hydroxide, in the presence of excess charge. Such an analysis must involve ab initio calculations of total energy for a large number of configurations with a large number of atoms. We do not attempt to perform such an analysis in this thesis.

Chapter 3

Tunable Ultrafast Optical Response of Graphene Oxide

3.1 Introduction

Ultrafast dynamics and nonlinear optical response of graphene has been the subject of considerable research[42, 43]. Graphene is known to exhibit wideband nonlinear saturable absorption SA. It is accepted that due to Pauli blocking, nonlinear absorption NA in graphene is not allowed.

Graphene oxide GO is an insulator, with an effective energy gap that depends on the stoichiometry[44, 25]. In GO, it was found that two-photon absorption dominate the NA for picosecond pulses, whereas for nanosecond pulses excited state absorption also influences the nonlinear response.[45], It has been previously observed that, GO can be reduced controllably by annealing at below 300 °C low-T in ambient atmosphere.[26, 27] Interruption of the annealing results in partially reduced GO PRGO. GO has been reduced by exposing to a photographic camera flash [28], or femtosecond laser.[46], Very recently, we studied reversible electrical reduction and oxidation of GO.[47], Nanoscale inspection showed that GO islands segregate within graphene, and a two-dimensional heterostructure nanomesh forms during electrochemical oxidation. Here, we study the effect of

the oxidation level on nonlinear optical properties of GO. We demonstrate that both electrochemically induced reversible reduction and optically induced photoreduction in GO result in changes in the nonlinear optical properties of GO thin films. We present the carrier dynamics and nonlinear optical properties of such films, studied by ultrafast wavelength-dependent pump-probe spectroscopy. We show that ultrafast response of GO can be tuned by both reduction procedure.

3.2 Experimental

The preparation, characterization, linear optical, and electrochromism properties of GO were very recently reported in Chapter 2. We study the electrical reduction in GO in air, using multilayer GO thin films deposited on metalized glass substrates. The two terminal devices consist of thin 10 50 nm Pd/Au planar contacts, separated by 0.30.6 mm, with a thin multilayer GO film covering both contacts and in between Figure 3.1a. The degree of chemical reduction and linear absorption spectrum can be tuned by applying a fixed voltage difference to the contacts. A gradual increase in the absorption edge as a function of applied bias is observed.[47], During the cyclic voltage sweeps, it is seen that the linear optical transparency of the films change between partially opaque and transparent states. Electrochemically induced oxidation/reduction takes place within a time scale on the order of seconds for applied bias voltages of 2.5 V. We infer the thickness of the films to be 3060 nm using optical measurements, assuming the films have graphene like optical absorption during the reduced state. Wavelength-dependent pump probe measurements were performed by using Ti:sapphire laser amplifier-optical parametric amplifier system Spectra Physics, Spitfire Pro XP, TOPAS with 44 fs pulse duration and 1 KHz repetition rate. Commercial pump probe experimental setup with white light continuum probe beam Spectra Physics, Helios was used. Experiments were performed with 400, 590, and 790 nm pump wavelengths. Pulse duration inside pump-probe experimental set up was measured via cross correlation of pump and probe pulses and it was found to be around 100 fs. Positive sign of pump probe data A=T/T0 corresponds to NA whereas negative sign of A corresponds to SA in our convention.

3.3 Characterization and ultrafast optical response

We investigate the ultrafast optical response of the films while the voltage bias is applied. A film left in the oxidized state after multiple redox cycles is characterized by the pump-probe technique. Figure 3.1 shows normalized change in the absorption of the white light continuum spectra, measured using 790 nm, 0.5 J pump energy with a typical pulse width of 100 fs, upon application of a time varying voltage profile shown in Figure 3.1b. Although initially SA is dominant over the whole spectrum, NA appears rapidly in a matter of seconds upon oxidation Figures 3.1c and 3.1d.

We attribute this to an increase in the degree of oxidation of GO, causing SA to gradually switch to NA for short probe wavelengths, possibly due to modification of the band-structure of the material. The oxidation state can be controlled electrochemically and GO can be reduced by application of a negative bias Figure 3.1c. Even when electrochemically or thermos-optically induced partial reduction takes place, we still observe NA at longer probe wavelengths 750 nm, suggesting only a partial reduction in GO. Application of a 2.5 V bias causes the advancing of SA behavior toward longer wavelengths, suggesting the presence of a stoichiometry-dependent effective band-gap.
The ultrafast response can therefore be modified upon application of the bias. The experiments were performed with different pump wavelengths, and similar results with varying decay times and modulation depths are observed.

Figures 3.2a and 3.2c show differential absorption of probe 430780 nm with simultaneously applied pump 0.5 J, 400 nm, 44 fs for GO; without applying bias, applying 2.5 V for 5 s and applying +2.5 V for 5 s, respectively. It is clearly seen that the ultrafast optical absorption of the samples can be switched from SA to NA reversibly depending on the wavelength and degree of the reduction. We also performed similar experiments using femtosecond pulses 5 J, 400 nm, 44

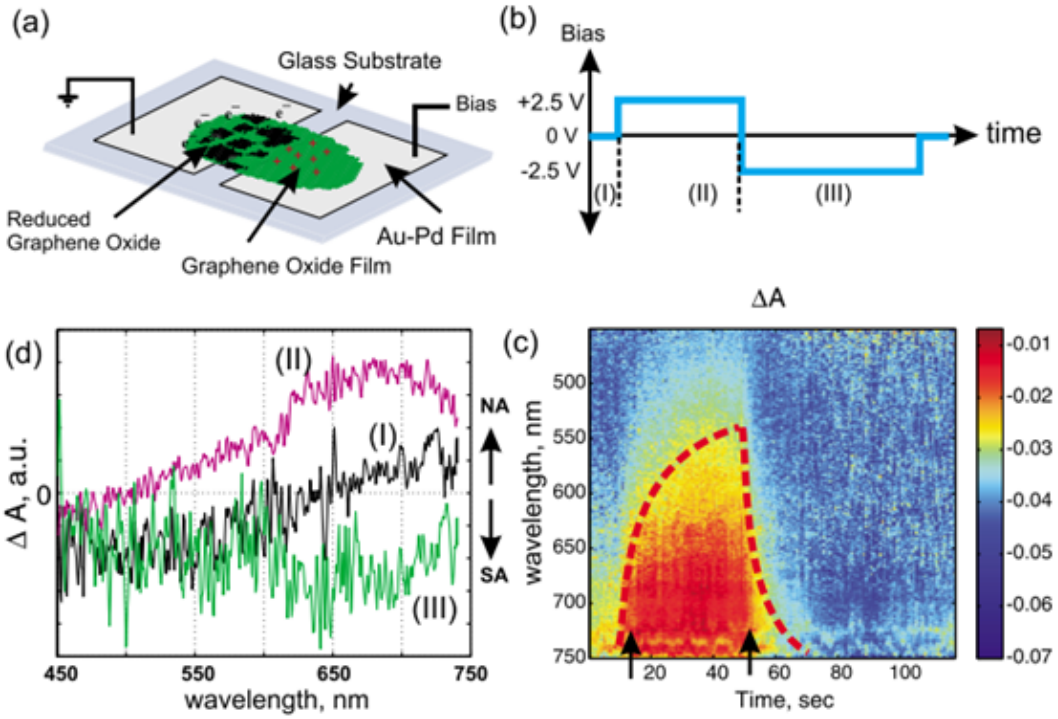

Figure 3.1: Color online schematic description of the device used in the measurements. (b) The applied bias voltage profile and (c) normalized differential probe transmission A as defined in text are plotted as a function of wavelength and time. Wavelength dependent switching between saturable and NA is observed upon application of the bias pump excitation energy of 0.5 J, center wavelength of 790 nm, pulse width of 44 fs. The dashed lines are guidelines for the eyes, delineating the transition wavelength between saturable and NA. (d) Differential absorption A plotted as a function of wavelength for three representative points with different bias conditions regions I, II, and III in cshowing NA and SA.

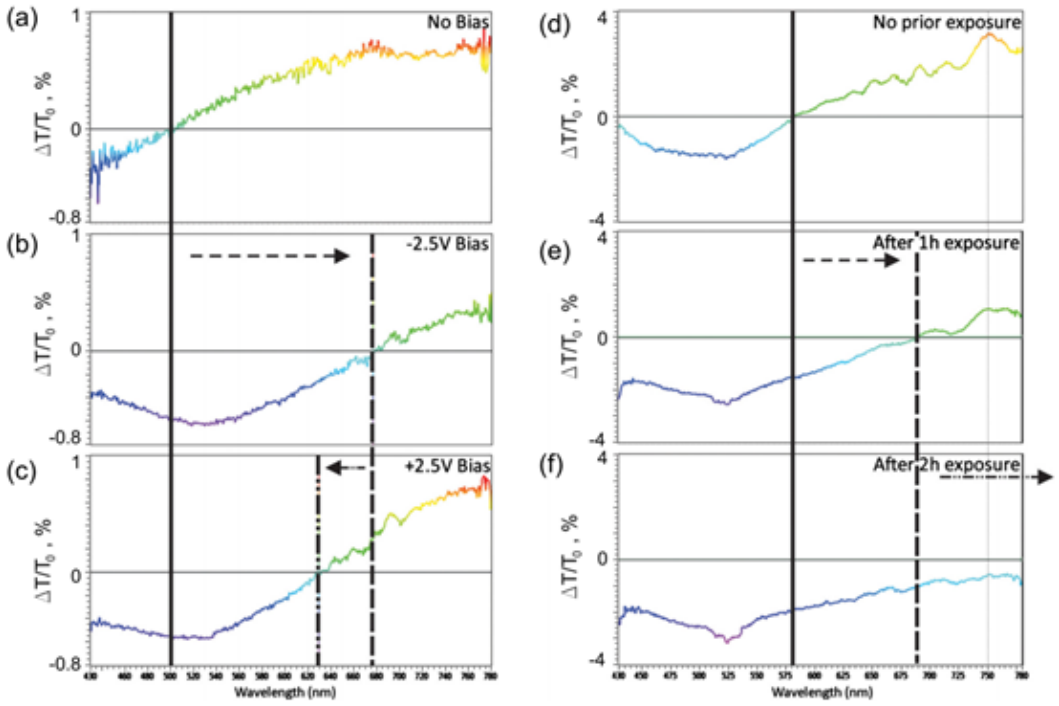

Figure 3.2: A color online differential absorption of probe at zero pump-probe delay. ac show voltage bias dependence. df Changes in the response upon high-intensity pump exposure for various durations. Similar changes are observed for electrochemical and photothermal reduction.

fs without applying bias. Figures 3.2d3.2f show differential absorption of probe 430780 nm with simultaneously applied pump for GO, without prior exposure, after exposing to pump for 1 h and for 2 h, respectively. Photo-reduction in GO takes places by exposing high intensity femtosecond pulses and this process is irreversible.

Applying high intensity femto-second pulses and negative bias causes similar effects on the differential absorption characteristics of GO. At intermediate oxidation stoichiometry is achieved by application of a 2.5 V bias or by exposing to high intensity femtosecond pulses, if the probe wavelength is chosen near the SA/NA transition, NA signal starts appearing within the SA signal region Figs. 3.3a and 3.3b. For example, as seen in Figure 3.3a, the NA peak appears within 100200 fs of the arrival of the pump pulse. Such a time scale between the carrier-carrier scattering and carrierphonon scattering causes the NA process disappears in a very short time, leaving the tail of carrierphonon scattering visible. In a simplistic view, it can be assumed that the simultaneous appearance of SA and NA is the result of isolated regions of the material acting as graphene and GO. The optical response is averaged over the 300 m diameter illumination spot-size and the material behaves like an effective material with multiple components. In such a case, the persistence of NA for a variety of pump wavelengths even when the pump photon energy is less than the apparent absorption edge of GO, requires that multiphoton absorption or absorption of the probe through intermediate states must be present.

Previous reports on observations of simultaneous presence of SA and NA in graphene offered an explanation in terms of doping of the graphene layers. Switching as a function of the probe wavelength from saturation to NA was observed around 1.78 m for doped epitaxial graphene on SiC[48]. The NA of the probe seen at longer wavelengths and saturation seen at shorter wavelengths were attributed to the shifting in the Fermi level due to doping. As molecules bind to the surface of the graphene, depending on the molecule and the binding location graphene experiences a charge transfer as a donor and acceptor, thus changing

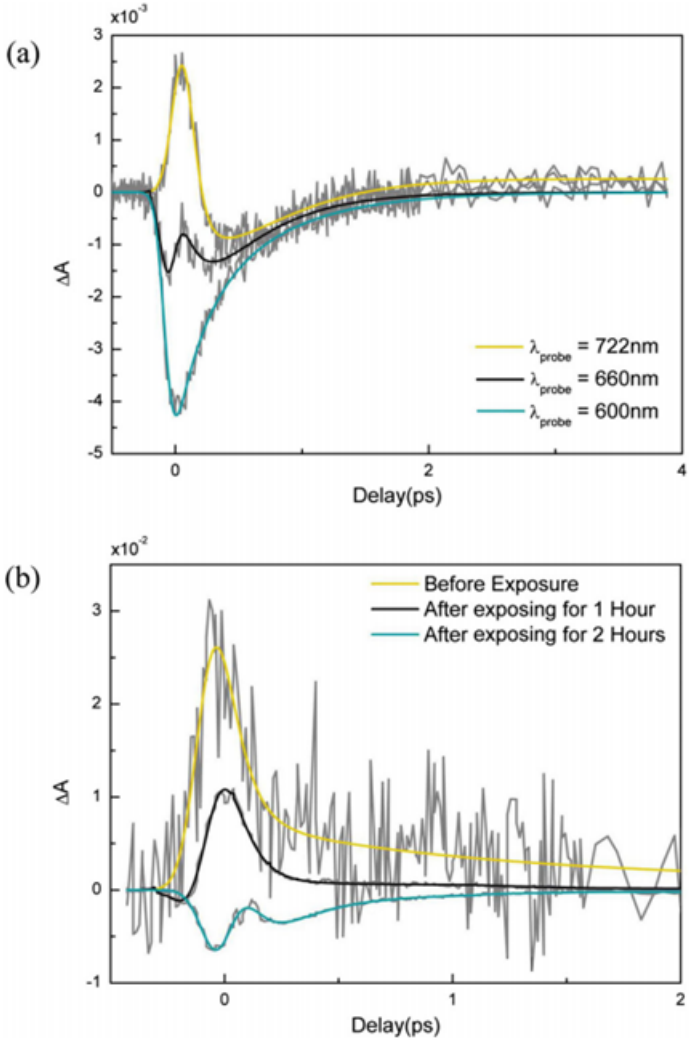

Figure 3.3: Color online (a) temporal behavior of the saturated and NA responses at different probe wavelengths after applying bias voltage. (b) Temporal behavior of the saturated and NA responses at 750 nm probe wavelength depending on the exposure time to pump pump excitation energy of 5 J, center wavelength of 790 nm, pulse width of 44 fs.

the Fermi level, carrier density, and electrical resistance of graphene[49]. In addition, the band structure itself may be modified depending on the type, location, and density of the binding species[25]. In our case, the observed NA/saturation behavior may be attributed to such modifications of Fermi level or band structure upon electrochemical stimulus. The zero crossing wavelengths can be tuned from 550 nm to beyond 800 nm our probe range. Although the exact origin of the electrochromic effects in the ultrafast regime is disputable, due to the SA/NA cancellation effect, for carefully chosen pump-probe wavelength and degree of reduction combinations, the nonlinear response of graphene can be tuned to display a very fast 100 fs effective NA decay time constant.

Chapter 4

Surface-Enhanced Raman Spectroscopy of Volatile Organic Compounds

4.1 Introduction

Raman spectroscopy is a valuable tool commonly used in the characterization of chemical substances. During the interaction of light with matter, small ($\approx 10^{-7}$) percentage of photons scatters in-elastically. Photons interact with the vibrational states of the material and an energy exchange occurs between them. During scattering, energy transfer between photons and vibrational states is called Raman Scattering and measuring the energy change of the scattered photon is Raman Spectroscopy. It is possible to identify materials by using their Raman spectra because each material has its own vibration energy states. However, it is hard to characterize materials with low concentration with Raman Spectroscopy due to low statistics of this physical phenomenon. Plasmonic nanostructures enhance absorption and increase the number of inelastic scattered photons [50, 51]. Therefore, Raman signal increases when samples placed on plasmonic surfaces. This technique is called SERS (Surface-Enhanced Raman Scattering). SERS

makes it possible to detect and characterize chemicals with low concentration also [52, 53].

Volatile organic compounds (VOCs) are organic molecules that have high vapor pressure at room temperature. VOCs evaporate and condense onto substances. There are variety of VOC sources such as paints, coatings, chlorofluorocarbons and cleaning products. VOCs are also important molecules for eviroment . Detection of VOCs has several practical applications such as explosive detection, opto-electronic nose for drugs and breathe analysis. In this thesis, we have focused on detection VOCs by using SERS.

4.2 Chemical synthesis, fabrication and characterization of SERS substrates

We have used a chemical synthesis method to fabricate SERS substrates. Due to the high enhancement factor used in SERS, we needed a process with minimum residual chemicals. Therefore, we have used a synthesis method developed for conductive ink application [54]. The chemical reaction is shown below. We have prepared a paste and drop cast the solution on a clean glass substrate. As shown in the equation, the included chemicals decompose spontaneously. After room temperature drying of the silver based paste, all the residuals evaporate and a rough silver layer was plated on the surface. The final products are solid silver and volatile compounds. After 6 hours drying of the film, we have measured the SERS performance. We observed that enhancement factor of the substrate is adequate enough; however structural uniformity is not enough for the applications that are aiming to do.

We have decided to do the rest of the experiments with a more simple, uniform and clean technique to fabricate SERS substrates. In this technique, we have evaporated thin films of silver onto glass substrates. Nanoparticles formed on the surface because of the surface tension of silver. The particle size depends on the thickness of the evaporated film. Additionally, the formed nanoparticles are close to each other as shown in the Figure 4.1. Because of the short distance between

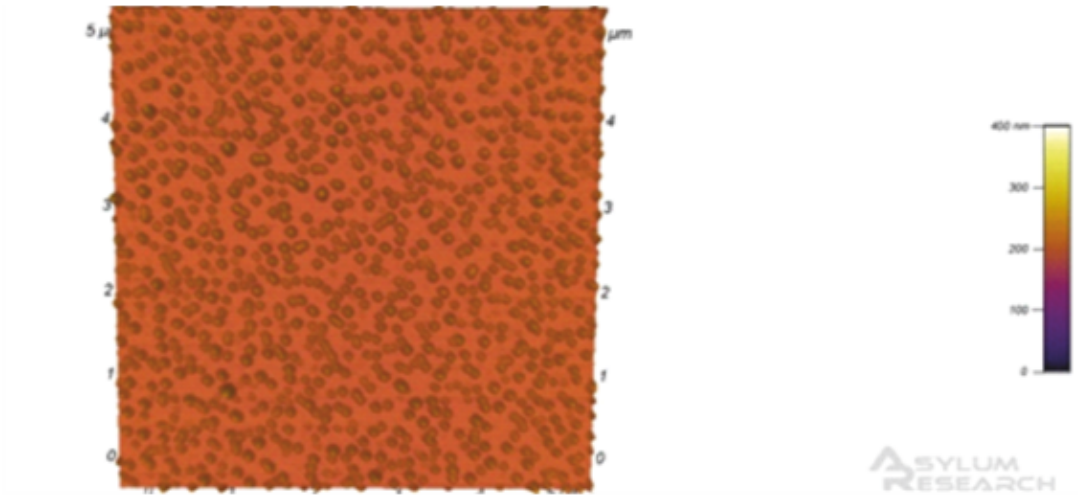

Figure 4.1: Image of 3nm silver coated glass slide.

particles, they behave like a coupled waveguide that enhances the absorption and forms hot points. Our Raman microscope uses a laser with a wavelength of 532 nm for excitation. Therefore, we have optimized maximum absorption of the silver film to be around 532nm. Figure 4.2 shows the wavelength vs absorbance of 3nm thickness silver film on glass. Silver film has a good match with laser wavelength as shown in the Figure 4.2. However, the most important drawback of silver is quick oxidation which decreases repeatability of the experiments. In the Figure 4.3, we have measured absorbance change with time. Experiments should be done with newly prepared samples to make repeatable experiments,. Addition to its oxidation problem, substrates are very sensitive to heat also. Laser radiation and elevated temperatures cause nanoparticles to accumulate. In the Figure 4.4, we have measured the effect of heat treatment on silver films. Due to increased mobility, average particle size has increased and absorbance shifted through red.

4.3 Single molecule sensing with SERS

Plasmonically active substrates have been fabricated for SERS experiments. We have fabricated metallic nanostructures by using different techniques including

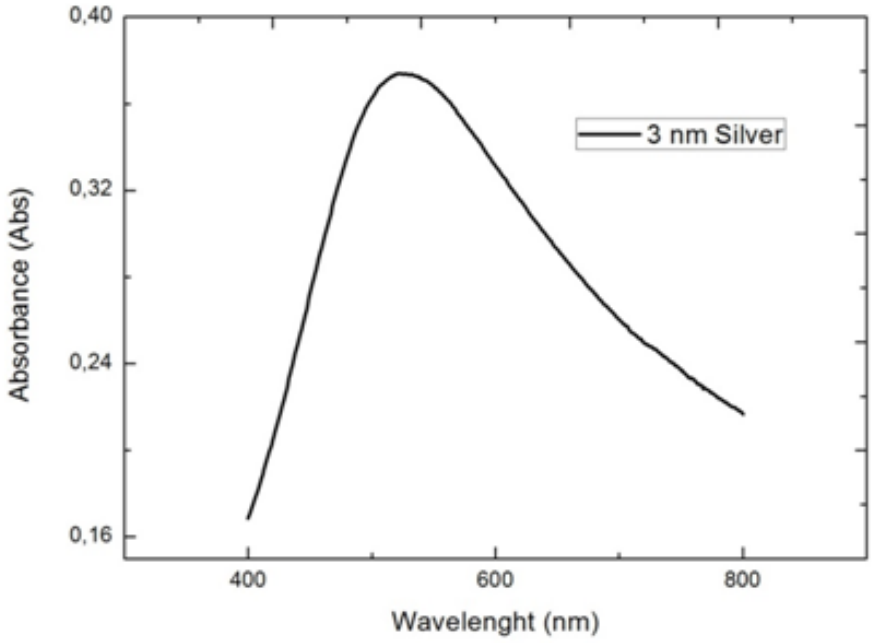

Figure 4.2: Absorbance vs wavelength of 3nm silver coated glass slide.

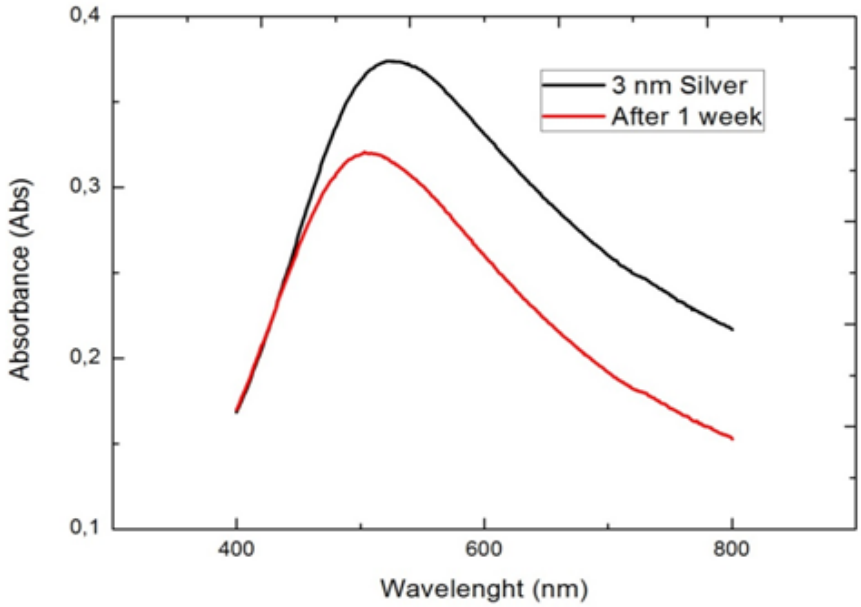

Figure 4.3: Absorbance vs wavelength of 3nm silver coated glass slide just after fabrication and 1 week after fabrication.

chemical synthesis and evaporation. At the start of the experiments, we have recognized an interesting phenomenon. On blank SERS substrates and with low laser power, we observed blinking in Raman signal. The blinking is independent from technique used in the fabrication of SERS substrate. Raman spectra measured during blinking were similar and coming from unknown substances possible originated from ambient atmosphere. We recognized that those fluctuations in Raman spectra were coming from VOCs molecules. The reason of the blinking is surface diffusion causes VOCs to enter and exit hot spot.

Previously, similar fluctuations in Raman spectra have been observed [52, 55, 56]. Those fluctuations regarded as single molecule SERS spectra. We have also observed similar SERS spectra in ambient atmosphere with high quality factor. However, Raman spectra of blank substrates are very complicated and hard to manipulate manually. The main reason is Raman spectrum of a substance on a SERS substrate is different than its bulk Raman spectrum [51]. And SERS spectra could depend on the molecular orientation. We have developed an analysis algorithm to identify the signals coming from SERS substrates, and used the

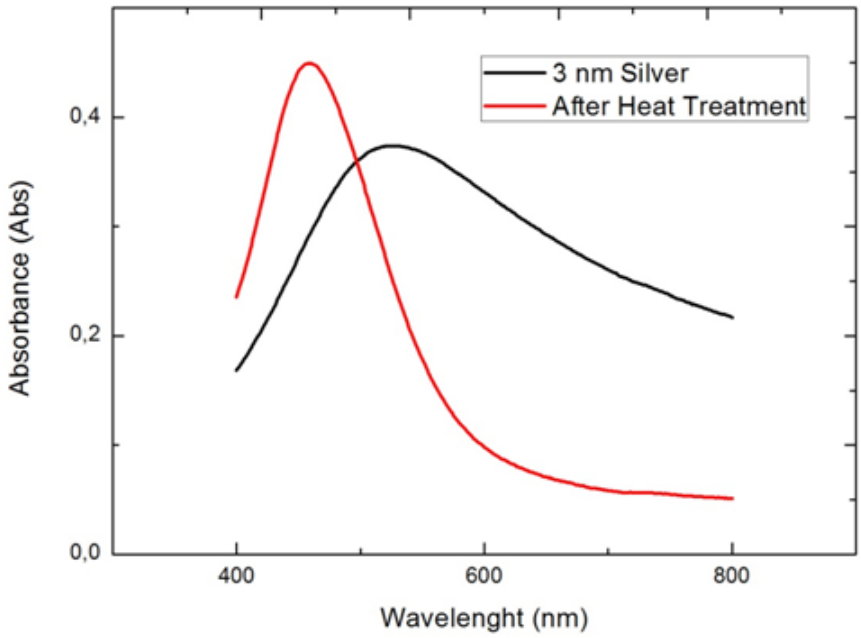

Figure 4.4: Absorbance vs wavelength of 3nm silver coated glass slide and after heat treatment.

algorithm to identify VOCs.

We have made experiments to reveal the mechanism and to identify airborne molecules. In the Figure 4.5, a common time vs total Raman intensity graph of a black SERS substrate is shown. We have covered silver surface with a monolayer of 4-MBA(4-Mercaptobenzoic acid) to isolate silver from ambient atmosphere. As shown in the Figure 4.6, we did not see any blinking as shown in the graph when the surface is covered by a self-assembled monolayer. This supports that blinking is originated from the free molecules diffusing on the substrate surface. Interactions of the molecules with the SERS substrate could change their Raman spectra also. 4-MBA acid physically binds to the silver surface due to its thiol group. We observed that Raman spectra shifted when 4-MBA interacts with the surface. In the Figure 4.7, Raman spectrum shifted to red as predicted by the simulation results [57] due to physical interaction of 4-MBA with the surface during its surface diffusion. This experiment showed that, it is possible to measure real time molecule-surface interactions by using SERS spectra.

Raman spectra also include florescence and scattered photons other than Raman. Raman signals of diffusing molecules should be isolated from total signal to identify unknown VOCs. Therefore, we have taken derivative of the Raman spectra to see the changes made by hoping molecules. In the Figures 4.8a and 4.8b, original vs derivative times series of total Raman signal is shown.

To identify Raman spectra of VOCs, we have modified the algorithm to find the most abundant spectra. The result was interesting. We have identified the spectrum by using Raman databases and it was identified as 3-(4-tert-Butylphenyl)-2-methylpropanal. It is kind of a fragrance molecule that is commonly used in cleaning agents. We traced the chemical and found that the laboratory was cleaned with a product includes 3-(4-tert-Butylphenyl)-2-methylpropanal which proves we have built an artificial nose can detect fragrances. We purified the fragrance molecule and dissolved it in an organic solvent to make controlled experiments. However, no matter how high the vapor pressure was, we could not see a linear increase in the Raman signal; i.e, the signal could not be saturated.

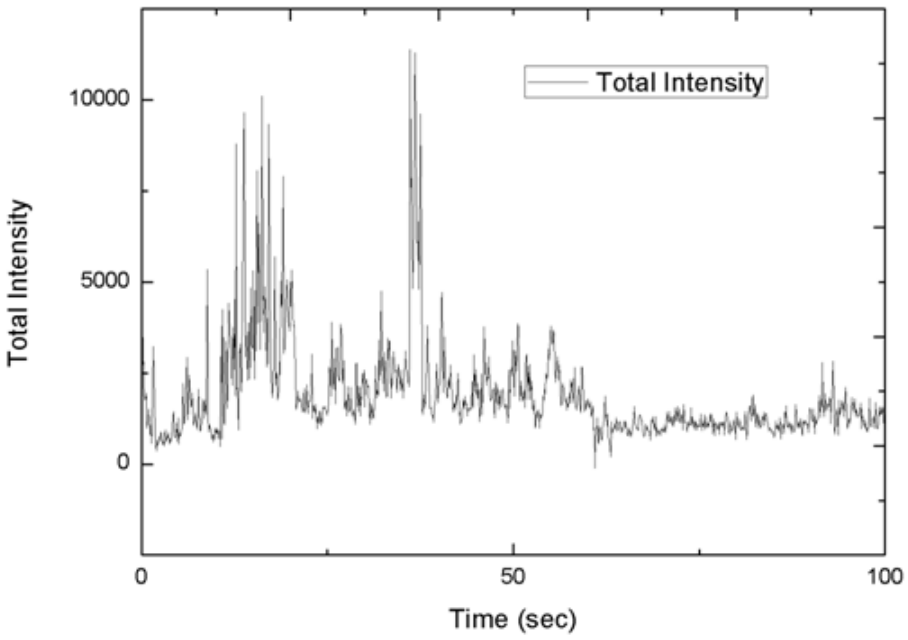

Figure 4.5: Total intensity of Raman signal vs time of a blank SERS substrate.

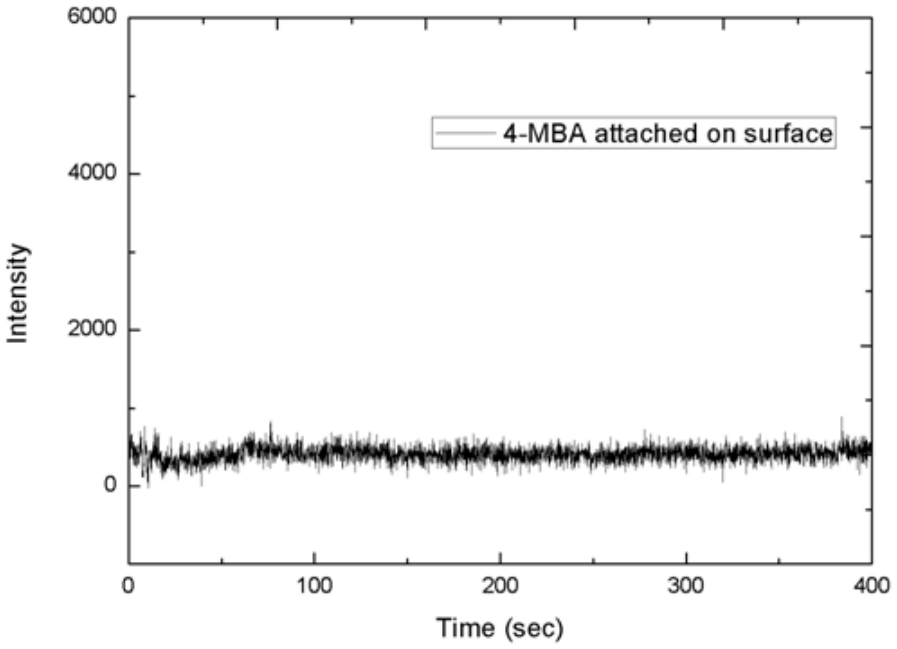

Figure 4.6: Total intensity of Raman signal vs time of a SERS substrate covered by 4-MBA monolayer.

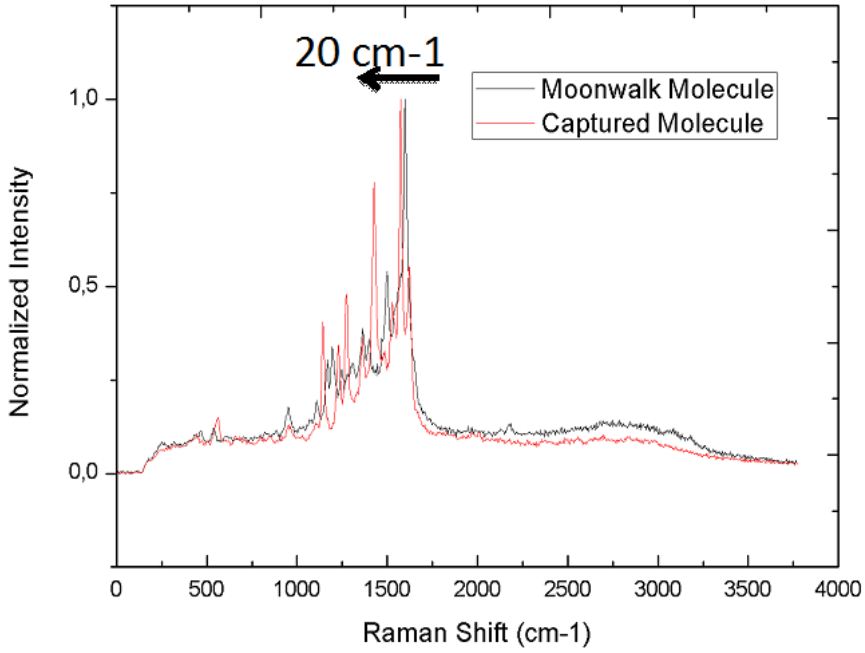

Figure 4.7: SERS spectra of 4-MBA. When 4-MBA goes into physical interaction with the silver surface, total spectra shifts to the left.

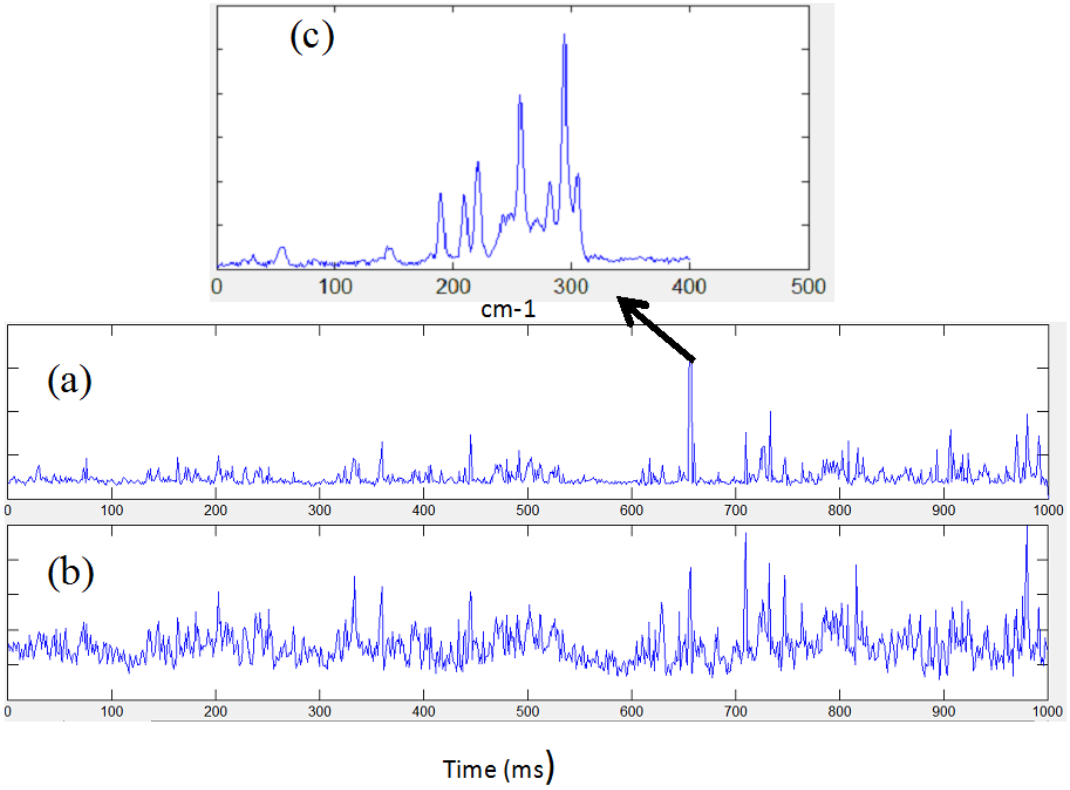

Figure 4.8: (b) Time vs total intensity Raman signal of blank substrate. (a) Time vs differential of Raman signal. (c) Raman spectrum at the peak shown by black arrow.

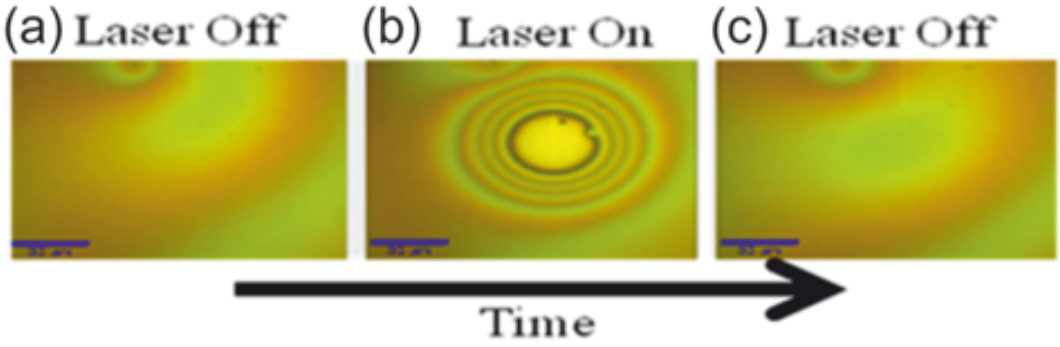

Figure 4.9: Microscope image of fragrance thin film on SERS substrate. (a) is unexposed film, (b) Laser light induces a repelling force, (c) Laser is closed and thin film covered the surface again.

We have dip-coated substrate surface with purified fragrance to measure the Raman spectrum of the bulk sample. We observed that the surface repels the fragrance thin film with a light driven force (Figure 4.9). When the light is on, a hole appears on the film. The change on thin film was reversible. Based on these results, light driven force repels excess amount of chemicals from surface and prevents saturation. This phenomenon enables us to characterize a mixture of chemicals at the same time which is not possible in mammalian olfactory system and most of the artificial noses.

We have done experiments to develop this technique to detect explosive vapour from air. However, identifying molecules from SERS spectra is difficult because of the difference between bulk vs SERS spectra. We need to know exact SERS spectra of the compounds to manipulate their spectrum from total signal. We contaminated air with well-known materials to measure SERS fingerprints of them. Different materials were encapsulated with SERS substrates. In the encapsulation, due to vapor pressure of the materials, volatile materials are supposed to evaporate and condense onto SERS substrates which allowed us to measure SERS fingerprints during surface diffusion.
We have achieved to measure SERS fingerprints of some materials by taking the average of total time series of encapsulated substrates. The SERS fingerprints of the materials are shown in the Figures 4.10, 4.11 and 4.12. We have applied a

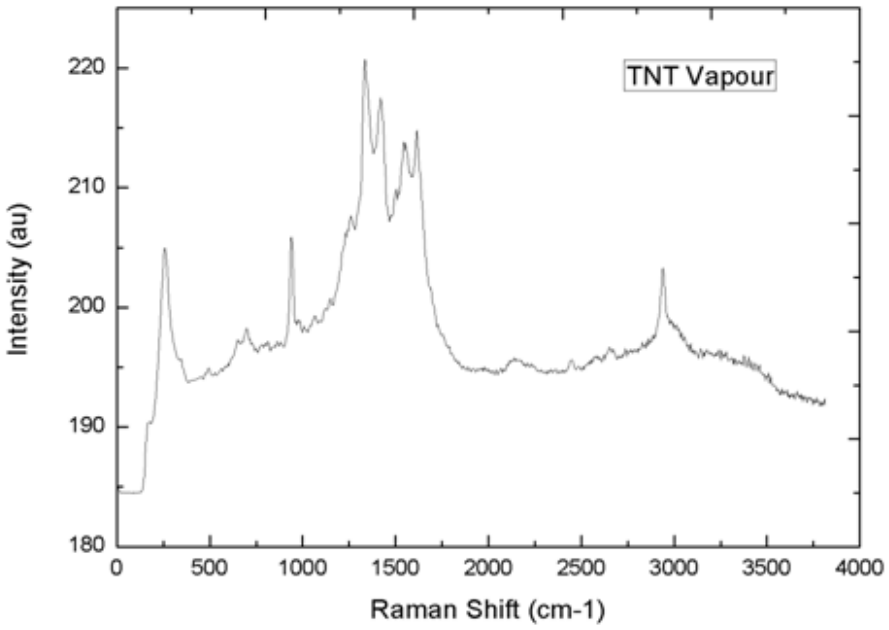

Figure 4.10: Average surface-enhanced Raman spectrum of TNT.

filter to Raman spectra which only multiplication of the major peak positions of average SERS spectrum of TNT is shown. This means that when a TNT enters to the hot spot, it should give a Raman spectrum similar to the previously measured SERS fingerprint of TNT, consequently a peak should be observed in the filtered times series as shown in the Figure 4.13. With this technique, it is possible to count TNT molecules that came to the hot spot. In the Figure 4.14, SERS spectra of the highest peak in Figure 4.13 and SERS fingerprint of TNT molecule is compared. Similarity between the fingerprint and actual spectra proves that our filters are working correctly.

To sum up, we have demonstrated single molecule sensing of airborne molecules with Raman spectroscopy. Sensing mechanism is based on Raman scattering of hoping volatile organic compounds on surface-enhanced Raman spectroscopy substrates. The fabricated sensor can distinguish even residual fragrance molecules of cleaning agents used around the experimental set-up. Additionally, we showed

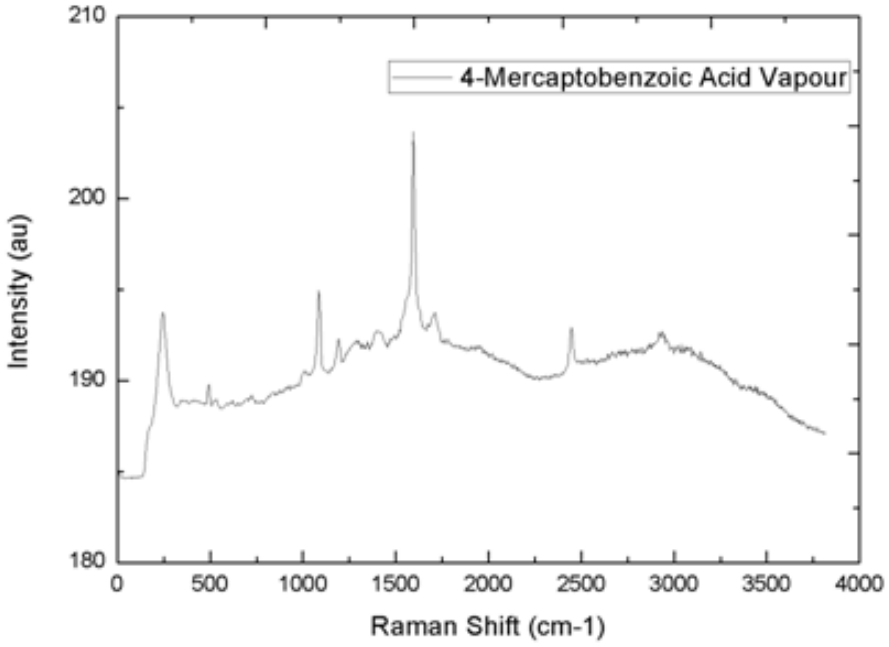

Figure 4.11: Average surface enhanced Raman spectrum of 4-MBA.

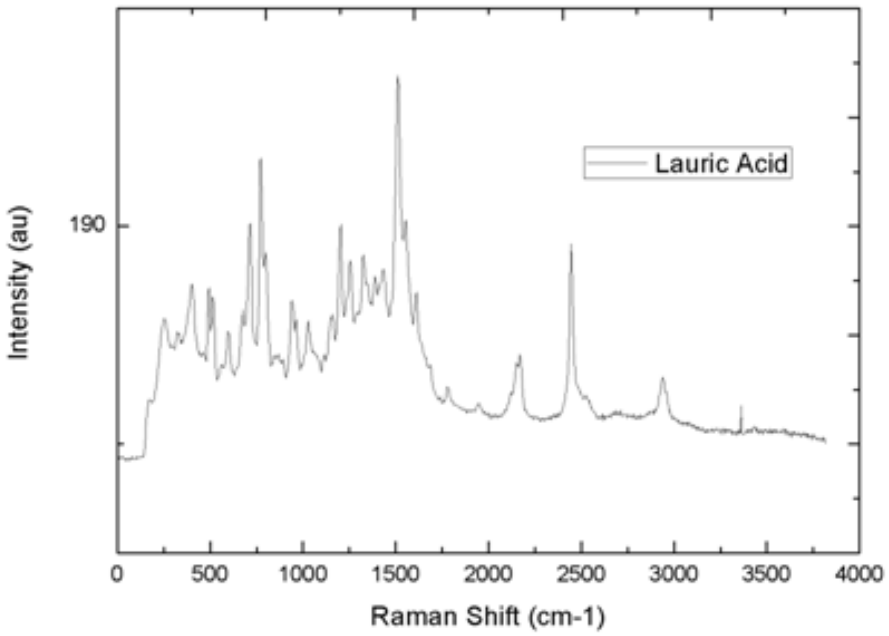

Figure 4.12: Average surface-enhanced Raman spectrum of Lauric acid.

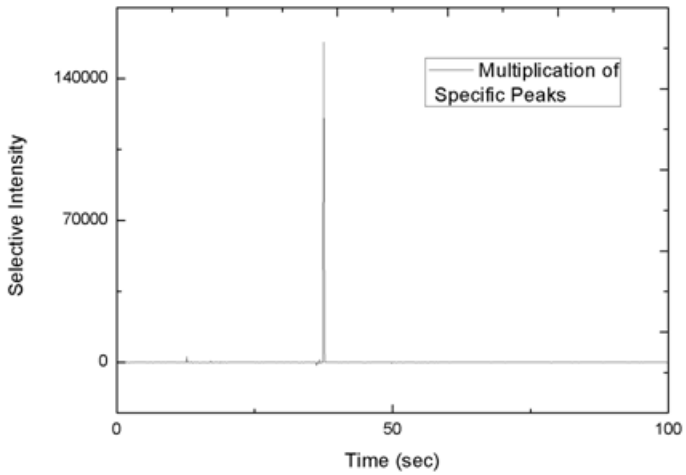

Figure 4.13: Time series of a filtered Raman spectra of a SERS substrate. A TNT sample was placed near SERS substrate. Total Raman signal wavelength filtered with TNT peak positions obtained from average surface-enhanced Raman spectrum of TNT. The peak at approximately 35^{th} sec. is assumed to be a TNT molecule diffused into the hot spot.

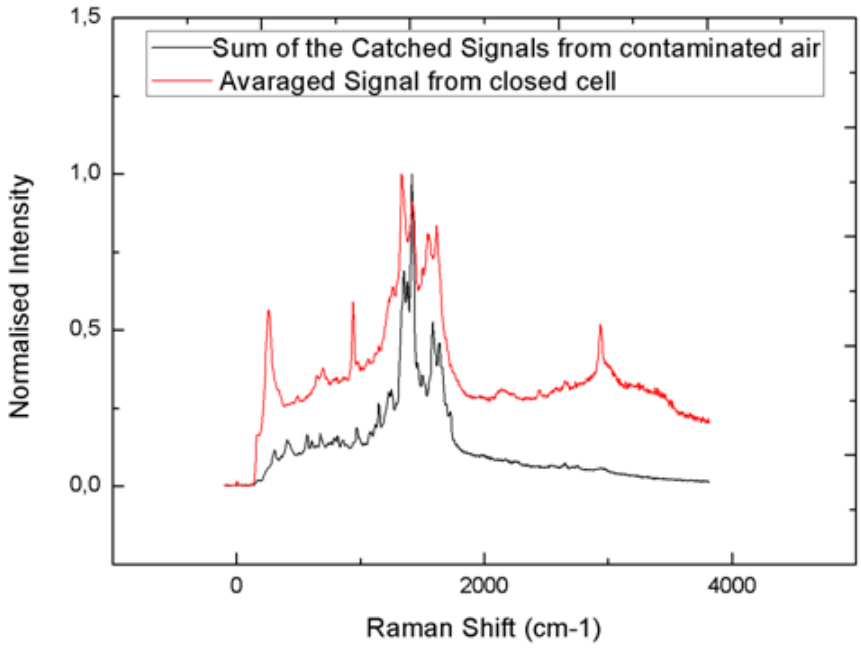

Figure 4.14: Captured Raman signal from blank SERS substrate vs SERS fingerprint of TNT. A TNT sample was placed near SERS substrate.

that excess amount of target molecules could not saturate the sensor contrary to mammalian olfactory system. Experiments revealed that sensor surface repels excess molecules with a light driven force. This phenomenon could be observed on sensor surface dip-coated with target molecules. We also showed that, it is possible to track target molecules by using SERS fingerprints.

4.4 Portable Raman microscope

We have design a portable Raman microscope that is specifically design for blinking phenomena (Figure.4.15 and 4.16). The device could be used for point of care and portable detection of VOCs. The device was 3D printed and assembled with the required optical elements (Figure 4.17). The device is using smart-phones to read-out Raman Signal. A built-in grating was placed between the image plane and imaging lens. When blinking occurs, light disperses into a line that could be read out as fluorescence and Raman spectrum. A constant current driven 532 nm DPSS (Diode-Pumped-Solid-State) laser used as an excitation source. An excitation filter was used to eliminate pump diode emission. A dichroic mirror, an aspherical lens and an emission filter were used in the optical path.

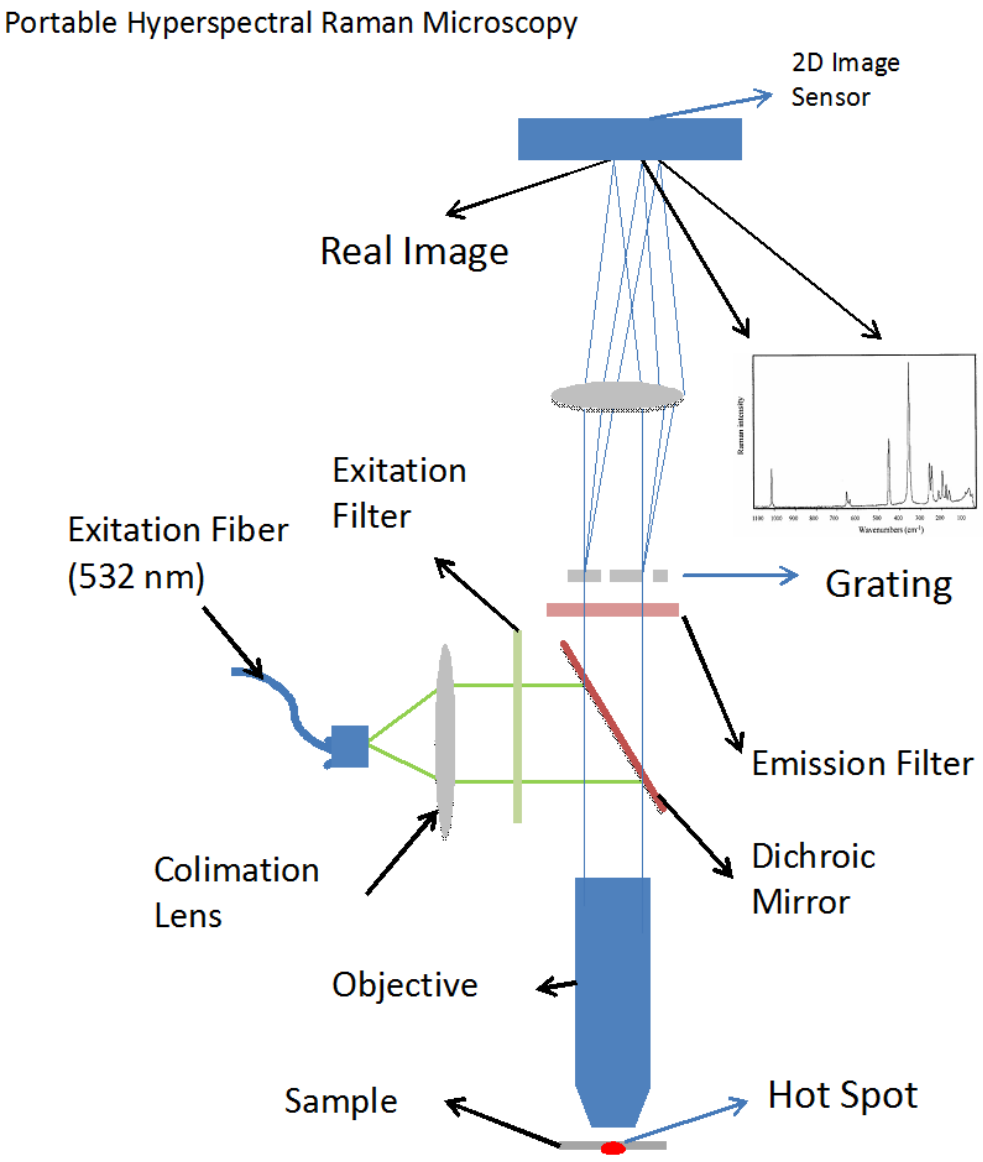

Figure 4.15: Optical design of the portable Raman system.

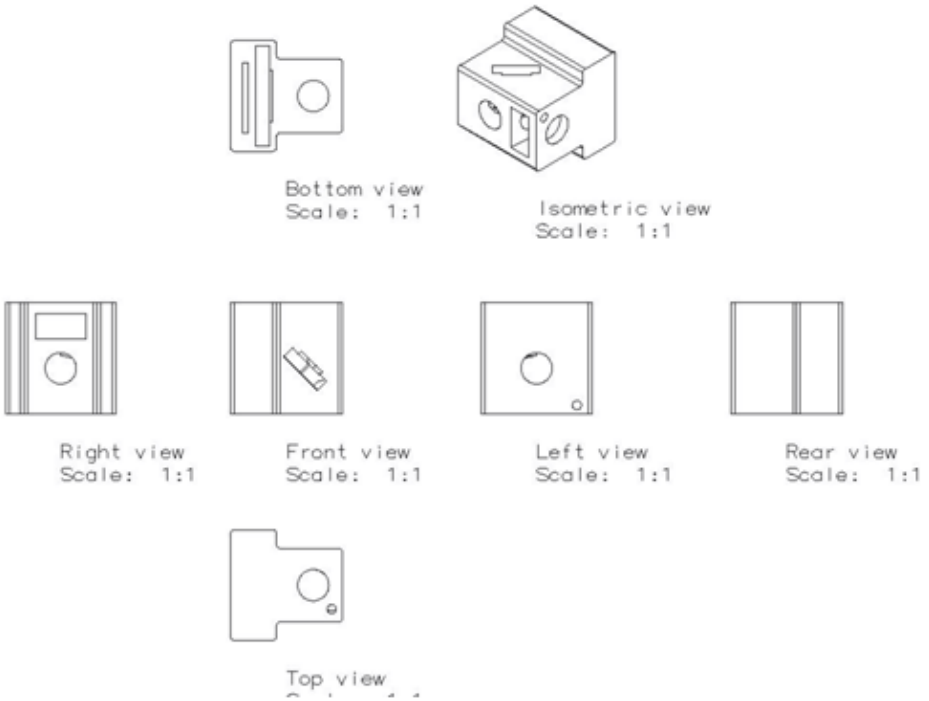

Figure 4.16: Technical drawing of portable Raman System.

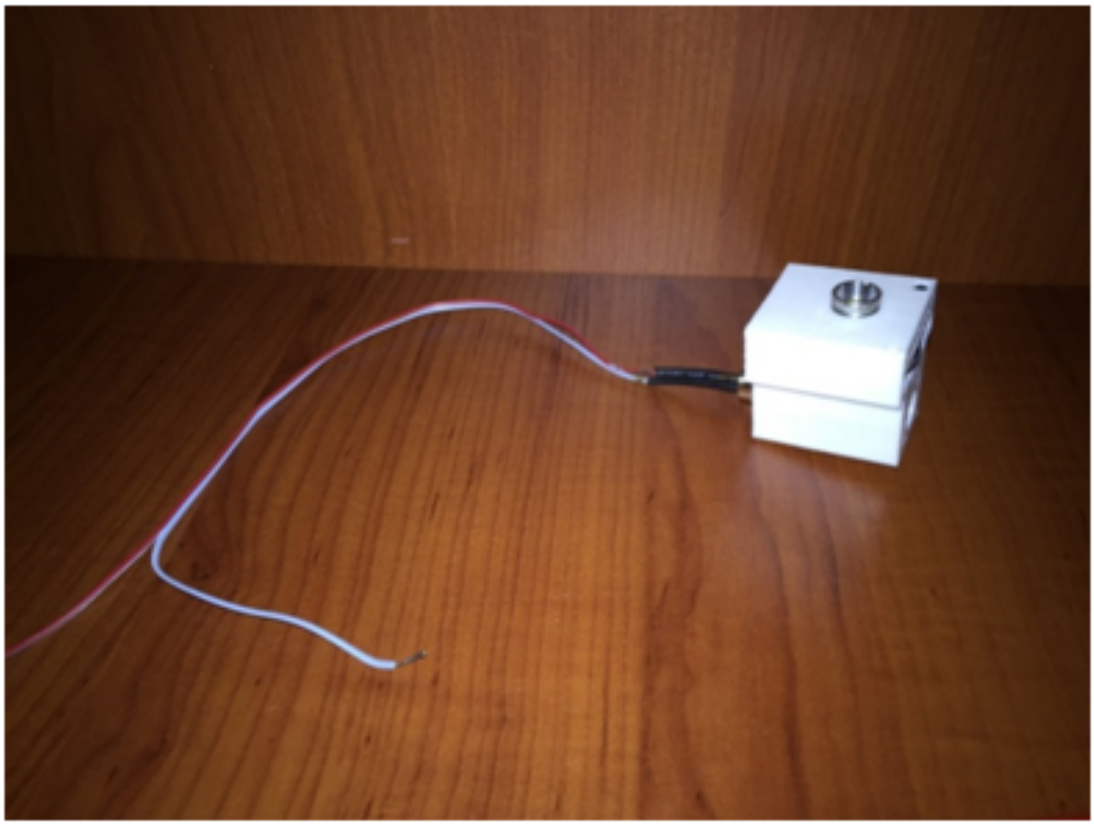

Figure 4.17: Photo of Portable Hyperspectral Raman System.

Chapter 5

Food Pathogen Detection with Surface Plasmon Resonance

5.1 Introcution

Food safety is a public health challenge and there is a great interest on using devices allowing early, fast and label-free detection of bacteria to prevent outbreaks [58]. Precise and rapid quantification of low levels of food pathogens is necessary to guarantee microbial safety of the produce and to carry out research on the subject of persistence of the pathogens [59, 60]. Traditional techniques used to identify pathogens involve the time-consuming cultivation period [61]. Cultivated pathogens are identified by biochemical testing or more advanced molecular methods like PCR, which can amplify pathogen-specific nucleic acid targets [60]. These approaches are effective, but they target only a single pathogen per assay. The development of a multiplex detection method for simultaneous identification of several food pathogens is needed to improve the efficiency of detection [62, 63, 64, 65] Therefore, there is a current need for portable, real-time, multiplex pathogen detection technologies that can predict the safety of food.
Surface Plasmon Resonance (SPR) imaging is a sensitive, label-free method that

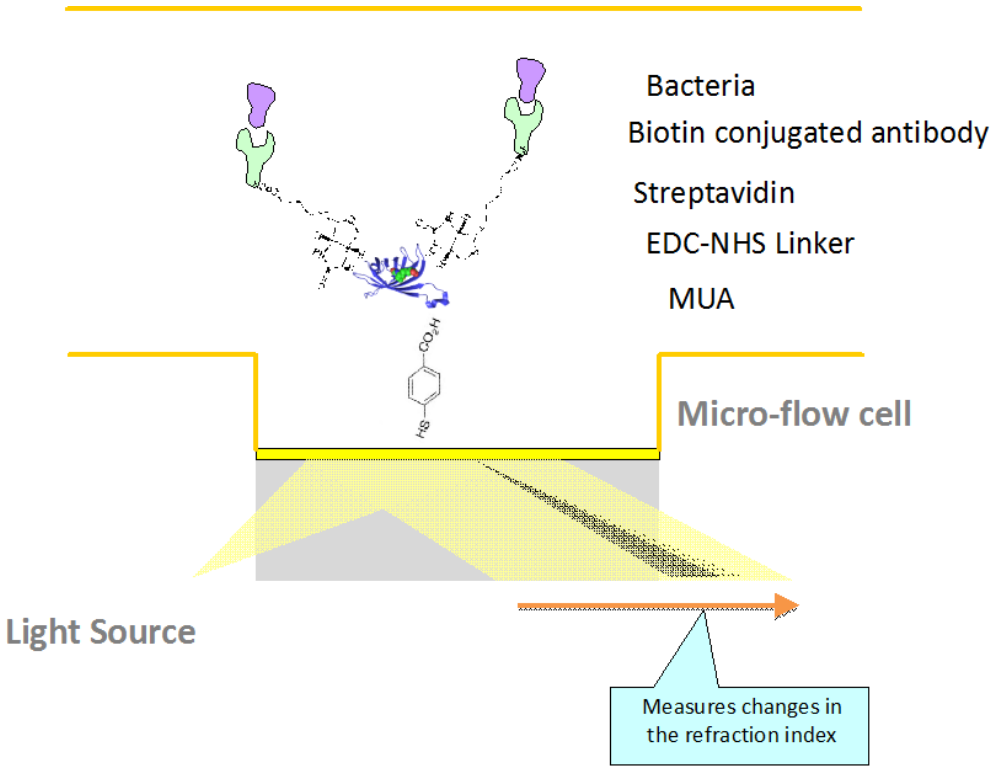

Figure 5.1: Shematic presentation of food pathogen detection with surface plasmon resonance.

can detect the binding of an analyte to a gold surface by the changes in refractive index that occur upon binding. SPR is an optical detection technique based on changes of the reflection and refraction of light and monitors the interactions occurring between biomolecules grafted on a biochip and target molecules within the sample (Figure 5.1) [66, 67, 68]

5.2 Theory

On a semi-infinite planar metal-dielectric interface, the surface plasmon polariton (SPP) wave vector is given cite as the equation below:

$$\beta = \frac{\omega}{c}\sqrt{\frac{\varepsilon_d \varepsilon_m}{\varepsilon_d + \varepsilon_m}} = k\sqrt{\frac{\varepsilon_d \varepsilon_m}{\varepsilon_d + \varepsilon_m}}$$

Where c is the speed of light in vacuum, k=$2\pi/\lambda$ free space wavenumber. And λ is the free-space wavelength. ϵ_d and ϵ_m are permittivity of dielectric and metal. The most common technique to excite surface plasmons is by using a prism coupler which is a attenuated total internal reflection method (ATR). There are two main configurations, Kretschmann and Otto geometry. In Kretschmann geometry, a high refraction index prism is coated with a thin metal semi-infinite film. When light enters the prism and reflected from the metal coated surface by total internal reflection, one part of the light propagates into the metal and forms an inhomogeneous electromagnetic wave. The wave decays in exponentially perpendicular to the metal-dielectric interface. This electromagnetic wave is referred as evanescent wave. In the case of the thickness of the metal film is smaller than 100 nm, the evanescent waves penetrates through metal film and couples the surface plasmons on the outside of the film . However, the presence of the prism effects the propagation constant of surface plasmons which can be formulated as:

$$\beta^{SP} = \beta^{SPo} + \Delta\beta = \frac{\omega}{c}\sqrt{\frac{\varepsilon_d \varepsilon_m}{\varepsilon_d + \varepsilon_m}} + \Delta\beta$$

Where β^{SPo} is the propagation constant of surface plasmons in metal-dielectric waveguide without the prism. $\triangle\beta$ is the effect of finite thickness of the metal film and the dielectric prism. For the coupling condition, the propagation constant of the evanescent wave β^{EW} should be equal to the constant of surface plasmons β^{SP}. The fomule above could be written as:

$$n_p \sin\theta = n_{ef}^{EW} = n_{ef}^{SP} = Re\left\{\sqrt{\frac{\varepsilon_d \varepsilon_m}{\varepsilon_d + \varepsilon_m}}\right\} + \Delta n_{ef}^{SP}$$

Where n_{ef}^{EW} is the effective index of the evanescent wave and n_{ef}^{SP} is the effective index of surface plasmon. Kretschmann configuration was used in this work to build an SPR device due to simple and useful design.

5.3 Experimental

5.3.1 Microorganisms

Salmonella Enteritidis and *Listeria monocytogenes* were obtained from KWIK STIK. Cultures for the assays were grown on Tryptic Soy Broth (TSB-Merck) for 24 h at 37 °C. One loop of sample from overnight culture was transferred to sterile TSB media, was grown to logarithmic phase. This culture was diluted to the level of 110^7 cfu/ml measuring of the turbidity with a spectrophotometer. The culture medium was centrifuged (4000 g 15 min.) and collected. The pellet was washed with phosphate buffer saline (PBS) to remove all remaining TSB and centrifuged at same conditions. After the second centrifugation the microorganisms were re-suspended with solution of PBS with 0.05 % Tween 80 and stored at 4°C until use.

5.3.2 Reagents

MUA (11 mercapto-1-undecanoic acid), EDC (1-Ethyl-3-[3-dimethylaminopropyl] carbodiimide hydrochloride), NHS (N-hydroxysuccinimide), streptavidin and phosphate buffer saline (PBS) were purchased from SIGMA ALDRICH. Biotin conjugated goat anti- Salmonella and L. monocytogenes polyclonal antibodies were obtained from KPL.

5.3.3 Preperation of Gold Surfaces

The production of Au coated SPR chips were performed by evaporation. Thin layer of Titanium was evaporated onto glass slides as an interfacial bonding layer. A 47 nm of 99.995 percent pure gold layer was evaporated onto titanium layer with a rotating sample holder. MUA monolayer coating on gold surfaces was prepared by immersing gold substrates into 10 mM MUA solution in absolute ethanol overnight.

5.3.4 Immobilization of antibodies

Primarily, the chip surface was washed with deionized water flow 15 minutes. A base line was obtained by injecting PBS onto the clean gold surface. Two mL of 1:1 EDC (100mM) +NHS (50mM) solution and Streptavidin (20 μg) were injected sequentially to the flow cell and their adsorption were monitored until surface saturation was observed. Excess and weakly adsorbed streptavidin was washed off by injecting PBS for 30 minutes. Then, biotin conjugated antibodies were injected to the sensor chip. PBS was used to remove excess antibodies. Reversibly bound antibodies were cleaned from the surface by injecting PBS 0.05 percent Tween 80 solution.

5.3.5 Detection of bacteria

The 1 mL of solutions containing bacteria at different concentrations were injected in to the flow cell. The unbound antigens were pre-washed by passing PBS through the flow cell. Binding of bacteria cells to the sensor surface was marked by the corresponding resonance angle changes. After each analysis the sensor was regenerated by injecting PBS 0.05 % Tween 80. The sensitivity of the developed sensor for *Salmonella* detection was determined by following the same assay procedure for *L. monocytogenes*. The resonance angle changes obtained for each bacterium were compared. In order to measure the performance of the produced

	E.coli	*L.monocytogenes*	*Salmonella*
Main colony	$32*10^7$	$55*10^7$	$80*10^7$
1.Dilution	$3.2*10^7$	$5.5*10^7$	$8*10^7$
2.Dilution	$3.2*10^6$	$5.5*10^6$	$8*10^6$
3.Dilution	$3.2*10^5$	$5.5*10^5$	$8*10^5$
4.Dilution	$3.2*10^4$	$5.5*10^4$	$8*10^4$
5.Dilution	$3.2*10^3$	$5.5*10^3$	$8*10^3$
6.Dilution	$3.2*10^2$	$5.5*10^2$	$8*10^2$
7.Dilution	$3.2*10^1$	$5.5*10^1$	$8*10^1$
8.Dilution	3.2	5.5	8

Table 5.1: Starting bacterial dilutions

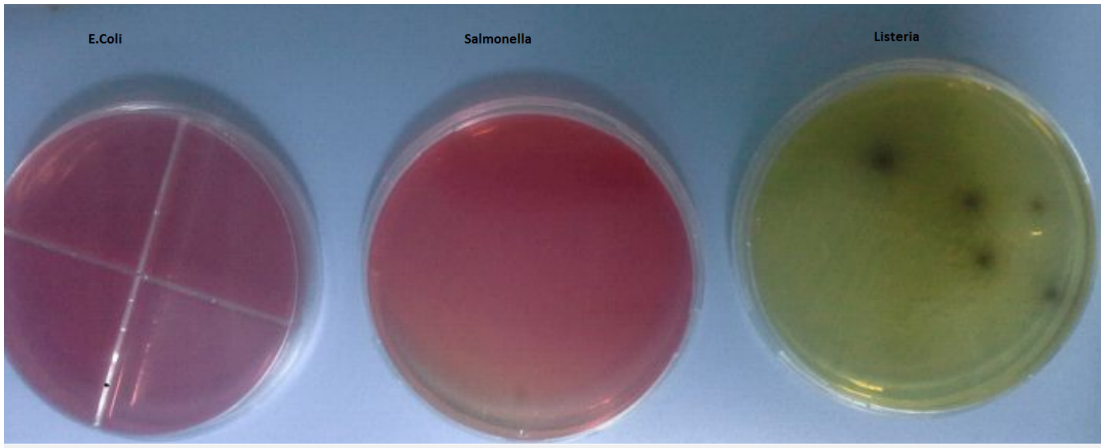

Figure 5.2: Photo of incubated pathogens.

sensor chip, pasteurized whole milk is contaminated with different concentrations of food pathogens and injected on to functionalized gold surface. The bacterial concentrations used in experiments are shown in the table 5.1 for *E.Coli*, *Listeria monocytogenes* and *Salmonella Enteritidis*.

5.4 Device construction

We have developed a surface plasmon resonance device that is designed for food pathogen detection. The device has a novel optical structure with precision temperature control. Additionally, we combined an incubation apparatus with SPR device to detect real time bacterial growth. The device can also be used for the continuous detection of bacterial secretion products. Temperature sensitive analysis allows us to work with different kind of bacterial cultures. We have also developed SPR chips to detect and culture bacterias.
Device Structure: Our device basically consists of a Light source, polarizer, detector and temperature control unit.
Light source: Maximum sensitivity of spr depends on wavelength and angular resolution of the light source. Sharp resonance peak increases sensitivity. In the Figure 5.3, calculated angle vs reflected light intensity of thin gold layer in water is shown for different wavelengths.

FWHM of resonance and resonance angle decreases with increased wavelength. Therefore, we have chosen 850nm as design wavelength. For high angular resolution we have used optical fiber with 50 um in diameter to couple the light source. Decreasing fiber diameter increases angular resolution however causes interference and light efficiency problems. Laser sources cause too much speckle and interference in the image; therefore we have searched for fiber coupled LED sources. The most important problem in using an optical fiber is to find a low cost, efficient and small fiber coupled light source. Over many trials and custom light sources, we have finally found an effective light source for portable devices. The standard telecommunication fiber optic transmitters have high optical efficiency with good coupling and repeatability. The transmitters have SMA (SubMiniature version A) connectors which is suitable for high precision optics. We have built a constant current drive circuit consist of a temperature insensitive resistor, a two channel single supply op-amp and a power mosfet.
Polarizer: The polarizer must be in NIR, therefore to build a cost effective device, we have found a linear sheet polarizer with higher dimensions. We cut the

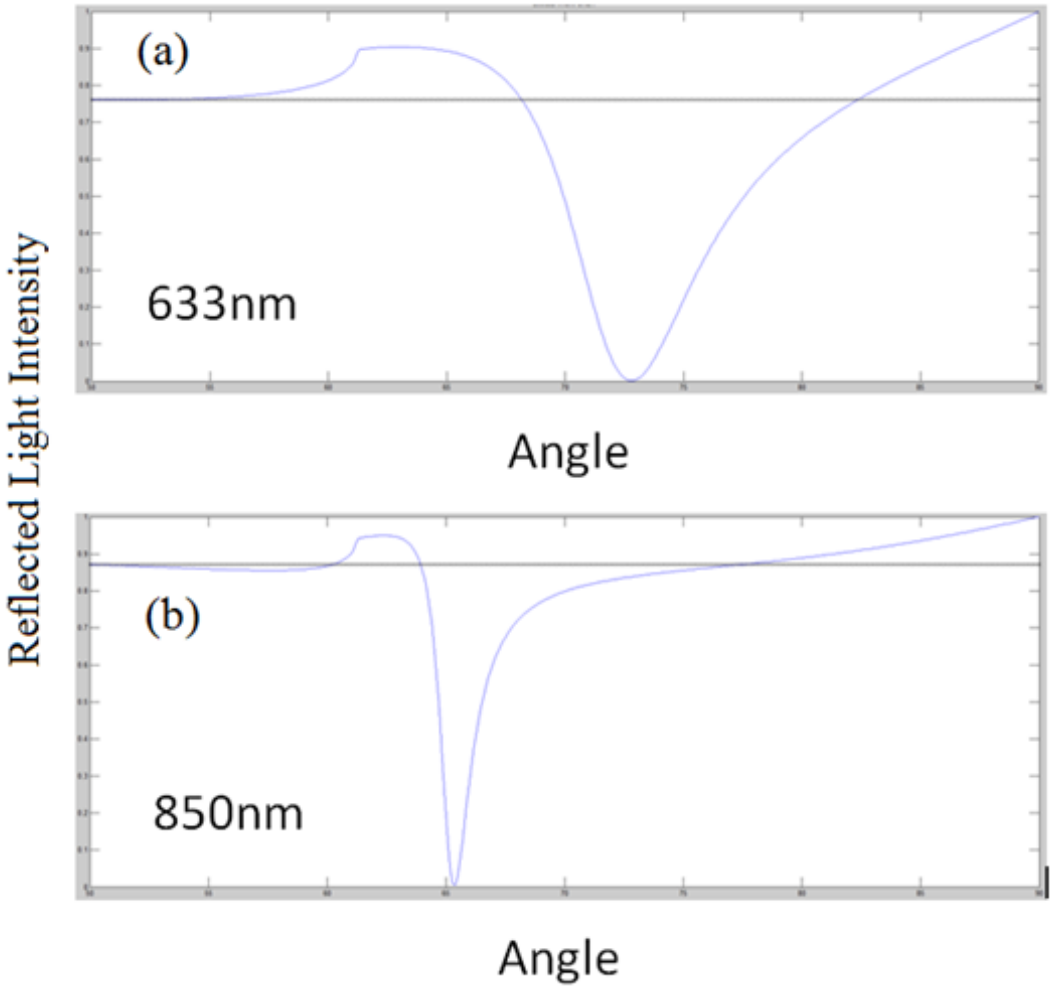

Figure 5.3: Calculated reflected intensity vs of 47nm Au film at (a) 633nm and (b) 850nm wavelength.

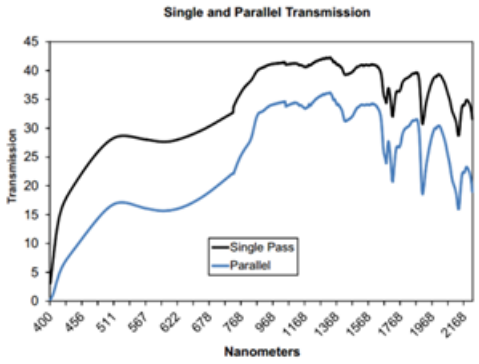

Figure 5.4: Wavelength vs. transmission graph of the polarizer.

polarizer into 1*1cm pieces to increase performance/cost. The polarizers optical transmission spectrum is below.

Image sensor: Using a 2D sensor to detect angular spectra in SPR is a novel technique. We are using an OEM CMOS 1.3MP sensor in our devices. Using a 2D sensor make it possible to multi-channel measurement. Integration of multiple lateral pixels reduced noises effectively. The device has 8 bit ADC with 30 fps which allowed us to integrate multiple readouts in a second.
Temperature control unit: Here we developed a temperature control unit with custom made PID (Proportional-Integral-Derivative) control. Using a PWM on a resistor has some disadvantages.Applying high power PWM (Pulse-Width Modulation) causes oscillations on circuit and emits EMI (Electromagnetic interference) to other electronic elements. We are using a power Mosfet (Metal Oxide Semiconductor Field Effect Transistor) as heating element because of its low heat capacity and high heat transfer constant. We have drived mosfet as a tunable resistance to produce heat to not to generate EMI. Also Mosfets can handle high power in a small area. Generated heat is effectively transferred to aluminum chassis. Temperature response of the aluminum chassis is measured with a re-calibrated analog temperature sensor. Embedded software uses a homemade written PID to stabilize temperature. We have achieved a temperature stability of 0.1 °C.

We have started to characterize the SPR device. We have noticed that spectral resolution is limited with pixel size which cause step vise increase as shown in the Figure 5.6. The origin of this effect is interference and resolution of the camera. Interference causes periodical changes in the signal. To eliminate interference, we applied Savitzky-Golay FIR smoothing filter to signal. Additionally, we applied a spline interpolation to the original signal to increase the resolution. In the Figure 5.5, the original and filtered signal is shown.

The Device has a PTFE fluid channel. The thickness of the channel is 500 um which will be reduced during the optimization steps. Sealing of the fludic chamber was achieved with a Viton o-ring.

5.5 Optimization of experimental conditions

We have first optimized the experimental conditions and characterized device parameters. We have measured the standby time that drifts in the signal are minimum. As shown in the Figure 5.7, one needs to wait for almost 30 minutes after device opening and fluid pumping. The reason is basically settlement of the surface bubbles, fluidic movement of index matching fluid and stabilization of the peristaltic pump. After 30 minutes, calculated noise in resonance angle is lower than 10^{-4} angles.

We have injected a PBS pulse into a water filled fluid channel to find the response time of the channel. As shown in the Figure 5.8, we observe step-vise increase rather than a Gaussian curve because of the high channel size. The possible reasons are electro-osmotic flow and turbulent flow inside the flow channel. Therefore, we have decreased the channel size gradually and test each dimension. Finally, we have found that 100 μm of channel size is optimum for laminar flow. In the Figure 5.8, we measured resonance angle change with PBS pulse in high

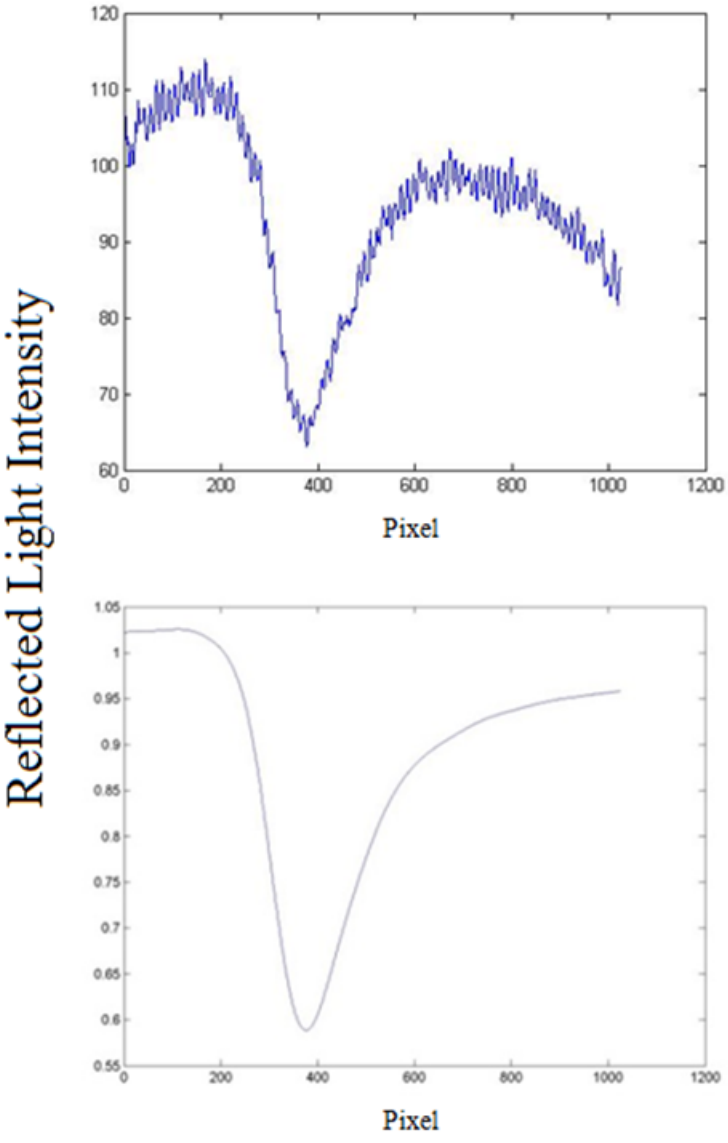

Figure 5.5: (a) Original and (b) filtered pixel vs reflected light intensity in SPR.

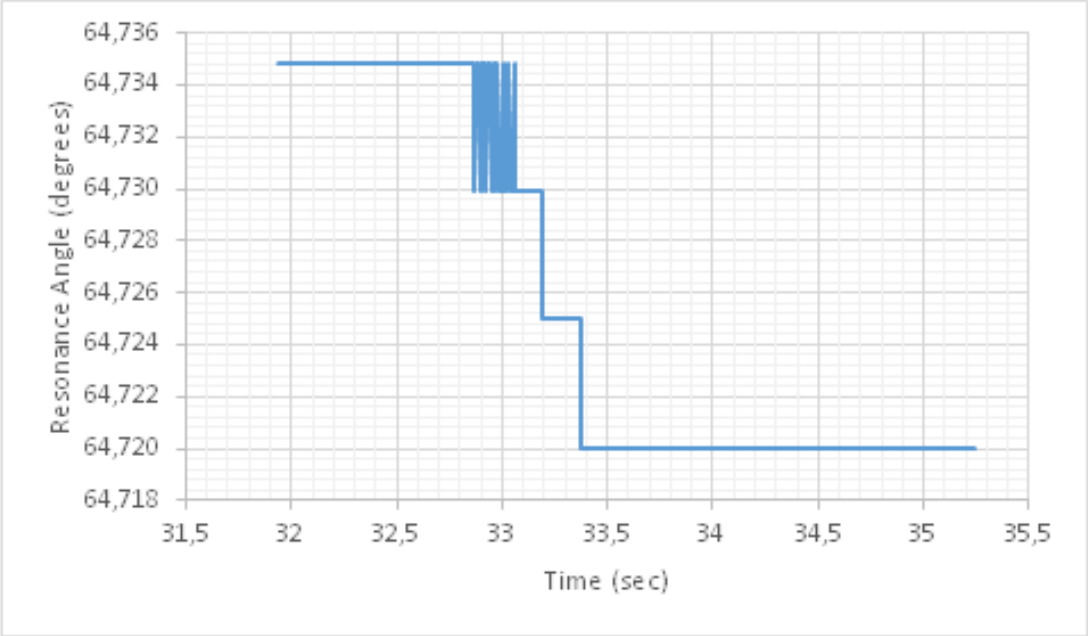

Figure 5.6: Change in the resonance angle vs time. Saw-like decrease is shown before correction in the software.

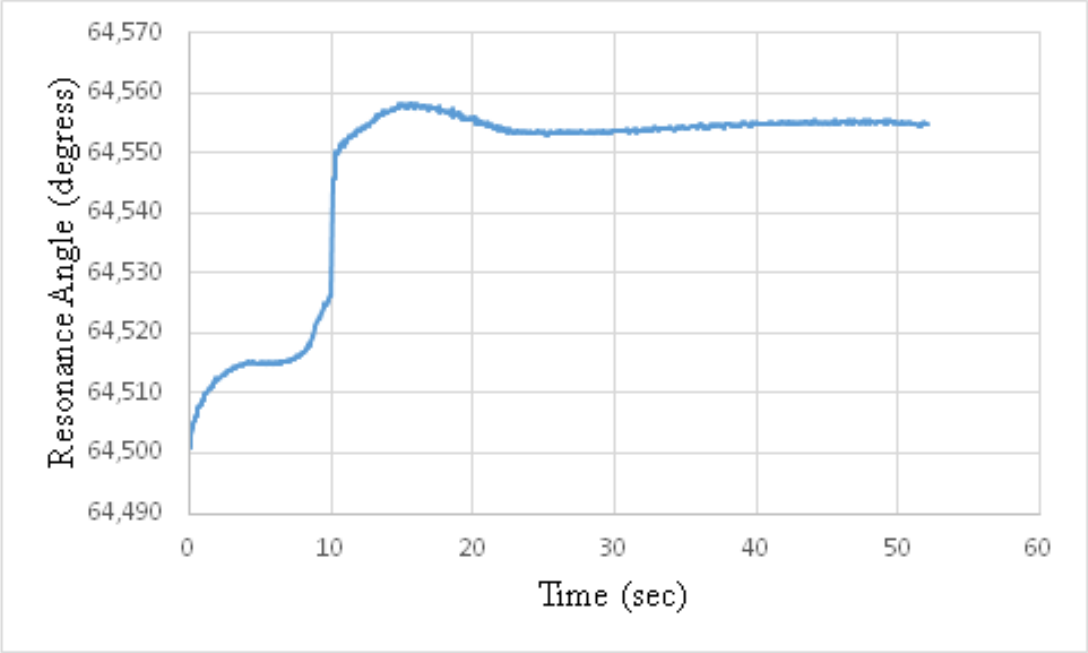

Figure 5.7: Resonance angle vs time after device opening.

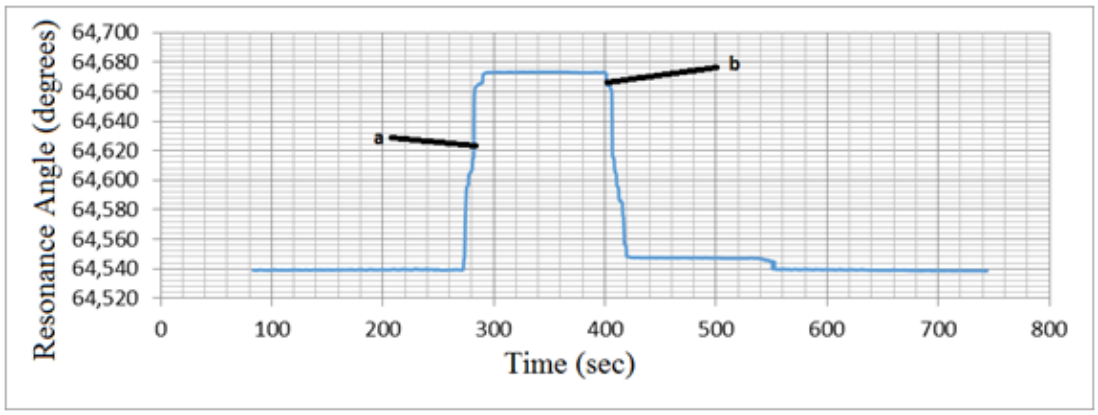

Figure 5.8: Resonance angle change during a PBS pulse send in water filled flow channel with 500 um height.

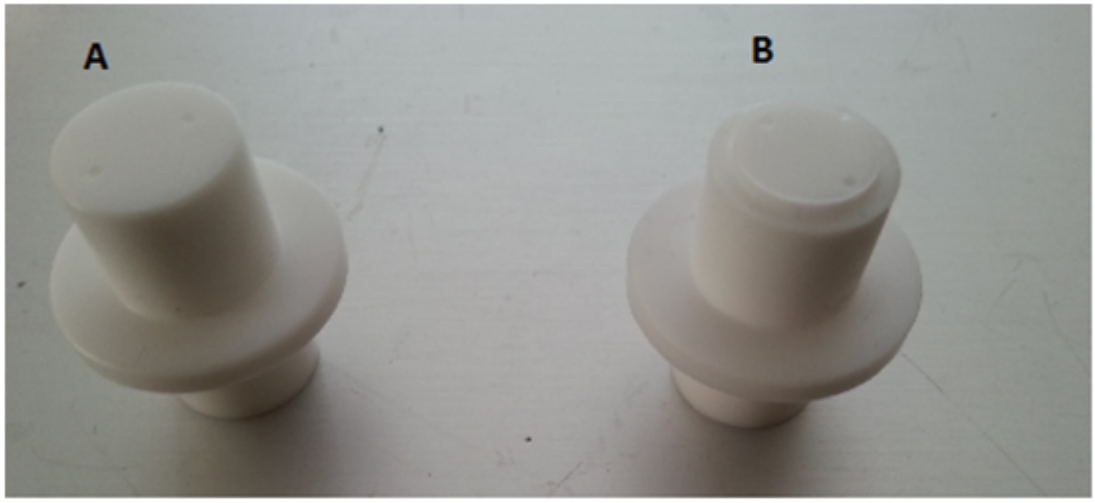

Figure 5.9: (a) 500 um and (b) 100 um PTFE flow channel of the SPR

volume flow channel. After dimensional correction in channel size, we have observed a Gaussian like increase in resonance angle as could be seen in the Figure 5.10. We are using a CNC machined PTFE flow channel with an o-ring. Increasing the size of the PTFE decreases channel size. In the Figure 5.9, we showed the original and the modified PTFE part used for flow.

We have used Tween 80 solution to increase the solubility of pathogens in PBS. A problem was observed after Tween addition because of its surfactant character.

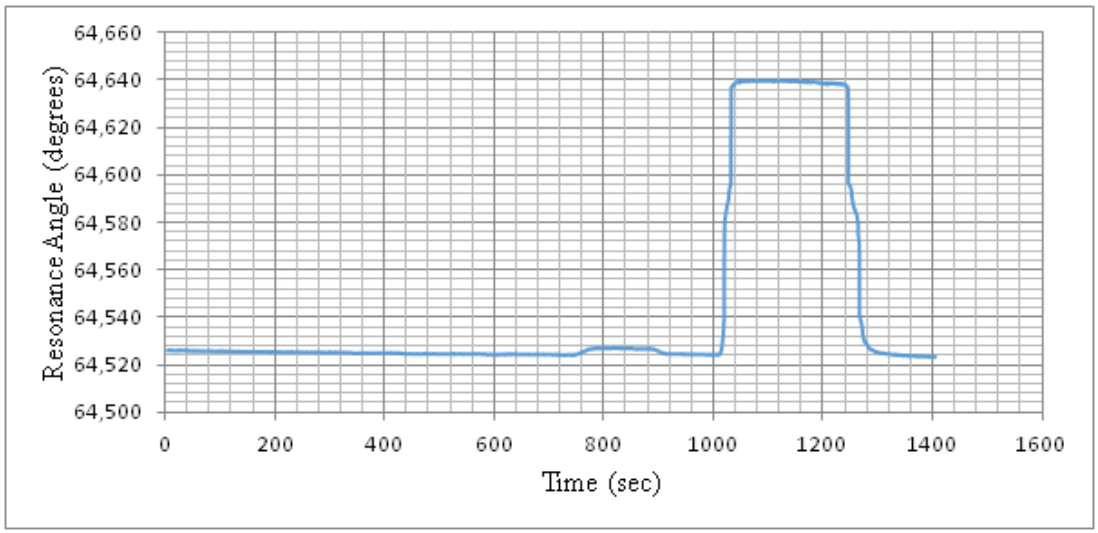

Figure 5.10: Resonance angle change during a PBS pulse send in water filled flow channel with 100 um height.

Tween causes a change in the viscosity and makes PBS hard to remove from corners of the chamber. This causes local concentration deviations and accumulation of previous concentrations. We have eliminated o-ring to minimize corners and avoid sharp concentration changes. In the Figure 5.11, the final design of PTFE chamber is shown. In the Figure 5.12, we have taken photo of the used SPR chip after experiment. PBS solution is accumulated in the center of the fluidic chamber after o-ring elimination.

Flow speed is one of the most important variable that affects sensitivity of SPR device. Pressure inside the flow cell changes with flow speed. Pressure fluctuations causes mechanical distortions and refraction index changes. Therefore, flow speed has a direct effect on resonance angle. In the Figure 5.13, we have measured resonance angle with increasing flow rate.

Figure 5.11: Modified PTFE channel is shown. In this channel design, the interaction of fluid with o-ring is prohibited.

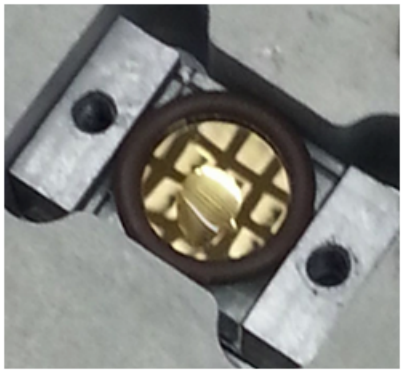

Figure 5.12: Photo of the sample holder of the device after an experiment. The fluid channel is filled with water during the removal of the PTFE channel.

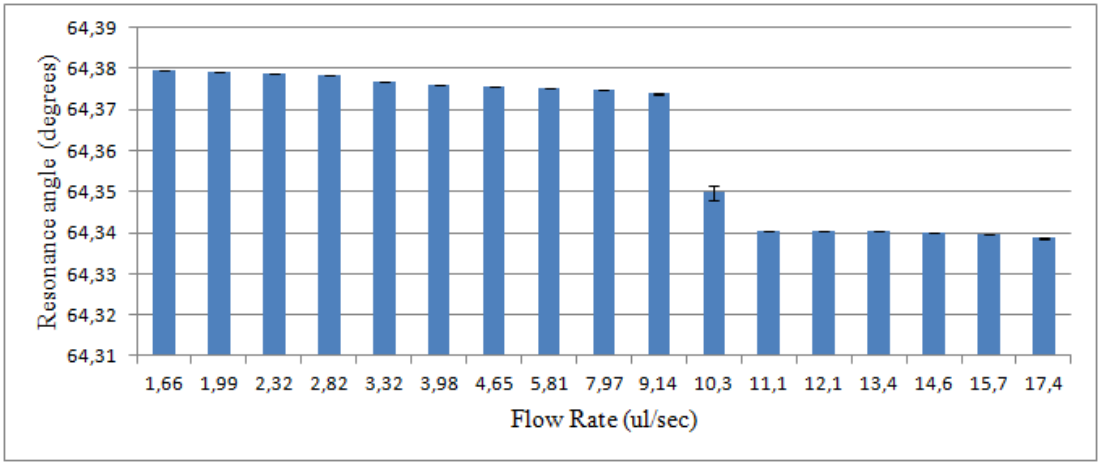

Figure 5.13: Average resonance angle with respect to flow speed.

Flow rate (ul/sec)	**1,66**	**1,99**	**2,32**	**2,82**
Average	64,37935918	64,37920677	64,37885752	64,37823
Standard deviation	0,000108517	0,000115605	0,000213494	0,00045
Standard error	4,31657E-06	5,38428E-06	7,19689E-06	1,68E-05
Flow rate (ul/sec)	**3,32**	**3,98**	**4,65**	**5,81**
Average	64,37674184	64,37602428	64,37567115	64,37517
Standard deviation	0,000575093	0,000177471	0,000171984	0,000195
Standard error	2,38794E-05	6,79572E-06	6,02065E-06	5,73E-06
Flow rate (ul/sec)	**7,97**	**9,14**	**10,3**	**11,1**
Average	64,37461017	64,37393045	64,34970121	64,34059
Standard deviation	0,000176608	0,001791187	0,014661984	8,2E-05
Standard error	5,68226E-06	5,52247E-05	0,00059316	4,13E-06
Flow rate (ul/sec)	**12,1**	**13,4**	**14,6**	**15,7**
Average	64,34040745	64,34028447	64,34000006	64,33951
Standard deviation	8,20279E-05	0,000129513	0,000122518	0,000202
Standard error	3,48818E-06	5,90528E-06	5,70004E-06	8,99E-06
Flow rate (ul/sec)	**17,4**			
Average	64,33865507			
Standard deviation	0,000454472			
Standard error	2,08966E-05			

Table 5.2: Calculated statistical values of resonance angle with different flow speeds

	strep 2.5μg	strep 7.5μg	12.5μg
Resonance angle shift	0.0025°	0.0038°	0.0050°

Table 5.3: Average change in the resonance angle with the amount of streptavidin.

5.6 Surface functionalization

The aim of the work is to label free and fast detection of food-bourne pathogens. We have used anti-salmonella, anti-listeria and anti-E-coli antibodies to start with. After instrumental optimization, device is ready for the surface functionalization experiments.

EDC-NHS reaction is used to covalently bind proteins onto COOH covered surfaces. Therefore, the first step in functionalization is activating the surface with EDC-NHS. Optimum EDC-NHS concentration is critical for protein binding. Moreover, EDC-NHS reaction forming gas during the preparation as shown in the Figure 5.14. Gas formation in the microchannel distorts resonance angle and decreases the quality of total experiment. One needs to minimize gas formation for sensitive detection. Gas causes miscalculation of the resonance angle in the orders of degrees as could be seen in the Figure 5.16. Experiments showed that 400-100 concentration is forming lower amount of gas. And as shown in the figure 5.15, EDC-NHS is active and also still binds to BSA.
Dilutions of streptavidin were pumped to the EDC-NHS functionalized surface to find the optimum amount. In Table 5.3, We have calculated the average resonance angle values vs strepravidin amount. Results show that, 17 μg of streptavidin is enough for surface coverage. We decided to add 20 μg in the following experiments to guarantee complete coverage.
The queued material to be optimized is biotinated antibody. Serial dilutions of antibody solution pumped to the streptavidin covered chip surface. In the Table 5.4, we have calculated the average values of resonance angles and change in the resonance angles with the amount of streptavidin. Experiments showed that we need to use 10 μg of antibody for complete coverage of SPR chip surface.

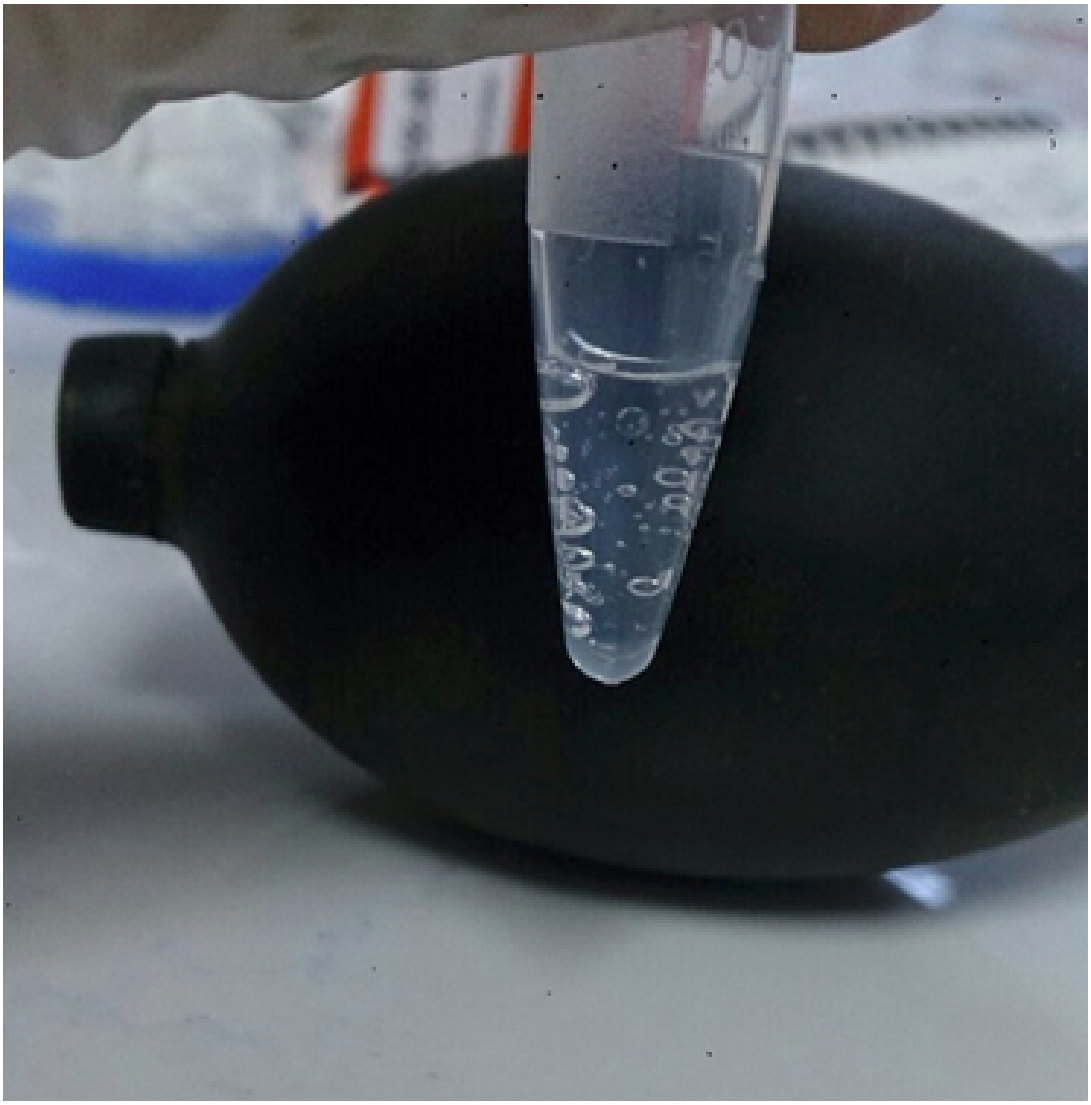

Figure 5.14: Photo of EDC-NHS reaction in an Eppendorf. Bubbles formed during the preparation of the mixture.

	strep 2μg	strep 4μg	10μg
Resonance angle shift	0.0045°	0.011°	0.19°

Table 5.4: Average change in the resonance angle with the amount of salmonella antibody.

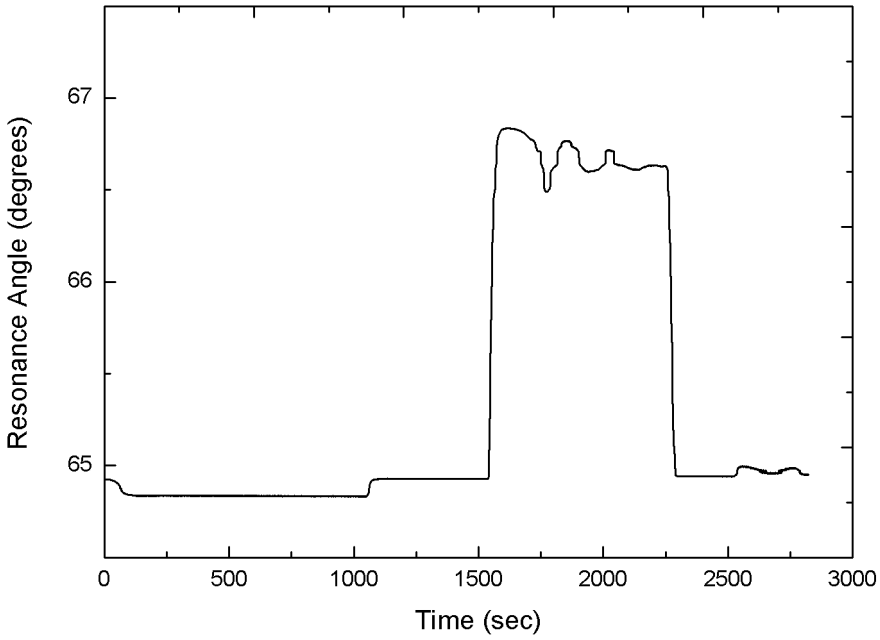

Figure 5.15: Time vs resonance angle during the 400:100 mM EDC-NHS pulse pumped into the SPR device.

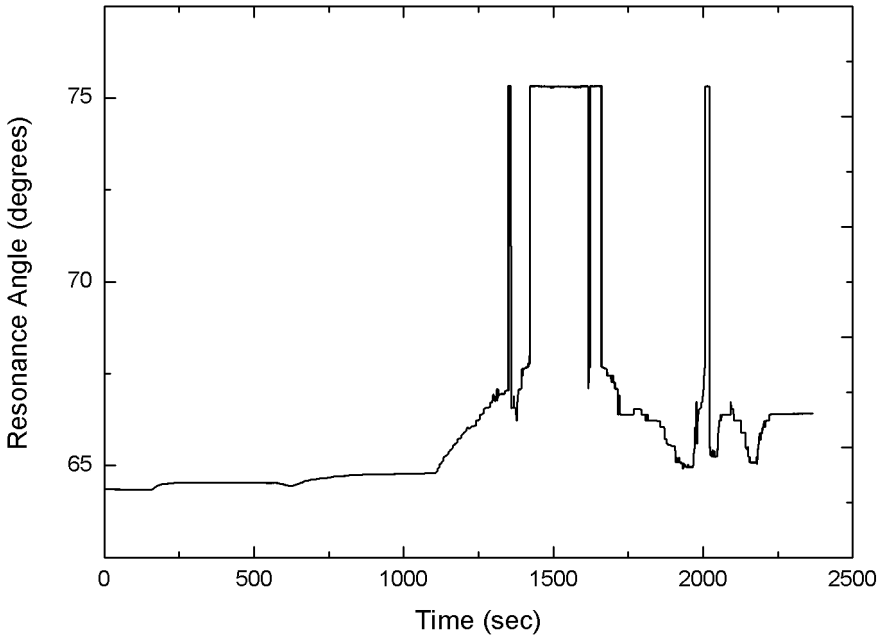

Figure 5.16: Time vs resonance angle during the 200:100 mM EDC-NHS pulse pumped into the SPR device.

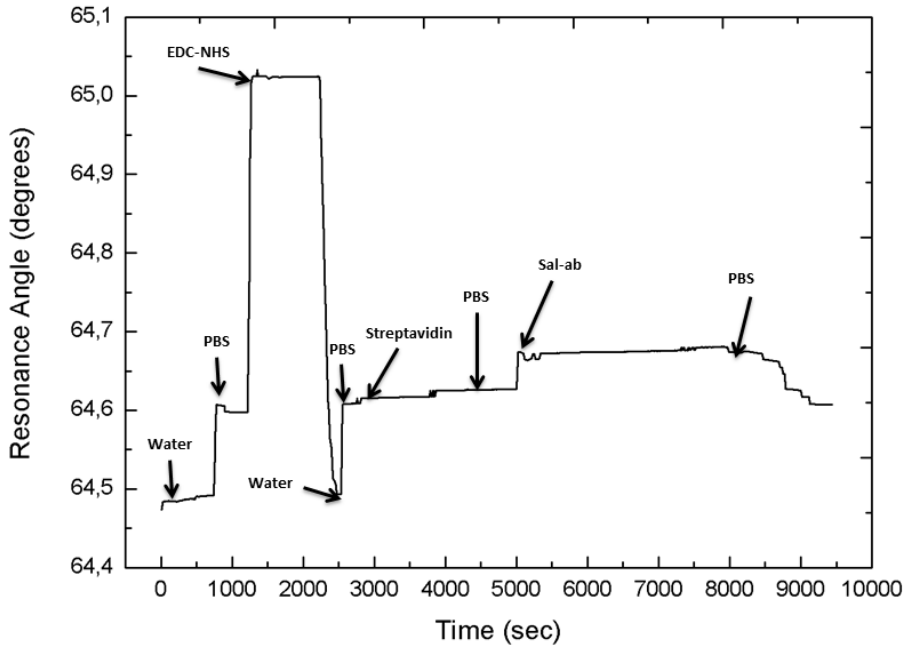

Figure 5.17: Surface functionalization of the SPR chip surface with salmonella antibody.

As shown in the Figure 5.17, Salmonella antibody is successfully bonded to the surface by using the optimized conditions.

5.7 Pathogen Detection

The changes in the resonance angle were investigated during the functionalization steps of EDC+NHS, streptavidin and biotin conjugated antibodies. Resonance angle was increased during the binding of streptavidin. The immobilization of the anti-Salmonella through avidin/biotin chemistry led to a remarkable change in resonance angle. The changes in the resonance angle induced by bacterial binding at various concentrations are shown in figure 5.18 (The red line is the

average of signal). Signal increased with increasing bacterial binding following the injection of *Salmonella* solutions to the flow cell. As shown in figure 5.19, we found that the detection limit for *Salmonella* is 110^2 cfu/mL which is one of the best results obtained with SPR compared to results given in the literature [67],. A good correlation was obtained between bacteria concentration and the change in resonance angle.
The selectivity of the SPR biosensor was tested by using dilution series of the *L. monocytogenes*. After performing *Salmonella* binding experiments, cross-contamination experiments were conducted. We have injected *L. monocytogenes* on to Salmonella antibody functionalized gold surface to investigate the sensitivity of the developed sensor by using the same assay procedure. The binding of *L. monocytogenes* to the Salmonella antibody was shown in figure 5.20. According to the results, a small amount of *L. monocytogenes* was bonded to the *S. Enteritidis* antibody coated surface. It was observed that the response induced by the non-specific binding (*L. monocytogenes*) was much lower than that of the response induced by *S.Enteritidistidis*. Additionally, resonance angle changes obtained from *L. monocytogenes* at different dilution levels were smaller than that of the detection limit of target pathogen, which shows the high specificity of the biosensor.

Chip surfaces were imaged after bacteria attachment by using SEM. According to Figure 5.21, *S. Enteritidis* are attached to the SPR chip surface in higher amount and more uniform than the *L. monocytogenes* (Figure 5.22).

The ability of developed sensor to detect *S. Enteritidis* in food samples was investigated. UHT pasteurized whole milk samples inoculated with *S. Enteritidis* to test proposed biosensor platform for commercial applications. A detectable signal increase was observed onto functionalized chip with increasing contamination level (Figure 5.23).

We have applied the same procedure for *L.monocytogenes* detection. In the figure 5.24, a complete experiment is shown. (Figure 5.25) Results showed that sensor performance is lower than *Salmonella* detection. However, the results are

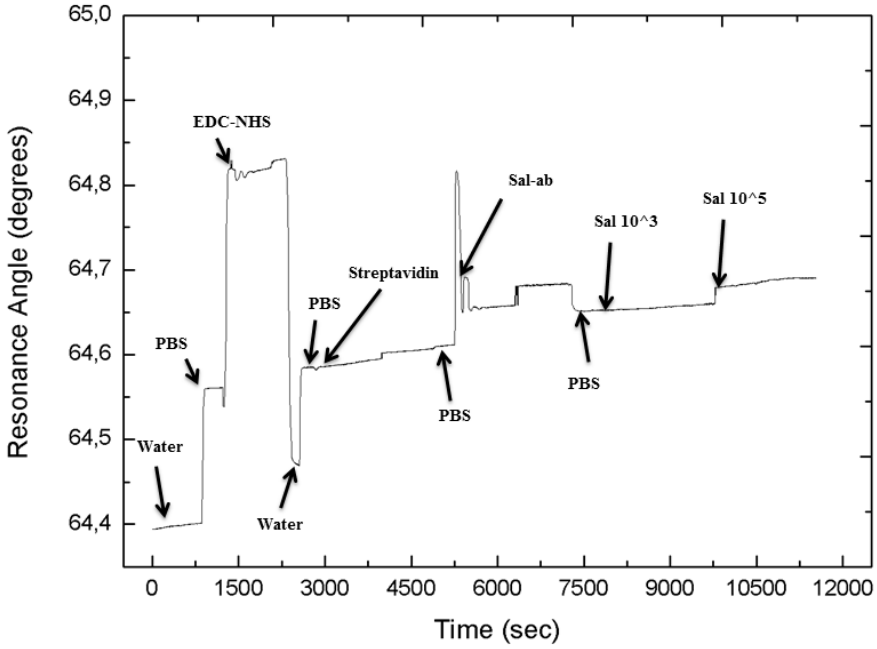

Figure 5.18: Changes in resonance angle during the functionalization of the Au surface and *S. Enteritidis* flow.

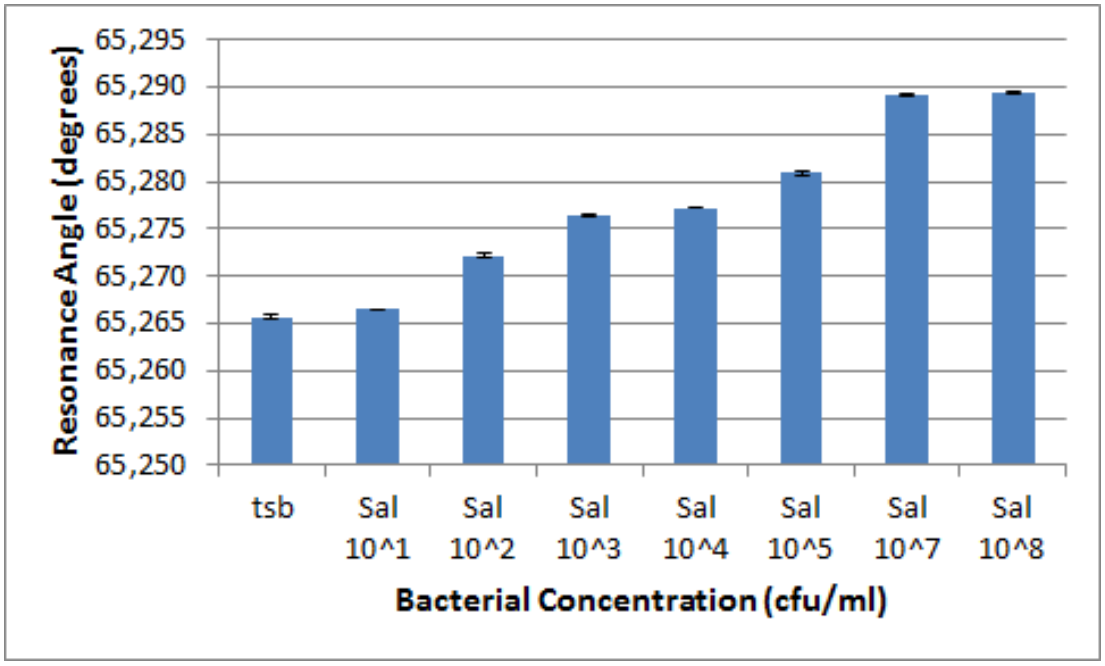

Figure 5.19: Average resonance angle with respect to *S. Enteritidis* concentration.

adequate enough compared to the techniques used in *L.monocytogenes* detection such as PCR [68]. In the table 5.5, we have showed calculated average resonance angle changes, standard errors, and standard deviation of signal during the whole experiment of *L.monocytogenes* detection. We have used *E.coli* for cross-contamination experiments to measure the selectivity of the sensor chip (Figure 5.27). Resonance angle vs time graph of *E.coli* injection on to Listeria-ab functionalized surface is shown in the figure 5.26. In the table 5.6, calculated values of *L.monocytogenes* cross-contamination experiment is shown.
Results showed that 250 *L.monocytogenes* microorganism has changed resonance angle for 9 milidegrees. 2500 Listeria microorganism made a 117 milidegree change on resonance angle. In the cross-contamination experiments, non-specific binding of 1000 *E.coli* made 11 milidegree change in the resonance angle. 106 *E.coli* made 12 milidegree change. In light of the foregoing data, the developed platform could detect 2500 *L.monocytogenes*.

After functionalization and injection of the pathogens, we have stopped the pump flow. In few hours, the resonance angle started to increase. The pathogens

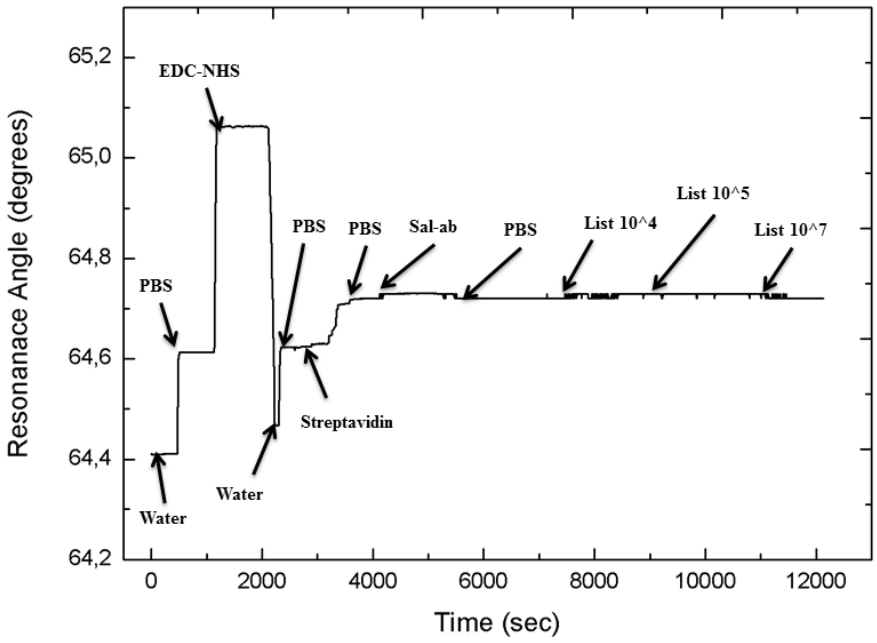

Figure 5.20: Changes in resonance angle during functionalization steps and *L. monocytogenes* flow.

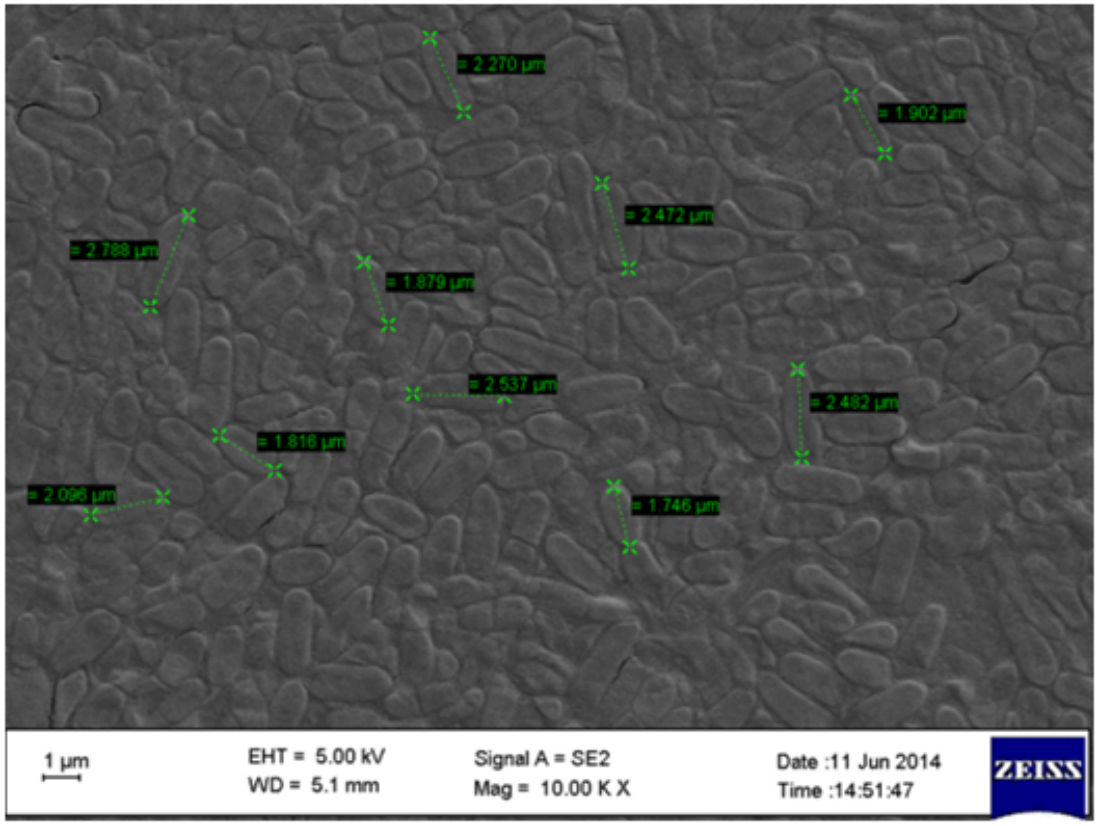

Figure 5.21: SEM images of Sal-ab functionalized SPR chip after *S. Enteritidis* flow.

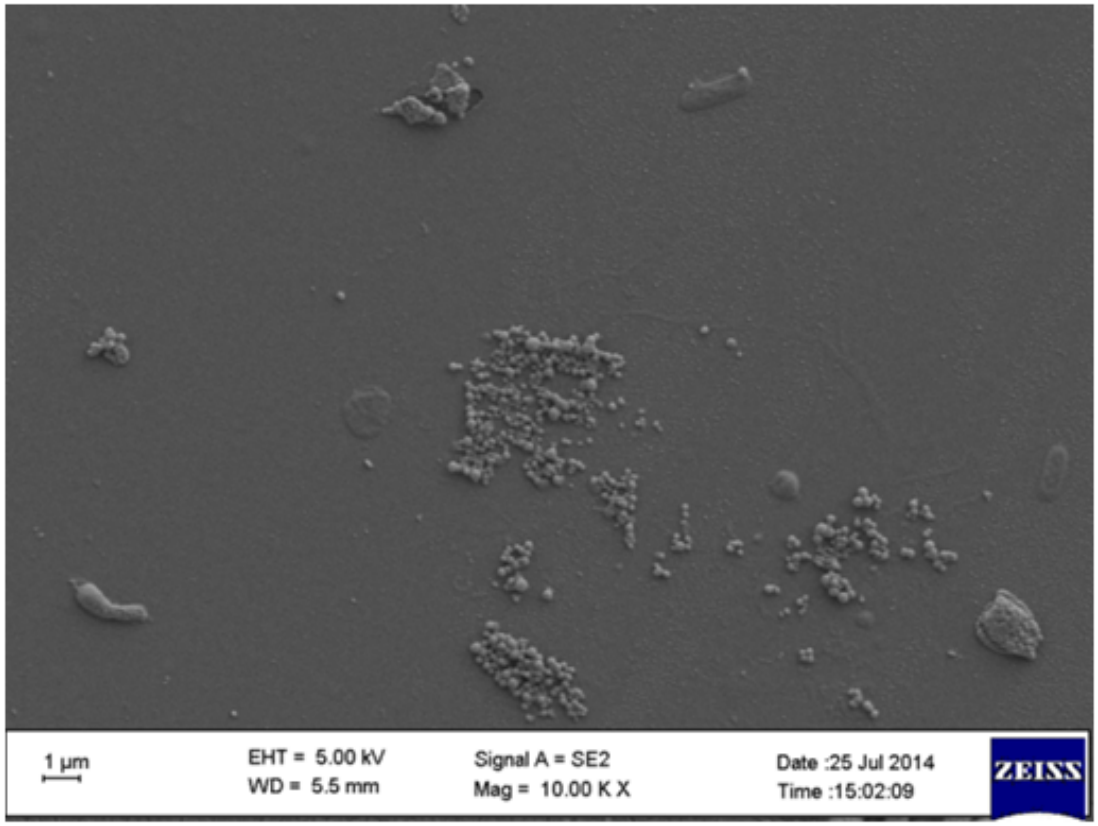

Figure 5.22: SEM images of Sal-ab functionalized SPR chip after *L. monocytogenes* flow.

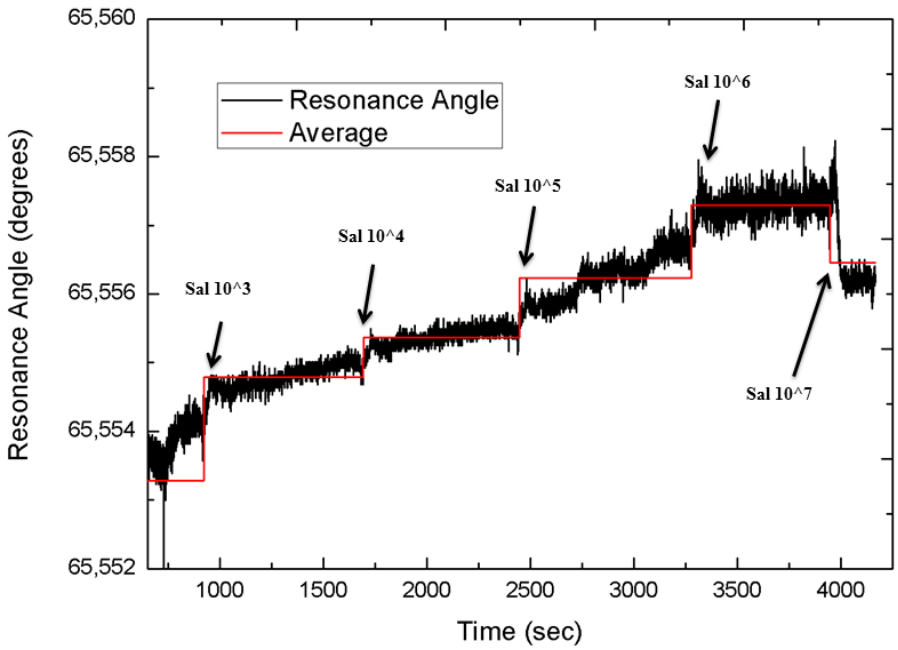

Figure 5.23: Resonance angle change vs pathogen contaminated whole milk with different concentrations. Blue line is the original signal. For better demonstration red line is calculated average resonance angle of each concentration.

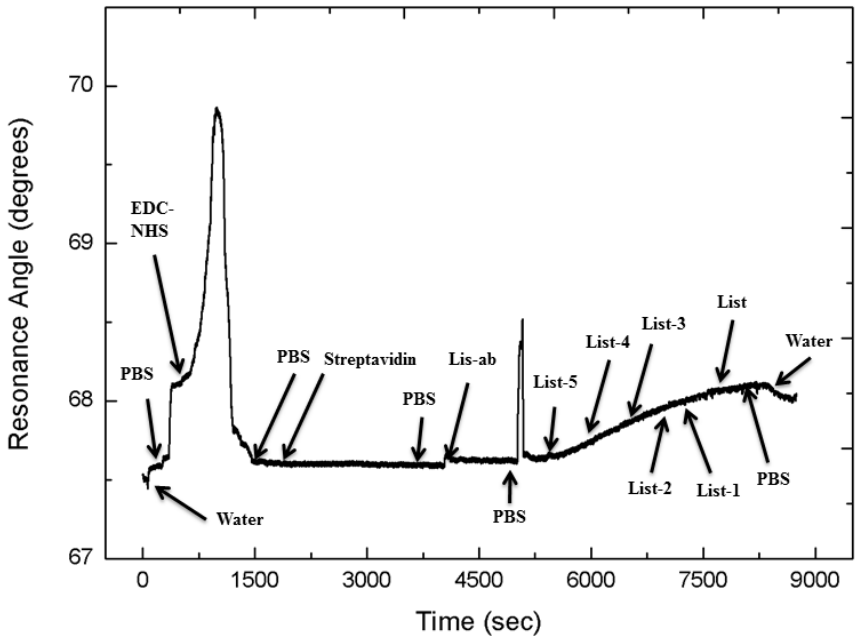

Figure 5.24: Change in the resonance angle during *L.monocytogenes* flow on Listeria-antibody functionalized SPR chip surface.

	Mean	Standard deviation	Standard error	N
water	6,75E+01	0,010771379	9,83E-04	1,20E+02
PBS	6,76E+01	0,037279529	1,84E-03	4,09E+02
mes	6,76E+01	0,008827968	8,83E-04	1,00E+02
edcnhs	6,83E+01	0,529290705	1,09E-02	2,36E+03
mes	6,86E+01	0,852491175	2,53E-02	1,14E+03
pbs	6,77E+01	0,0433105	1,50E-03	8,31E+02
streptavidin	6,76E+01	0,009678679	1,25E-04	6,02E+03
pbs	6,76E+01	0,008956636	3,65E-04	6,01E+02
listeria	6,76E+01	0,01298542	2,70E-04	2,31E+03
pbst	6,77E+01	0,232915624	6,46E-03	1,30E+03
listeria-5	6,77E+01	0,033077014	8,48E-04	1,52E+03
listeria-4	6,78E+01	0,023556567	8,16E-04	8,33E+02
listeria-3	6,79E+01	0,021250451	7,79E-04	7,44E+02
listeria-2	6,79E+01	0,019147484	6,87E-04	7,76E+02
listeria-1	6,80E+01	0,011927894	5,16E-04	5,34E+02
listeria	6,80E+01	0,012868014	5,19E-04	6,15E+02
pbst	6,81E+01	0,011945803	9,00E-04	1,76E+02
pbs	6,81E+01	0,016384146	4,45E-04	1,35E+03
water	6,81E+01	0,034928376	1,06E-03	1,08E+03

Table 5.5: Calculated statistical values of resonance angle during *L.monocytogenes* detection experiment

	Mean	Standard deviation	Standard error	N
water	6,58E+01	0,004846871	0,00012087	1608
pbs	6,60E+01	0,02832883	0,00085029	1110
mes	6,64E+01	0,911989489	0,022672561	1618
edc-nhs	6,67E+01	0,079576329	0,001824646	1902
pbs	6,62E+01	0,165046804	0,006034709	748
streptavidin	6,61E+01	0,009955154	0,000111177	8018
pbs	6,62E+01	0,004048857	0,000130001	970
L-ab	6,62E+01	0,009563892	0,000116202	6774
pbs	6,62E+01	0,005389243	0,00020254	708
pbstween	6,62E+01	0,005011722	0,000216071	538
ecoli-7	6,62E+01	0,003934343	0,000169622	538
pbstween	6,62E+01	0,00512448	0,000231265	491
ecoli-6	6,62E+01	0,004117345	0,0001322	970
pbstween	6,62E+01	0,003629152	0,000179231	410
ecoli-5	6,62E+01	0,004845647	0,000189335	655
pbstween	6,62E+01	0,004769162	0,000236109	408
ecoli1	6,62E+01	0,003564489	0,000116884	930
pbstween	6,62E+01	0,00303865	9,26349E-05	1076

Table 5.6: Calculated statistical values of resonance angle during the cross-contamination experiment; *E.coli* flow on listeria antibody functionalized SPR chip.

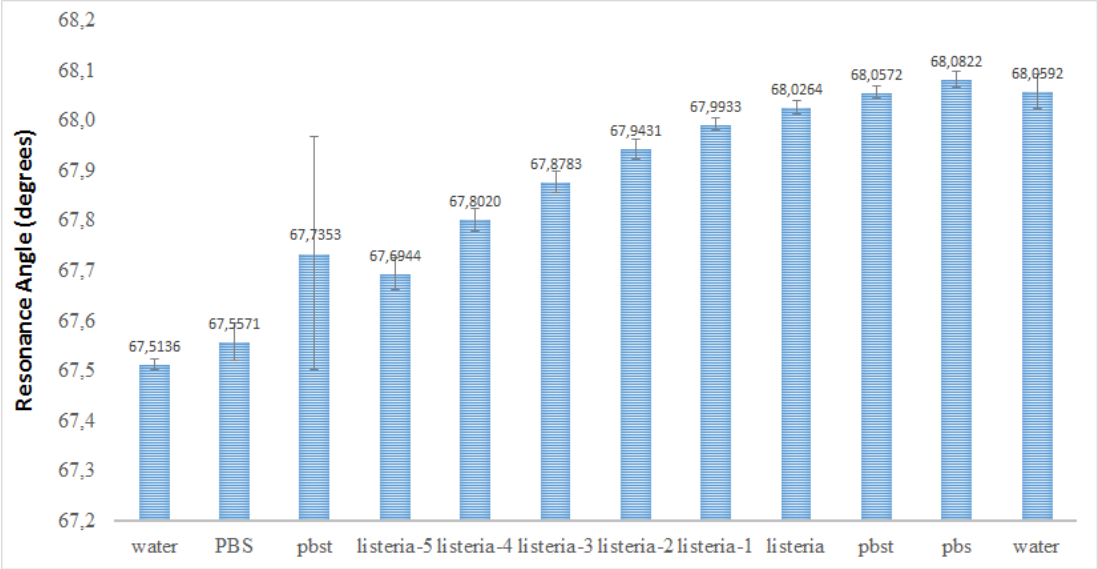

Figure 5.25: Average resonance angle vs serial dilution of *L.monocytogenes*. The SPR chip is functionalized with Listeria-antibody. Listeria-5 is equals to 250 pathogens, Listeria-4 is equal to 2500 pathogens, Listeria-3 is equal to 25000 pathogens, Listeria-2 is equals to 250000, Listeria-1 is equals to 2500000 and Listeria is equals to 25000000 pathogens.
content...

started to grow on the surface at room temperature. Therefore, we have done the same experiment with pathogens concentration just around the detection limit of the device. We have prepared a pathogen solution together with growth medium to observe in-situ growth. The idea is to enhance signal by using the multiplication of the pathogens so that we could detect pathogens below our detection limit. Bacterial growth after stopping the flow could be seen on the figure 5.28. In figure 5.29, We have focused on the growth region of figure 5.28.

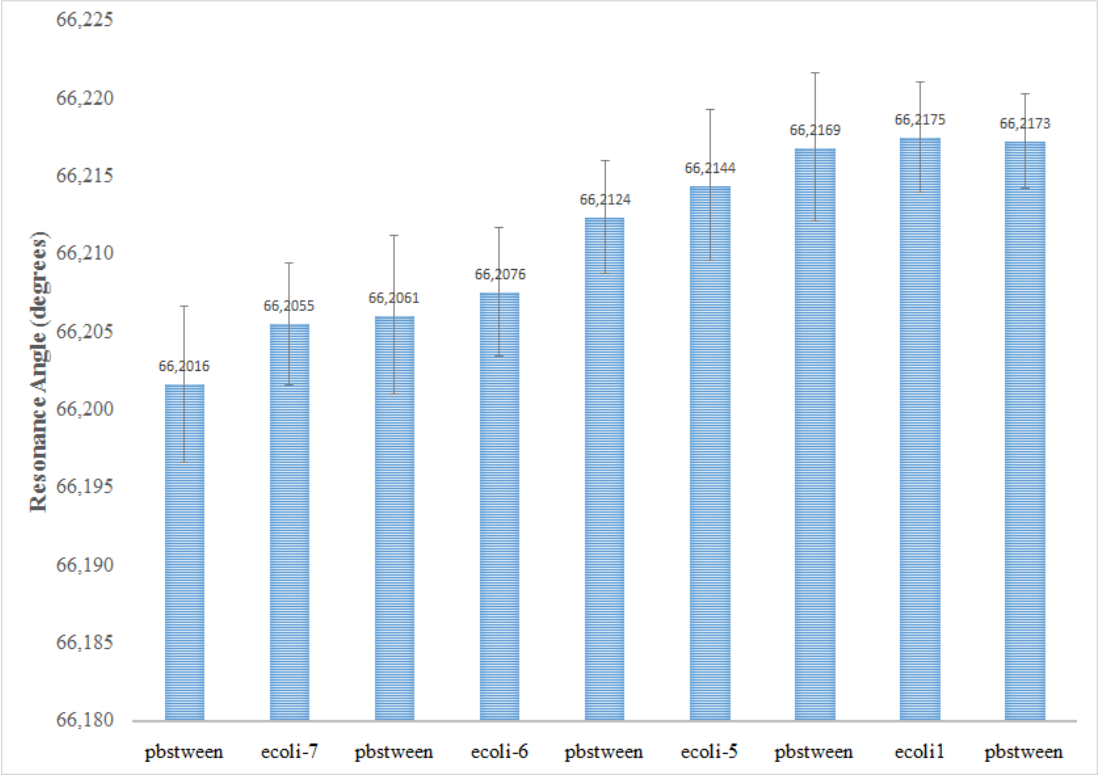

Figure 5.26: Average resonance angles vs serial dilution of *E.coli*. The SPR chip is functionalized with listeria antibody. Ecoli-7 is equals to 10 pathogens, Ecoli-6 is equal to 100 pathogens, E-coli5 is equal to 1000 pathogens, E-coli1 is equals to 10000000 pathogens.

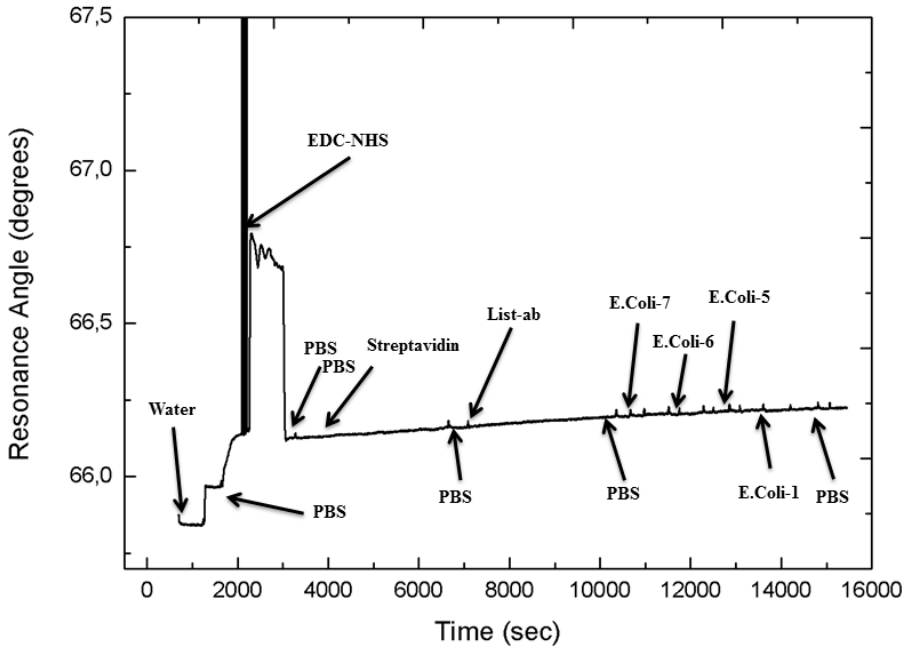

Figure 5.27: Resonance angle vs serial dilution of *E.coli* on anti-listeria antibody functionalized SPR chip.

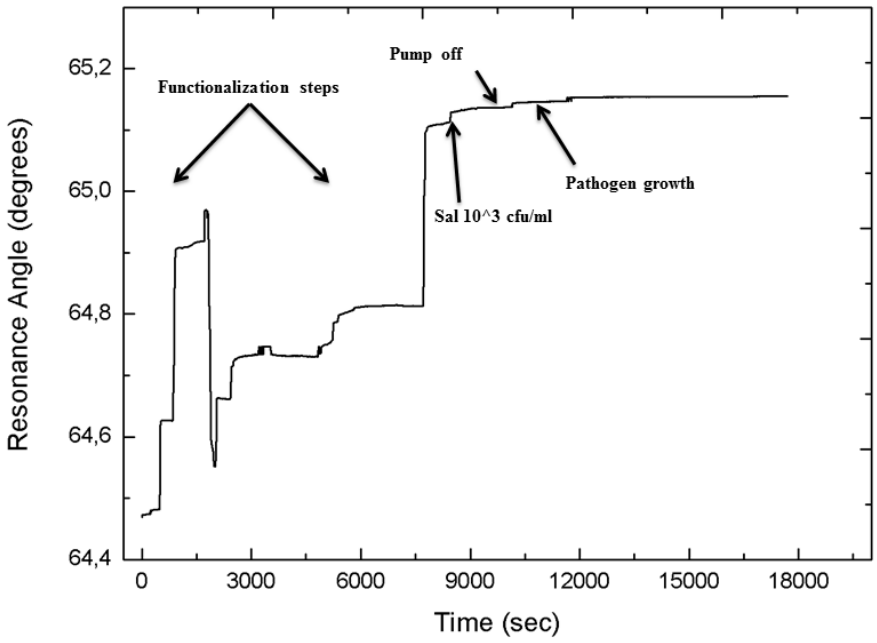

Figure 5.28: Resonance angle change during the *Salmonella* detection. After flow of *Salmonella* with 10^3 concentration, the pump is stopped to observe growth.

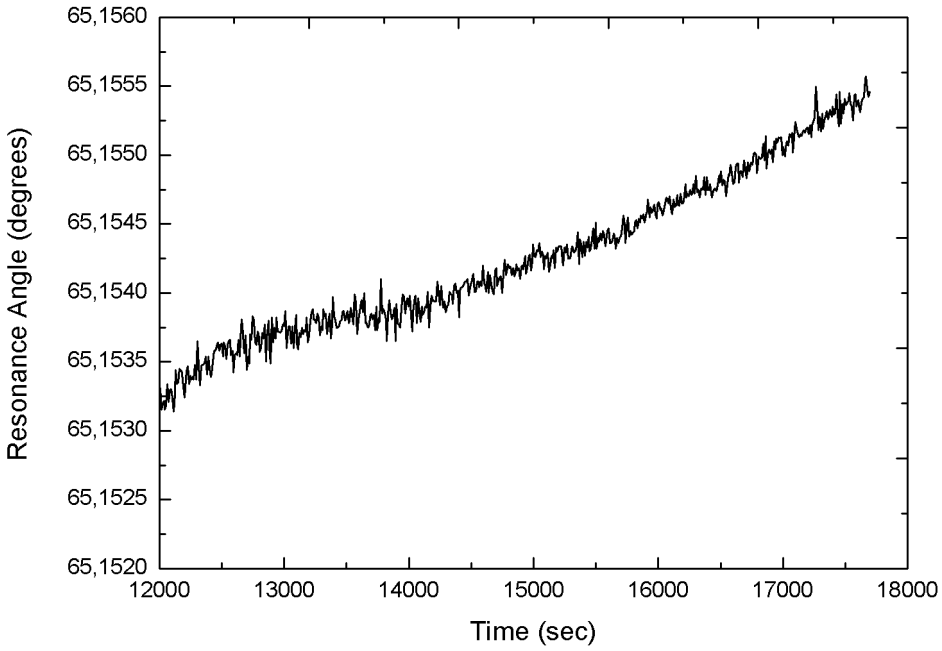

Figure 5.29: Resonance angle change during the *Salmonella* growth. The data is part of the graph in Figure 5.28.

Chapter 6

Conclusions

In summary, we demonstrated electrically induced reduction and oxidation of few-layer graphene films. If the repeatability and controllability of the observed effects can be improved, such electrochemical effects can be used in the design of novel micro- and nanoscale optoelectronic and memory devices. Demonstration of bias-controlled stoichiometry and nanoscale electronic structure can be viewed as electrically controlled formation of graphene quantum dots in grapheme oxide. A similar quantum dot structure has been theoretically studied recently in a similar system (i.e., hydrogenated graphene)[69]. The results presented in this work suggest that electrical bias and charging effects are important in energetic analysis and design of such nanostructures. Observations suggest that the practical graphene material family of optoelectronic devices is potentially subject to nanoscale chemical modifications during operation. Graphene transistor experiments that are working under ambient conditions and with high voltages should take into account possible electrochemical effects. In a transistor structure, it could be possible to protect graphene from oxidation by proper capping. However, electrochemical reduction/oxidation reactions may still be present in the solid phase if the binding energy of oxygen on graphene is more than that in the capping (or gate) oxide material. Oxidation effects could be minimized by use of a dielectric that does not contain oxygen, such as MgF_2. Charge-induced chemical reactions could also affect performance of graphene-based energy storage devices

such as super-capacitors. The findings show the importance of electrochemical effects for graphene-based devices

The linear and nonlinear optical properties are highly dependent on the electronic structure of the layers and the degree of reduction, thereby on bias and/or the intensity of the femtosecond pulses. The nonlinear optical characteristics of GO can be switched from SA to excited state absorption depending on the wavelength and the degree of reduction. Photo-thermal and electrochemical reduction are observed to produce changes with similar characteristics in the ultrafast response. Electrochemical tunability of the ultrafast response opens up the possibility of using GO-PRGO for tunable ultrafast optical device applications.

We have developed a technique that can to detect VOCs by using surface-enhanced Raman spectroscopy. We have fabricated and characterized SERS substrates. Surface diffusion of molecules on SERS substrate causes blinking in Raman signal. Further research showed that blinking involves Raman spectrum of VOCs. We have developed a technique to analyze and identify Raman spectra during blinking. Fragrance molecules were successfully identified in the time series of Raman spectra of SERS substrate. Experiments showed that our technique could be used for several applications such as detection of explosives, drugs and VOCs.

L. monocytogenes and *Salmonella spp.* are food borne pathogens which are responsible for the high proportion of the hospitalizations in the world. There is a current need for portable, real-time, multiplex pathogen detection technologies that can predict the safety of food. In this study, surface plasmon resonance (SPR) imaging was successfully used for sensitive, label-free detection and quantification of food pathogens in less than 5 hours. The demonstrated system can potentially be generalized to other pathogens for the selected food materials.

Bibliography

[1] K. S. Novoselov, A. K. Geim, S. V. Morozov, D. Jiang, M. I. Katsnelson, I. V. Grigorieva, S. V. Dubonos, and A. A. Firsov, "Two-dimensional gas of massless dirac fermions in graphene," *Nature*, vol. 5, no. 4, pp. 197–200, 2005.

[2] A. K. Geim and K. S. Novoselov, "The rise of graphene," *Nat. Mater.*, vol. 6, pp. 183–191, 2007.

[3] S. Stankovich, D. A. Dikin, G. H. B. Dommett, K. M. Kohlhaas, E. J. Zimney, E. A. Stach, R. D. Piner, S. T. Nguyen, and R. S. Ruoff, "Graphene-based composite materials," *Nature*, vol. 442, p. 282?286, 2006.

[4] I. Meric, M. Y. Han, A. F. Young, B. Ozyilmaz, P. Kim, and K. L. Shepard, "Current saturation in zero-bandgap, top gated graphene field-effect transistors," *Nat. Nanotechnol*, vol. 3, p. 654?659, 2008.

[5] Y.-M. Lin, C. Dimitrakopoulos, K. A. Jenkins, D. B. Farmer, H.-Y. Chiu, A. Grill, and P. Avouris, "100-ghz transistors from wafer-scale epitaxial graphene," *Science*, vol. 327, no. 5966, p. 662, 2010.

[6] K. S. Novoselov, Z. Jiang, Y. Zhang, S. V. Morozov, H. L. Stormer, U. Zeitler, J. C. Maan, G. S. Boebinger, P. Kim, and A. K. Geim, "Room-temperature quantum hall effect in graphene," *Science*, vol. 315, no. 5817, p. 1379, 2007.

[7] F. Schedin, A. K. Geim, S. V. Morozov, E. W. Hill, P. Blake, M. I. Katsnelson, and K. S. Novoselov, "Detection of individual gas molecules adsorbed on graphene," *Nat. Mater*, vol. 6, p. 652?655, 2007.

[8] . T. O. Wehling, K. S. Novoselov, . S. V. Morozov, . E. E. Vdovin, M. I. Katsnelson, A. K. Geim, , and A. I. Lichtenstein, "Molecular doping of graphene," *Nano Letters*, vol. 8, no. 1, pp. 173–177, 2008. PMID: 18085811.

[9] J. T. Robinson, F. K. Perkins, E. S. Snow, Z. Wei, and P. E. Sheehan, "Reduced graphene oxide molecular sensors," *Nano Letters*, vol. 8, no. 10, pp. 3137–3140, 2008. PMID: 18763832.

[10] M. D. Stoller, S. Park, Y. Zhu, J. An, and R. S. Ruoff, "Graphene-based ultracapacitors," *Nano Letters*, vol. 8, no. 10, pp. 3498–3502, 2008. PMID: 18788793.

[11] E. Yoo, J. Kim, E. Hosono, H. shen Zhou, T. Kudo, and I. Honma, "Large reversible li storage of graphene nanosheet families for use in rechargeable lithium ion batteries," *Nano Letters*, vol. 8, no. 8, pp. 2277–2282, 2008. PMID: 18651781.

[12] L. Wang, K. Lee, Y.-Y. Sun, M. Lucking, Z. Chen, J. J. Zhao, and S. B. Zhang, "Graphene oxide as an ideal substrate for hydrogen storage," *ACS Nano*, vol. 3, no. 10, pp. 2995–3000, 2009. PMID: 19856979.

[13] T. Mueller, F. Xia, and P. Avouris, "Graphene photodetectors for high-speed optical communications," *Nat. Photonics*, vol. 4, p. 297?301, 2010.

[14] T. Gokus, R. R. Nair, A. Bonetti, M. Bhmler, A. Lombardo, K. S. Novoselov, A. K. Geim, A. C. Ferrari, and A. Hartschuh, "Making graphene luminescent by oxygen plasma treatment," *ACS Nano*, vol. 3, no. 12, pp. 3963–3968, 2009. PMID: 19925014.

[15] Z. Sun, T. Hasan, F. Torrisi, D. Popa, G. Privitera, F. Wang, F. Bonaccorso, D. M. Basko, and A. C. Ferrari, "Graphene mode-locked ultrafast laser," *ACS Nano*, vol. 4, no. 2, pp. 803–810, 2010. PMID: 20099874.

[16] K. Bolotin, K. Sikes, Z. Jiang, M. Klima, G. Fudenberg, J. Hone, P. Kim, and H. Stormer, "Ultrahigh electron mobility in suspended graphene," *Solid State Communications*, vol. 146, no. 9?10, pp. 351 – 355, 2008.

[17] H. Sevinçli, M. Topsakal, and S. Ciraci, "Superlattice structures of graphene-based armchair nanoribbons," *Phys. Rev. B*, vol. 78, p. 245402, Dec 2008.

[18] A. K. Singh and B. I. Yakobson, "Electronics and magnetism of patterned graphene nanoroads," *Nano Letters*, vol. 9, no. 4, pp. 1540–1543, 2009.

[19] M. Y. Han, B. Özyilmaz, Y. Zhang, and P. Kim, "Energy band-gap engineering of graphene nanoribbons," *Phys. Rev. Lett.*, vol. 98, p. 206805, May 2007.

[20] J. Bai, X. Zhong, S. Jiang, Y. Huang, and X. Duan, "Graphene nanomesh," *Nat. Nanotechnology*, vol. 5, p. 190?194, 2010.

[21] Y. Li, A. Sinitskii, and J. M. Tour, "Electronic two-terminal bistable graphitic memories," *Nat. Mater*, vol. 7, p. 966? 971, 2008.

[22] C. L. He, F. Zhuge, X. F. Zhou, M. Li, G. C. Zhou, Y. W. Liu, J. Z. Wang, B. Chen, W. J. Su, Z. P. Liu, Y. H. Wu, P. Cui, and R.-W. Li, "Nonvolatile resistive switching in graphene oxide thin films," *Applied Physics Letters*, vol. 95, no. 23, 2009.

[23] T. Echtermeyer, M. C. Lemme, M. Baus, B. Szafranek, A. Geim, and H. Kurz, "Nonvolatile switching in graphene field-effect devices," *Electron Device Letters, IEEE*, vol. 29, pp. 952–954, Aug 2008.

[24] J.-A. Yan, L. Xian, and M. Y. Chou, "Structural and electronic properties of oxidized graphene," *Phys. Rev. Lett.*, vol. 103, p. 086802, Aug 2009.

[25] D. W. Boukhvalov and M. I. Katsnelson, "Modeling of graphite oxide," *Journal of the American Chemical Society*, vol. 130, no. 32, pp. 10697–10701, 2008. PMID: 18627149.

[26] I. Jung, D. A. Dikin, R. D. Piner, and R. S. Ruoff, "Tunable electrical conductivity of individual graphene oxide sheets reduced at ?low? temperatures," *Nano Letters*, vol. 8, no. 12, pp. 4283–4287, 2008. PMID: 18975992.

[27] V. Lpez, R. S. Sundaram, C. Gmez-Navarro, D. Olea, M. Burghard, J. Gmez-Herrero, F. Zamora, and K. Kern, "Chemical vapor deposition repair of

graphene oxide: A route to highly-conductive graphene monolayers," *Advanced Materials*, vol. 21, no. 46, pp. 4683–4686, 2009.

[28] L. J. Cote, R. Cruz-Silva, and J. Huang, "Flash reduction and patterning of graphite oxide and its polymer composite," *Journal of the American Chemical Society*, vol. 131, no. 31, pp. 11027–11032, 2009. PMID: 19601624.

[29] . Cristina Gmez-Navarro, . R. Thomas Weitz, . Alexander M. Bittner, . Matteo Scolari, . Alf Mews, . Marko Burghard, *, , and . Klaus Kern?, "Electronic transport properties of individual chemically reduced graphene oxide sheets," *Nano Letters*, vol. 7, no. 11, pp. 3499–3503, 2007. PMID: 17944526.

[30] Z. Wei, D. Wang, S. Kim, S.-Y. Kim, Y. Hu, M. K. Yakes, A. R. Laracuente, Z. Dai, S. R. Marder, C. Berger, W. P. King, W. A. de Heer, P. E. Sheehan, and E. Riedo, "Nanoscale tunable reduction of graphene oxide for graphene electronics," *Science*, vol. 328, no. 5984, pp. 1373–1376, 2010.

[31] P. Sessi, J. R. Guest, M. Bode, and N. P. Guisinger, "Patterning graphene at the nanometer scale via hydrogen desorption," *Nano Letters*, vol. 9, no. 12, pp. 4343–4347, 2009. PMID: 19883050.

[32] J. M. Mativetsky, E. Treossi, E. Orgiu, M. Melucci, G. P. Veronese, P. Samor, and V. Palermo, "Local current mapping and patterning of reduced graphene oxide," *Journal of the American Chemical Society*, vol. 132, no. 40, pp. 14130–14136, 2010. PMID: 20925312.

[33] W. S. H. Jr. and R. E. Offeman, "Preparation of graphitic oxide," *Journal of the American Chemical Society*, vol. 80, no. 6, pp. 1339–1339, 1958.

[34] S. Stankovich, R. D. Piner, C. Chen, N. Wu, S. T. Nguyen, and R. S. Ruoff, "Stable aqueous dispersions of graphitic nanoplatelets via the reduction of exfoliated graphite oxide in the presence of poly(sodium 4-styrenesulfonate)," *J. Mater. Chem.*, vol. 16, p. 155 ?158, 2006.

[35] X. D. Ding, J. An, J. B. Xu, C. Li, and R. Y. Zeng, "Improving lateral resolution of electrostatic force microscopy by multifrequency method under ambient conditions," *Applied Physics Letters*, vol. 94, no. 22, 2009.

[36] D. Ziegler, J. Rychen, N. Naujoks, and A. Stemmer, "Compensating electrostatic forces by single-scan kelvin probe force microscopy," *Nanotechnology*, vol. 18, no. 22, p. 225505, 2007.

[37] U. Bostanci, M. K. Abak, O. Aktaş, and A. Dna, "Nanoscale charging hysteresis measurement by multifrequency electrostatic force spectroscopy," *Applied Physics Letters*, vol. 92, no. 9, 2008.

[38] R. R. Nair, P. Blake, A. N. Grigorenko, K. S. Novoselov, T. J. Booth, T. Stauber, N. M. R. Peres, and A. K. Geim, "Fine structure constant defines visual transparency of graphene," *Science*, vol. 320, no. 5881, p. 1308, 2008.

[39] P. Avouris, R. Martel, T. Hertel, and R. Sandstrom, "Afm-tip-induced and current-induced local oxidation of silicon and metals," *Applied Physics A*, vol. 66, no. 1, pp. S659–S667, 1998.

[40] Y. Okada, S. Amano, M. Kawabe, and J. S. Harris, "Basic mechanisms of an atomic force microscope tip-induced nano-oxidation process of gaas," *Journal of Applied Physics*, vol. 83, no. 12, 1998.

[41] P. Avouris, T. Hertel, and R. Martel, "Atomic force microscope tip-induced local oxidation of silicon: kinetics, mechanism, and nanofabrication," *Applied Physics Letters*, vol. 71, no. 2, 1997.

[42] J. M. Dawlaty, S. Shivaraman, M. Chandrashekhar, F. Rana, and M. G. Spencer, "Measurement of ultrafast carrier dynamics in epitaxial graphene," *Applied Physics Letters*, vol. 92, no. 4, 2008.

[43] G. Xing, H. Guo, X. Zhang, T. C. Sum, and C. H. A. Huan, "The physics of ultrafast saturable absorption in graphene," *Opt. Express*, vol. 18, pp. 4564–4573, Mar 2010.

[44] J.-A. Yan, L. Xian, and M. Y. Chou, "Structural and electronic properties of oxidized graphene," *Phys. Rev. Lett.*, vol. 103, p. 086802, Aug 2009.

[45] Z. Liu, Y. Wang, X. Zhang, Y. Xu, Y. Chen, and J. Tian, "Nonlinear optical properties of graphene oxide in nanosecond and picosecond regimes," *Applied Physics Letters*, vol. 94, no. 2, 2009.

[46] Y. Zhang, L. Guo, S. Wei, Y. He, H. Xia, Q. Chen, H.-B. Sun, and F.-S. Xiao, "Direct imprinting of microcircuits on graphene oxides film by femtosecond laser reduction," *Nano Today*, vol. 5, no. 1, pp. 15 – 20, 2010.

[47] O. ner Ekiz, M. rel, H. Gner, A. K. Mizrak, and A. Dna, "Reversible electrical reduction and oxidation of graphene oxide," *ACS Nano*, vol. 5, no. 4, pp. 2475–2482, 2011. PMID: 21391707.

[48] D. Sun, Z.-K. Wu, C. Divin, X. Li, C. Berger, W. A. de Heer, P. N. First, and T. B. Norris, "Ultrafast relaxation of excited dirac fermions in epitaxial graphene using optical differential transmission spectroscopy," *Phys. Rev. Lett.*, vol. 101, p. 157402, Oct 2008.

[49] Y. Zhu, S. Murali, W. Cai, X. Li, W. Ji, J. R. Potts, and R. S. Ruoff, "Graphene and graphene oxide: synthesis, properties, and applications)," *Adv. Mater.*, vol. 22, p. 3906?3924, 2010.

[50] E. J. Blackie, E. C. L. Ru, and P. G. Etchegoin, "Single-molecule surface-enhanced raman spectroscopy of nonresonant molecules," *Journal of the American Chemical Society*, vol. 131, no. 40, pp. 14466–14472, 2009. PMID: 19807188.

[51] . E. C. Le Ru, E. Blackie, M. Meyer, , and P. G. Etchegoin, "Surface enhanced raman scattering enhancement factors: A comprehensive study," *The Journal of Physical Chemistry C*, vol. 111, no. 37, pp. 13794–13803, 2007.

[52] S. Nie and S. R. Emory, "Probing single molecules and single nanoparticles by surface-enhanced raman scattering," *Science*, vol. 275, no. 5303, pp. 1102–1106, 1997.

[53] . E. C. Le Ru, M. Meyer, , and P. G. Etchegoin*, "Proof of single-molecule sensitivity in surface enhanced raman scattering (sers) by means of a two-analyte technique," *The Journal of Physical Chemistry B*, vol. 110, no. 4, pp. 1944–1948, 2006. PMID: 16471765.

[54] S. B. Walker and J. A. Lewis, "Reactive silver inks for patterning high-conductivity features at mild temperatures," *Journal of the American Chemical Society*, vol. 134, no. 3, pp. 1419–1421, 2012. PMID: 22220580.

[55] K. Kneipp, Y. Wang, H. Kneipp, L. T. Perelman, I. Itzkan, R. R. Dasari, and M. S. Feld, "Single molecule detection using surface-enhanced raman scattering (sers)," *Phys. Rev. Lett.*, vol. 78, pp. 1667–1670, Mar 1997.

[56] E. C. L. Ru and P. Etchegoin, "Single-molecule surface-enhanced raman spectroscopy," *Rev. Phys. Chem.*, vol. 63, p. 65?87, 2012.

[57] S. K. Saikin, Y. Chu, D. Rappoport, K. B. Crozier, and A. Aspuru-Guzik, "Separation of electromagnetic and chemical contributions to surface-enhanced raman spectra on nanoengineered plasmonic substrates," *The Journal of Physical Chemistry Letters*, vol. 1, no. 18, pp. 2740–2746, 2010.

[58] F. C. Dudak and I. H. Boyaci, "Development of an immunosensor based on surface plasmon resonance for enumeration of escherichia coli in water samples," *Food Research International*, vol. 40, no. 7, pp. 803 – 807, 2007.

[59] G. Kisluk, D. G. Hoover, K. E. Kneil, and S. Yaron, "Quantification of low and high levels of salmonella enterica serovar typhimurium on leaves," {*LWT*} - *Food Science and Technology*, vol. 45, no. 1, pp. 36 – 42, 2012.

[60] C. Situ, M. H. Mooney, C. T. Elliott, and J. Buijs, "Advances in surface plasmon resonance biosensor technology towards high-throughput, food-safety analysis," *TrAC Trends in Analytical Chemistry*, vol. 29, no. 11, pp. 1305 – 1315, 2010.

[61] P. Fratamico, T. Strobaugh, M. Medina, and A. Gehring, "Detection of escherichia coli 0157:h7 using a surface plasmon resonance biosensor," *Biotechnology Techniques*, vol. 12, no. 7, pp. 571–576, 1998.

[62] V. Koubov, E. Brynda, L. Karasov, J. ?kvor, J. Homola, J. Dostlek, P. Tobi?ka, and J. Ro?ick, "Detection of foodborne pathogens using surface plasmon resonance biosensors," *Sensors and Actuators B: Chemical*, vol. 74, no. 1?3, pp. 100 – 105, 2001. Proceedings of the 5th European Conference on Optical Chemical Sensors and Biosensors.

[63] J. Waswa, J. Irudayaraj, and C. DebRoy, "Direct detection of e. coli o157:h7 in selected food systems by a surface plasmon resonance biosensor," {*LWT*} - *Food Science and Technology*, vol. 40, no. 2, pp. 187 – 192, 2007.

[64] Y. bin Lan, S. zhou Wang, Y. guang Yin, W. C. Hoffmann, and X. zhe Zheng, "Using a surface plasmon resonance biosensor for rapid detection of salmonella typhimurium in chicken carcass," *Journal of Bionic Engineering*, vol. 5, no. 3, pp. 239 – 246, 2008.

[65] J. Homola, "Surface plasmon resonance sensors for detection of chemical and biological species," *Chem. Rev.*, vol. 108, pp. 462–493, 2008.

[66] J. Homola, S. S. Yee, and G. Gauglitz, "Surface plasmon resonance sensors: review," *Sensors and Actuators B: Chemical*, vol. 54, pp. 3 – 15, 1999.

[67] O. Tokel, U. H. Yıldız, F. İnci, N. G. Durmuş, O. Ekiz, B. Turker, C. Cetin, S. Rao, K. Sridhar, N. Natarajan, H. Shafiee, A. Dana, and U. Demirci, "Portable microfluidic integrated plasmonic platform for pathogen detection," *Scientific Reports*, vol. 5, pp. 1–9, 2015.

[68] B. Malorny, P. T. Tassios, P. Rdstrm, N. Cook, M. Wagner, and J. Hoorfar, "Standardization of diagnostic {PCR} for the detection of foodborne pathogens," *International Journal of Food Microbiology*, vol. 83, no. 1, pp. 39 – 48, 2003.

[69] A. K. Singh, E. S. Penev, and B. I. Yakobson, "Vacancy clusters in graphane as quantum dots," *ACS Nano*, vol. 4, no. 6, pp. 3510–3514, 2010.